ABSTRACT

DESIGN AND CONTROL OF NEXT-GENERATION UAVS FOR EFFECTIVELY INTERACTING WITH ENVIRONMENTS

by
Caiwu Ding

In this dissertation, the design and control of a novel multirotor for aerial manipulation is studied, with the aim of endowing the aerial vehicle with more degrees of freedom of motion and stability when interacting with the environments. Firstly, it presents an energy-efficient adaptive robust tracking control method for a class of fully actuated, thrust vectoring unmanned aerial vehicles (UAVs) with parametric uncertainties including unknown moment of inertia, mass and center of mass, which would occur in aerial maneuvering and manipulation. The effectiveness of this method is demonstrated through simulation. Secondly, a humanoid robot arm is adopted to serve as a 6-degree-of-freedom (DOF) automated flight testing platform for emulating the free flight environment of UAVs while ensuring safety. Another novel multirotor in a tilt-rotor architecture is studied and tested for coping with parametric uncertainties in aerial maneuvering and manipulation. Two pairs of rotors are mounted on two independently-controlled tilting arms placed at two sides of the vehicle in a "H" configuration to enhance its maneuverability and stability through an adaptive robust control method. In addition, an impedance control algorithm is deployed in the out loop that modifies the trajectory to achieve a compliant behavior in the end-effector space for aerial drilling and screwing tasks.

DESIGN AND CONTROL OF NEXT-GENERATION UAVS FOR EFFECTIVELY INTERACTING WITH ENVIRONMENTS

by
Caiwu Ding

A Dissertation
Submitted to the Faculty of
New Jersey Institute of Technology
in Partial Fulfillment of the Requirements for the Degree of
Doctor of Philosophy in Mechanical Engineering

Department of Mechanical and Industrial Engineering

May 2022

APPROVAL PAGE

DESIGN AND CONTROL OF NEXT-GENERATION UAVS FOR EFFECTIVELY INTERACTING WITH ENVIRONMENTS

Caiwu Ding

Dr. Lu Lu, Dissertation Advisor — Date
Assistant Professor of Mechanical and Industrial Engineering, NJIT

Dr. Ian S. Fischer, Committee Member — Date
Professor of Mechanical and Industrial Engineering, NJIT

Dr. Zhiming Ji, Committee Member — Date
Professor of Mechanical and Industrial Engineering, NJIT

Dr. Cong Wang, Committee Member — Date
Associate Professor of Electrical and Computer Engineering, NJIT

Dr. Samuel C. Lieber, Committee Member — Date
Assistant Professor of Applied Engineering Technology, NJIT

BIOGRAPHICAL SKETCH

Author: Caiwu Ding

Degree: Doctor of Philosophy

Date: May 2022

Undergraduate and Graduate Education:

- Doctor of Philosophy in Mechanical Engineering,
  New Jersey Institute of Technology, Newark, NJ, 2022
- Master of Science in Engineering and Technology Management,
  Morehead State University, Morehead, KY, 2016
- Bachelor of Science in Mechanical Design and Manufacturing Its Automation,
  Yangtze Normal University, Chongqing, China, 2014

Major: Mechanical Engineering

Presentations and Publications:

C. Ding, L. Lu, C. Wang and C. Ding, "Design, Sensing, and Control of a Novel UAV Platform for Aerial Drilling and Screwing," *IEEE Robotics and Automation Letters*, vol. 6, no. 2, pages 3176-3183, 2021

C. Ding and L. Lu, "A Tilting-Rotor Unmanned Aerial Vehicle for Enhanced Aerial Locomotion and Manipulation Capabilities: Design, Control, and Applications," *IEEE/ASME Transactions on Mechatronics*, vol. 26, no. 4, pages 2237-2248, 2021

S. Zhou, B. Li, C. Ding, L. Lu and C. Ding, "An Efficient Deep Reinforcement Learning Framework for UAVs," *21st International Symposium on Quality Electronic Design (ISQED)*, pages 323-328, 2020

C Ding, L Lu, C Wang, "Energy-Efficient Adaptive Robust Control of Vector Thrust UAVs With Unknown Inertia Parameters," *American Society of Mechanical Engineers (ASME) Dynamic Systems and Control Conference (DSCC)*, 2018

C. Ding, L. Lu, C. Wang and J. Li, "6-DOF Automated Flight Testing Using a Humanoid Robot Arm," *IEEE 14th International Conference on Automation Science and Engineering (CASE)*, 2018

C Ding, C Wang, L Lu, B Ouyang, "Modeling and control of fully actuated vector thrust unmanned aerial vehicles," *International Symposium on Flexible Automation*, 2018

"Man first of all exists, encounters himself, surges up in the world—and defines himself afterwards."

–Jean-Paul Sartre

ACKNOWLEDGMENT

I would like to give thanks to my advisor, Dr. Lu Lu, for his illuminating guidance and continuous support through each stage of the research.

I also want to express my gratitude to all my committee members: Dr. Ian S. Fischer, Dr. Zhiming Ji, Dr. Samuel C. Lieber, and Dr. Cong Wang for the support of my research.

I appreciate the support from my beloved department and school, Department of Mechanical and Industrial Engineering at New Jersey Institute of Technology. Thanks my department for providing teaching assistantship to me.

I am also extremely grateful to all the members of our Assistive and Intelligent Robotics lab and Dr. Cong Wang's lab who have provided me assistance and inspiration during the research.

TABLE OF CONTENTS

Chapter **Page**

TABLE OF CONTENTS
(Continued)

Chapter **Page**

TABLE OF CONTENTS
(Continued)

Chapter **Page**

LIST OF FIGURES

LIST OF FIGURES
(Continued)

Figure **Page**

LIST OF FIGURES
(Continued)

Figure **Page**

CHAPTER 1

INTRODUCTION

1.1 Background and Motivation

The last decade has seen dramatic growth of the Unmanned Aerial Vehicles(UAVs) research, both for civilian and military applications such as remote surveillance, photography, inspection, search and rescue operations. It shows that multirotors have arisen as an mature platform with great adoption for implementing tasks where aerial mobility and aerial perspective are needed. Additionally, aerial interaction and manipulation using multirotor vehicles as shown in Figure 1.1 are recently receiving increasing attention due to its goal of enabling multirotors to actively interact with external environments, instead of just being the under-actuated passive sensing platforms. The design and control of standard multirotor UAVs including tricopters, quadcopters and hexrotors are well studied, however, they have limited mobility and controllability due to their inherent underactuation nature. Thus, the standard multirotors are not capable of tracking arbitrary position and orientation trajectories in 3D space [1]. Such capability, however, is required for UAVs to execute complex interactive tasks such as aerial manipulation [2, 3, 4].

Theoretically, a fully actuated UAV should be configured to track any desired trajectory of body position and orientation, and is therefore an ideal choice for applications involving aerial locomotion, and dexterous manipulation in a constrained environment. In recent years, many different fully actuated UAVs have been designed, which include the ones with at least six rotors with propellers facing different directions [5, 6, 4], as demonstrated in Figure 1.2, and the ones with tilting rotors/propellers [7, 1, 8, 9], as shown in Figure 1.3. The latter type is structurally more complicated, but more efficient in terms of energy consumption since it is possible to minimize the inefficient mutual force cancellation between propellers by properly tilting each

Figure 1.1 Application scenarios in which aerial manipulation may be helpful. From left to right: bridge, power line, wind turbine inspection and repair.

propeller. In particular, in [8, 10], the authors proposed fully actuated multirotors, of which each propeller can tilt about two axes. The control system design is in combination with preflight setup of tilting angle α and β depending on the needs of a particular trajectory, to attain non-linear trajectory tracking. However, the optimization scheme for redundancy resolution imposes some artificial constraints on the tilting angles α and β for each propeller, which does not guarantee global optimality of the solution and compromises performance.

Figure 1.2 Multirotors with at least six rotors with propellers facing different directions.

Figure 1.3 Multirotors with tilting rotors/propellers.

As mentioned before, one of the applications of the fully actuated UAVs is the aerial manipulation and maneuvering in constrained environments. The vehicle may pick up an unknown payload, change its body orientation, fly around obstacles, and drop the payload. During this process, the inertial parameters including the moment of inertia, the mass and center of mass are subject to abrupt changes. The unknown inertial parameters will significantly affect the flight performance especially when the fully actuated UAV flies at a non-horizontal posture. Thus, the online adaptation of these parameters is necessary to maintain a stable and desired flight. Adaptive control has been used in the previous studies to address this issue in aerial manipulation [11, 12], as shown in Figure 1.4. However, the object being grasped was assumed to be a point mass at the end-effector, resulting in only two parameters to be estimated. When grasping a large object with unknown inertia and center of mass, this simplified approach will fail to establish. Furthermore, how the uncertain nonlinearities not captured by the parametric model of the system affect the closed-loop control performance was not studied.

1.2 Aims and Objectives

Firstly, this dissertation studies an energy-efficient adaptive robust control framework for a class of fully actuated vector thrust multirotor UAVs, to generate the $6-DOF$ force/torque wrench such that an accurate position/orientation trajectory tracking is

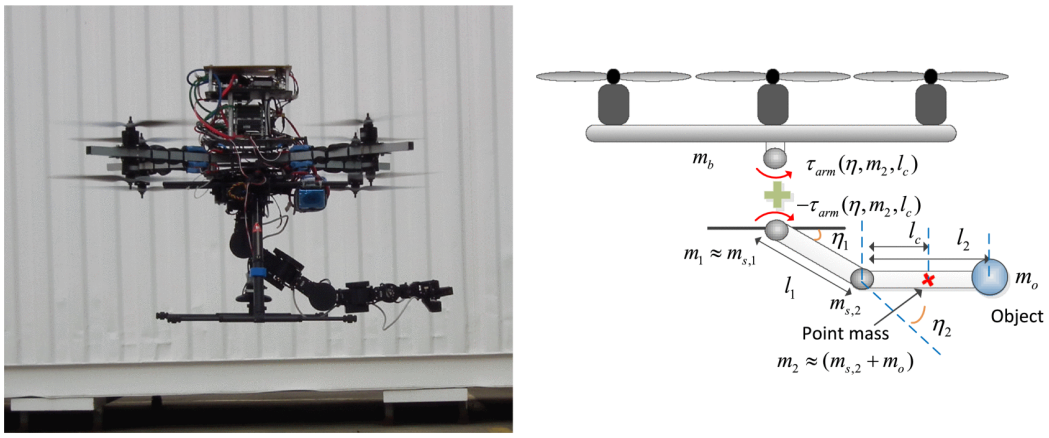

Figure 1.4 Aerial Manipulation and Parametric Uncertainties.

achieved in the presence of parametric uncertainties as well as uncertain nonlinearities of the system. To resolve actuation redundancy of the fully actuated UAVs, a thrust force optimization problem minimizing power consumption while achieving the desired body force/torque wrench is formulated.

Secondly, after a new vehicle and its control law are designed, an initial flight testing is necessary to validate the functionality and performance of the vehicle under an emulated free flight environment. In the next chapter, this dissertation studies a new method of flight testing of VTOL UAVs by using an articulated humanoid robot arm with a 6-axis force/torque sensor as the test platform. Specifically, the vehicle is mounted to the end-effector of the robot arm through the force/torque sensor. The robot arm carries the vehicle and follows its movement quickly and precisely during the flight testing. To test the performance of the designed vehicle controller in an emulated free flight environment while ensuring safety, we develop a dual-module control approach to control the robot arm so that the $6-DOF$ free flight emulation and safety can be ensured simultaneously, which has not been achieved before.

In the next chapter, this dissertation investigates the design and control of a novel multirotor UAV that is capable of achieving the follow advantages, which are required for the next-generation UAVs for effectively interacting with environments.

1. More motion DOFs than traditional UAVs, which is characterized by the ability of the vehicle to change one or two of its attitude angles independently from the translational motions.
2. Simple mechanical structure, which is to avoid stability, robustness, and high weight issues arising from over-complicated designs.
3. Avoidance of thrust force cancellation (through both the design and control) to achieve high power efficiency.
4. High motion control precision and the ability to adapt to changing parameters during locomotion and manipulation in unknown environments.

With such a design, the vehicle has one more DOF of motion than the traditional quadcopters, allowing it to have independent roll angle regulation at the expense of only two additional servo motors with minimum transmission needed.

Finally, a human-guided semi-automated aerial drilling/screwing platform based on our developed novel tilting-rotor aerial manipulator is presented. The developed drilling/screwing platform can achieve omnidirectional drilling/screwing. Based on the dynamics of the proposed UAV design, a dual-level control law is designed. The low-level attitude controller uses an adaptive robust control (ARC) to accurately regulate the attitude angles in the presence of force/torque uncertainties that may occur during the drilling and screwing process, while a selective impedance controller is implemented at high level to indirectly control the contact force commanded by the user. In addition, a vision-based guidance scheme is developed to identify and track the target feature on the workpiece. For verification, we conduct various indoor hole drilling and bolt screwing experiments on a vertical wood plate to show the applicability of our approach.

CHAPTER 2

FULLY-ACTUATED VECTOR THRUST MULTIROTORS

2.1 Introduction

A hierarchical(multi-loops) architecture is currently the most widely used controller strategy tackling with the stabilization problem of underactuated multirotors. It resorts to [13, 14] an inner loop of high frequency and an outer loop of comparatively low frequency for angular and linear dynamics respectively, as shown in Figure 2.1. In this case, the position and the yaw angle of the multirotor UAV can be set as final outputs [15, 16]. Therefore, it is possible to track any position and yaw angle trajectory in the Cartesian space with a desired heading angle stemming from its desired trajectory. Thus, the underactuation issue is solved, as tracking of the desired position and yaw angle (low frequency outer loop) generates the references of heading angles for the high frequency inner loop controller. There exist other worthy approaches including impedance [17], backstepping [18] and optical flow [19] techniques, as demonstrated by Figure 2.2.

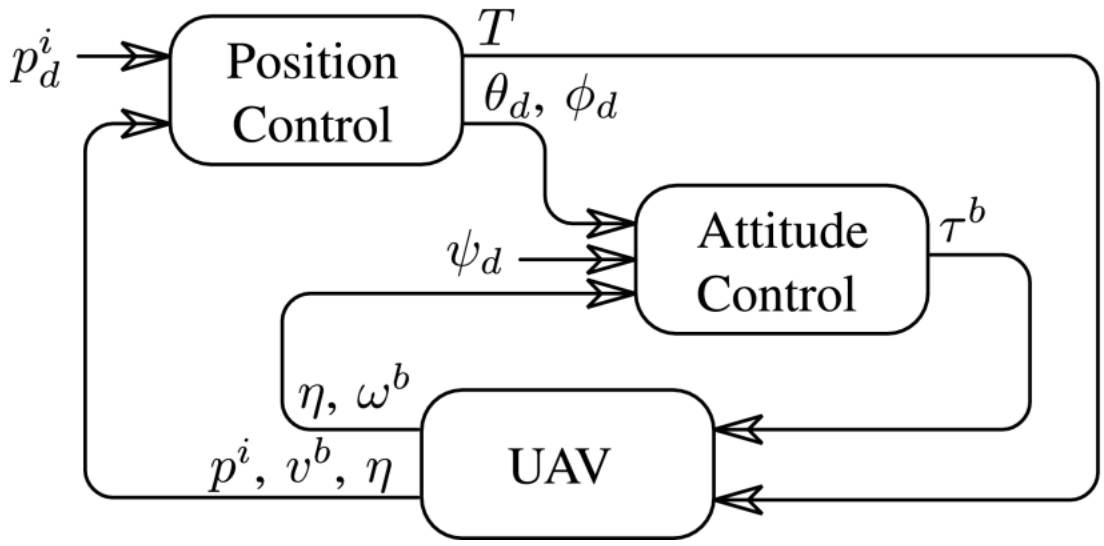

Figure 2.1 Inner–outer loop controller structure.

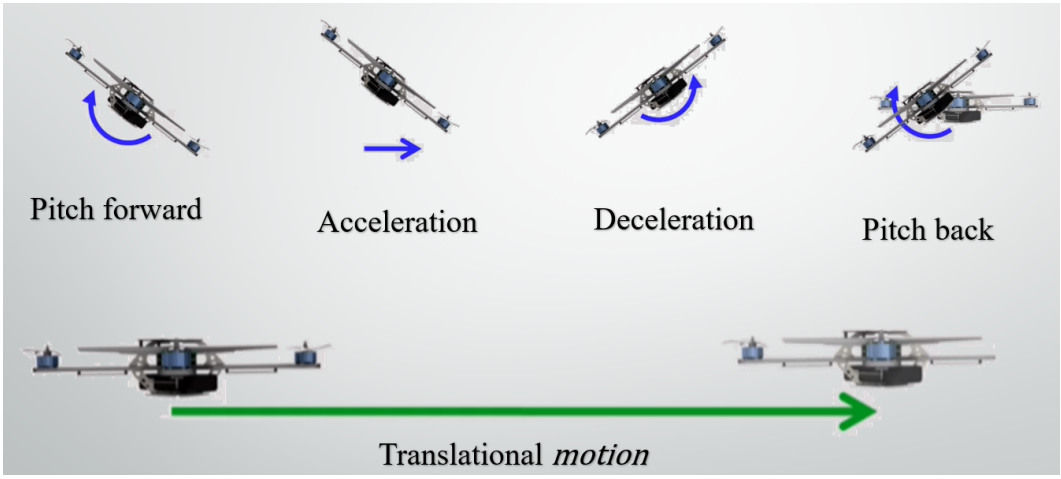

Figure 2.2 Multirotors controller strategy.

Another issue is derived from the factor that the aerodynamic model of the multirotor vehicle is very complicated, and in order to derive its dynamic model several assumptions need to be made. Thus, different robust control laws are proposed for control of UAVs. And an integral controller is wildly adopted in most of them to resist against external disturbances and tackle with unknown and time-varying parameters [20, 21, 22, 23, 24, 25].

Current aerial manipulation vehicles are all based on traditional multirotor platforms, and the proper tools are equipped to accomplish manipulation tasks in the air. According to the tools attached on the vehicles, there are two most adopted solutions: to mount a gripper or a multi-fingered hand directly on the aerial vehicle, e.g., called a flying hand (FH) or to equip the UAV with one or more robotic arms, e.g., which is named as unmanned aerial manipulator (UAM) as shown in Figure 2.3. In the first case, the FH can only grasp and locally manipulate an object, and usually the control of this manipulation can't be independent from the motion of the aerial platform. Moreover, the single gripper does not have enough DOF to complete complex tasks which require dexterous manipulation. Thus, to equip the aerial vehicles with more mechanical structures are essential to perform more complex actions. Examples to be referred of this scenario can be taken from research about mobile ground

platforms [26], underwater [27], and space robots [28]. It turns out that a UAM could be an efficient solution endowing an aerial manipulation vehicle with the capability of performing dexterous tasks.

Figure 2.3 A flying hand (left) and an unmanned arial manipulator (right).

2.2 System Structure and Coordinate Systems

The UAV considered in this section contains n arms ($n \geq 3$) stretching outward from the main body, as shown in the top view of Figure 2.4. The arms are equally distributed around the body. An arc-shaped fork is attached to the outer end of each arm, and a propelling rotor is mounted to the fork. Two servos are equipped to change the directions of the thrust force generated by each rotor, as shown in the side views of Figure 2.4. One servo rotates about the axis1, changing the relative angle between the arm and the fork, denoted as α_i, $i = 1, \cdots, n$. The other servo rotates about the axis2, changing the relative angle between the fork and rotor, denoted as β_i, $i = 1, \cdots, n$. We assume that all the arms, forks, rotors and propellers have the same geometric and inertial parameters. The length from the actuation point to the center of the UAV body is l, and the propeller radius is r. The entire system has $3n$ degrees of actuation, higher than the degrees of freedom of the UAV body which is six. Thus, by properly varying the thrust force vector of each rotor, arbitrary position/orientation trajectory of the vehicle body can be achieved, while the rest of the degrees of freedom

can be used for optimizing power consumption. A prototype of the such UAV with four rotors is shown in Figure 2.5.

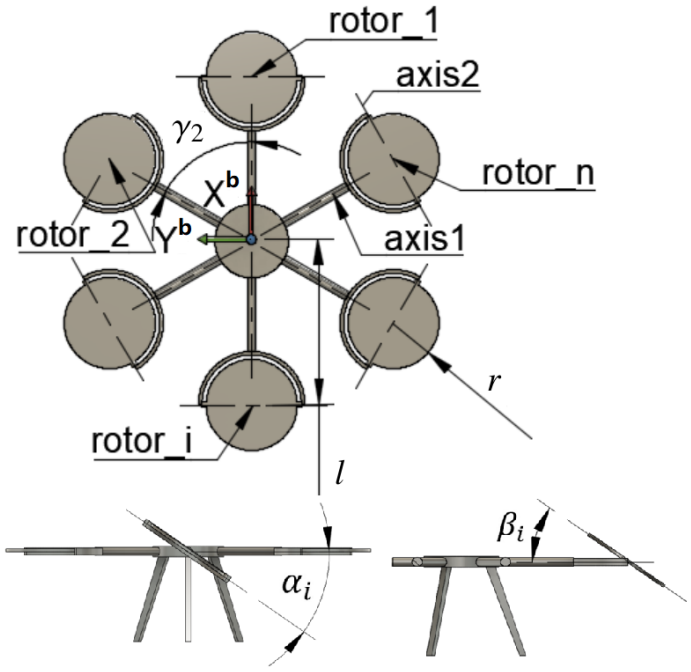

Figure 2.4 The structure of the proposed dual-axis tilting vector thrust UAV.

To develop the dynamic model of the UAV, we consider the following right-hand coordinate systems as shown in Figure 2.6.

$\{e\}$: The earth (inertial) frame with axes $X^e; Y^e; Z^e$.

$\{b\}$: The body-fixed coordinate system in which the origin coincides with the geometric center of the UAV. The axes of frame b are denoted by $X^b; Y^b; Z^b$.

$\{l_i\}$: The frame fixed to the i'th propeller with axes $X^{l_i}; Y^{l_i}$; Z^{l_i}, and $i = 1, \cdots, n$. These coordinate frames are termed as local propeller frames. The origin of each frame $\{l_i\}$ coincides with the center point of the propeller. Y^{l_i} is along the line connecting the two ends of the i'th fork, and Z^{l_i} is perpendicular to the plane of i'th propeller rotation.

The rotational matrices [7] between the defined coordinate systems are denoted by:

R_b^e: the rotational matrix from frame $\{e\}$ to frame $\{b\}$.

Figure 2.5 A prototype of the proposed dual-axis tilting vec-tor thrust UAV.

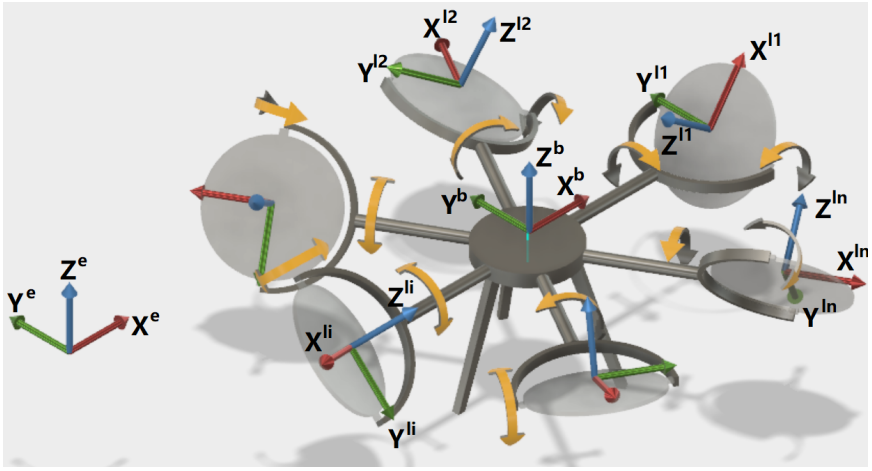

Figure 2.6 The illustration of the coordinate systems used.

$$R_b^e = \begin{bmatrix} C_\theta C_\psi & S_\theta C_\psi S_\phi - S_\psi C_\phi & S_\theta C_\psi C_\phi + S_\psi S_\phi \\ C_\theta S_\psi & S_\theta S_\psi S_\phi + C_\psi C_\phi & S_\theta S_\psi C_\phi - C_\psi S_\phi \\ -S_\theta & C_\theta S_\phi & C_\theta C_\phi \end{bmatrix}$$

where ϕ, θ,and ψ are the Euler angles of the UAV body.

$R_{l_i}^b$: the rotational matrix from frame $\{b\}$ to frame $\{l_i\}$, $i = 1, \cdots, n$.

$$R_{l_i}^b = \begin{bmatrix} C_{\gamma_i} C_{\beta_i} - S_{\gamma_i} S_{\alpha_i} S_{\beta_i} & -S_{\gamma_i} C_{\alpha_i} & C_{\gamma_i} S_{\beta_i} + C_{\beta_i} S_{\gamma_i} S_{\alpha_i} \\ S_{\gamma_i} C_{\beta_i} + C_{\gamma_i} S_{\alpha_i} S_{\beta_i} & C_{\gamma_i} C_{\alpha_i} & S_{\gamma_i} S_{\beta_i} - C_{\gamma_i} S_{\alpha_i} C_{\beta_i} \\ -C_{\alpha_i} S_{\beta_i} & S_{\alpha_i} & C_{\beta_i} C_{\alpha_i} \end{bmatrix}$$

where $C = cos$ and $S = sin$. And γ_i, α_i, β_i are the series of rotation angles from $\{b\}$ to $\{l_i\}$ around Z, X and Y axes, respectively. Among them, α_i and β_i can be freely tuned by the servos, and $\gamma_i = \frac{2\pi(i-1)}{n}$ is the fixed spacing angle of the i'th arm.

2.3 Modeling of the Fully-actuated Vector Thrust UAVs

In order to develop the equations of motion of the vector thrust UAV, we need to model the forces and torques acting on the vehicle. There are two main forces acting on the UAV: the thrust force and the gravitational force. Also, the main torques acting on the UAV are the thrust torque and the drag torque, as well as the torque caused by gravitational force acting on the center of mass.

2.3.1 The thrust force

The individual thrust force [29] expressed in local propeller frame $\{l_i\}$ is:

$$F_{p_i}^{l_i} = \begin{bmatrix} 0 & 0 & K_F {\omega_i}^2 \end{bmatrix}^T, i = 1, \cdots, n \tag{2.1}$$

where K_F is the force to speed constant of the propeller. ω_i is the rotational speed of

the i'th rotor. The thrust force of the i'th rotor expressed in body frame is thus

$$\begin{aligned} F_{p_i}^b = R_{l_i}^b F_{p_i}^{l_i} &= K_F {\omega_i}^2 \begin{bmatrix} S_{\gamma_i} S_{\alpha_i} + C_{\gamma_i} S_{\gamma_i} C_{\alpha_i} \\ -C_{\gamma_i} S_{\alpha_i} + S_{\gamma_i} S_{\beta_i} C_{\alpha_i} \\ C_{\beta_i} C_{\alpha_i} \end{bmatrix} \\ &= \begin{bmatrix} F_{p_{ix}}^b & F_{p_{iy}}^b & F_{p_{iz}}^b \end{bmatrix}^T, i = 1, \cdots, n \end{aligned} \tag{2.2}$$

where $F_{p_{ix}}^b, F_{p_{iy}}^b$ and $F_{p_{iz}}^b$ are the X, Y and Z components of the i'th thrust force vector to be optimized later. The total thrust force which equals to the sum of all individual thrust forces generated from the propellers is $F_p^b = \sum_{i=1}^{n} F_{p_i}^b$.

2.3.2 The gravitational force

The gravitational force expressed in the body frame is expressed as

$$F_g^b = R_b^{eT} \begin{bmatrix} 0 & 0 & -mg \end{bmatrix}^T = \begin{bmatrix} mgS_\theta & -mgC_\theta S_\phi & -mgC_\theta C_\phi \end{bmatrix}^T \tag{2.3}$$

where m is the total mass of the UAV, g is the gravitational acceleration.

Now, the total force acting on the UAV and expressed in the body coordinate system is described as :

$$F^b = F_p^b + F_g^b + F_\Delta^b = \begin{bmatrix} F_x^b & F_y^b & F_z^b \end{bmatrix}^T \tag{2.4}$$

where $F_\Delta^b \in R^3$ is the force uncertainty term represented in body frame.

2.3.3 The thrust torque

Each individual thrust torque, which is the torque resulting from the thrust force with respect to the center of geometry of the UAV, expressed in body frame is

$$\tau_{p_i}^b = r_i^b \times F_{p_i}^b = \begin{bmatrix} r_{ix}^b & r_{iy}^b & r_{iz}^b \end{bmatrix}^T \times \begin{bmatrix} F_{p_{ix}}^b & F_{p_{iy}}^b & F_{p_{iz}}^b \end{bmatrix}^T, i = 1, \cdots, n \tag{2.5}$$

where r_i^b is the vector pointing from the center of geometry of the UAV to the center of the i'th propeller, represented in body frame.

The total thrust torque which equals to the sum of all individual thrust torques generated from the propellers is $\tau_p^b = \sum_{i=1}^{n} \tau_{p_i}^b$.

2.3.4 The drag torque

The drag torque of each rotor is generated from the drag force that ambient air applies on a rotating propeller. In our study, the drag torque applied on the i'th propeller [29] expressed in local frame can be approximated by

$$\tau_{d_i}^{l_i} = \begin{bmatrix} 0 & 0 & D_i K_M {\omega_i}^2 \end{bmatrix}^T, i = 1, \cdots, n \tag{2.6}$$

where D_i is a constant equal to 1 when the i'th propeller rotates in clockwise direction, and equal to -1 when it rotates in counterclockwise direction; K_M is the drag torque to speed constant of the propeller.

It is easy to see that the drag torque and thrust force represented in body frame satisfy the following relationship:

$$\tau_{d_i}^b = D_i k F_{p_i}^b, i = 1, \cdots, n \tag{2.7}$$

where $k = K_M / K_F$.

The total drag torque which equals the sum of all individual drag torques generated from the propellers is $\tau_d^b = \sum_{i=1}^{n} \tau_{d_i}^b$.

2.3.5 The gravitational torque

Usually, the center of mass of the UAV is different from its geometric center, especially when the UAV is picking up objects and tilting its body. The gravitational force then

generates an additional torque acting on the UAV with respect to its geometric center:

$$\tau_g^b = r_g \times F_g^b = \begin{bmatrix} r_{gx} & r_{gy} & r_{gz} \end{bmatrix}^T \times \begin{bmatrix} mgS_\theta & -mgC_\theta S_\phi & -mgC_\theta C_\phi \end{bmatrix}^T \tag{2.8}$$

where $r_g = \begin{bmatrix} r_{gx} & r_{gy} & r_{gz} \end{bmatrix}^T$ is the location of the center of mass in body frame.

Now, the total torque acting on the UAV and expressed in the body frame is

$$\tau^b = \tau_p^b + \tau_d^b + \tau_g^b + \tau_\Delta^b = \begin{bmatrix} \tau_x^b & \tau_y^b & \tau_z^b \end{bmatrix}^T \tag{2.9}$$

where $\tau_\Delta^b \in R^3$ is the torque uncertainty term represented in body frame.

2.3.6 Dynamic model

Most literatures treat the vehicle as a rigid body with geometric center and center of mass at the same location, which does not apply to most of the real scenarios. We assume that the vector thrust UAV is a rigid body of unknown mass with its geometric center differing from the center of mass, which captures the scenario of aerial manipulation of an object with unknown weight. The total force and torque applied to the vehicle are related to the vehicle's motion through the following dynamic equations:

1) Translational motion:

$$\begin{aligned} F_x^b &= m[\dot{u} + qw - rv + \dot{q}r_{gz} - \dot{r}r_{gy} \\ &\quad +(qr_{gy} + rr_{gz})p - (q^2 + r^2)r_{gx}] \\ F_y^b &= m[\dot{v} + ru - pw + \dot{r}r_{gx} - \dot{p}r_{gz} \\ &\quad +(rr_{gz} + pr_{gx})q - (r^2 + p^2)r_{gy}] \\ F_z^b &= m[\dot{w} + pv - qu + \dot{p}r_{gy} - \dot{q}r_{gx} \\ &\quad +(pr_{gx} + qr_{gy})r - (p^2 + q^2)r_{gz}] \end{aligned} \tag{2.10}$$

where $v^b = \begin{bmatrix} u & v & w \end{bmatrix}^T$ is the velocity of the geometric center of the vehicle in body frame, $\omega^b = \begin{bmatrix} p & q & r \end{bmatrix}^T$ is the rotational velocity of the vehicle in body frame.

2) Rotational motion:

$$\begin{aligned}
\tau_x^b &= I_{xx}\dot{p} + I_{xy}\dot{q} + I_{xz}\dot{r} + (I_{zz} - I_{yy})rq + I_{yz}(q^2 - r^2) \\
&+ I_{xz}pq - I_{xy}pr + m[r_{gy}(\dot{w} + pv - qu) - r_{gz}(\dot{v} + ru - pw)] \\
\tau_y^b &= I_{yx}\dot{p} + I_{yy}\dot{q} + I_{yz}\dot{r} + (I_{xx} - I_{zz})pr + I_{xz}(r^2 - p^2) \\
&+ I_{xy}qr - I_{yz}pq + m[r_{gz}(\dot{u} + qw - rv) - r_{gx}(\dot{w} + pv - qu)] \\
\tau_z^b &= I_{zx}\dot{p} + I_{zy}\dot{q} + I_{zz}\dot{r} + (I_{yy} - I_{xx})pq + I_{xy}(p^2 - q^2) \\
&+ I_{yz}pr - I_{xz}qr + m[r_{gx}(\dot{v} + ru - pw) - r_{gy}(\dot{u} + qw - rv)]
\end{aligned} \tag{2.11}$$

where $I^b = \begin{bmatrix} I_{xx} & I_{xy} & I_{xz} \\ I_{yx} & I_{yy} & I_{yz} \\ I_{zx} & I_{zy} & I_{zz} \end{bmatrix}$ is the inertial tensor matrix of the vehicle with respect to the body frame.

3) By combining the dynamic equations (2.10), (2.11), and utilizing the force/torque expressions (2.4), (2.9), we obtain the lumped system dynamics in matrix form:

$$M\dot{\nu} = N + AU + \Delta \tag{2.12}$$

where $\nu = \begin{bmatrix} u & v & w & p & q & r \end{bmatrix}^T$ is a vector of the linear and rotational velocities of the vehicle in body frame, $U = \begin{bmatrix} F_{p1x}^b & F_{p1y}^b & F_{p1z}^b & \cdots & F_{pnx}^b & F_{pny}^b & F_{pnz}^b \end{bmatrix}^T$ is the vector of x, y, z elements of the thrust forces of the propellers expressed in body frame. Since the tilting angles α_i and β_i can be uniquely determined once the value of each F_{pi}^b is known, we can simply treat U as the control input to the dynamic system to be synthesized. $M \in R^{6\times6}$ is the lumped inertial matrix, $N \in R^{6\times1}$ is the vector of lumped

nonlinear items, $A \in R^{6\times 3n}$ is a lumped input gain matrix, $\Delta = [F_{\Delta}^{bT}, \tau_{\Delta}^{bT}]^T$ is the lumped uncertainty vector. The expressions of M, N and A are shown below:

$$M = \begin{bmatrix} m & 0 & 0 & 0 & mr_{gz} & -mr_{gy} \\ 0 & m & 0 & -mr_{gz} & 0 & mr_{gx} \\ 0 & 0 & m & mr_{gy} & -mr_{gx} & 0 \\ 0 & -mr_{gz} & mr_{gy} & I_{xx} & I_{xy} & I_{xz} \\ mr_{gz} & 0 & -mr_{gx} & I_{yx} & I_{yy} & I_{yz} \\ -mr_{gy} & mr_{gx} & 0 & I_{zx} & I_{zy} & I_{zz} \end{bmatrix}$$

$$N = \begin{bmatrix} m(-qw + rv - (qr_{gy} + rr_{gz})p + (q^2 + r^2)r_{gx}) \\ m(-ru + pw - (rr_{gz} + pr_{gx})q + (r^2 + p^2)r_{gy}) \\ m(-pv + qu - (pr_{gx} + qr_{gy})r + (p^2 + q^2)r_{gz}) \\ -(I_{zz} - I_{yy})rq - I_{yz}(q^2 - r^2) - I_{xz}pq + I_{xy}pr - m[r_{gy} \\ -(I_{xx} - I_{zz})rp - I_{xz}(r^2 - p^2) - I_{xy}qr + I_{yz}pq - m[r_{gz} \\ -(I_{yy} - I_{xx})pq - I_{xy}(p^2 - q^2) - I_{yz}pr + I_{xz}qr - m[r_{gx} \end{bmatrix}$$

$$\begin{bmatrix} +mgS_{\theta} \\ -mgC_{\theta}S_{\phi} \\ -mgC_{\theta}C_{\phi} \\ (pv - qu) - r_{gz}(ru - pw)] + mgC_{\theta}S_{\phi}r_{gz} - mgC_{\theta}C_{\phi}r_{gy} \\ (qw - rv) - r_{gx}(pv - qu)] + mgC_{\theta}C_{\phi}r_{gx} + mgS_{\theta}r_{gz} \\ (ru - pw) - r_{gy}(qw - rv)] - mgS_{\theta}r_{gy} - mgC_{\theta}S_{\phi}r_{gx} \end{bmatrix}$$

$$A = \begin{bmatrix} 1 & 0 & 0 & 1 & 0 & 0 & \cdots & 1 & 0 & 0 \\ 0 & 1 & 0 & 0 & 1 & 0 & \cdots & 0 & 1 & 0 \\ 0 & 0 & 1 & 0 & 0 & 1 & \cdots & 0 & 0 & 1 \\ D_1k & -r_{1z} & r_{1y} & D_2k & -r_{2z} & r_{2y} & \cdots & D_nk & -r_{nz} & r_{ny} \\ r_{1z} & D_1k & -r_{1x} & r_{2z} & D_2k & -r_{2x} & \cdots & r_{nz} & D_nk & -r_{nx} \\ -r_{1y} & r_{1x} & D_1k & -r_{2y} & r_{2x} & D_2k & \cdots & -r_{ny} & r_{nx} & D_nk \end{bmatrix}$$

2.3.7 Overall system model including kinematics and dynamics

Since the objective is to control the vehicle's position and orientation in inertial frame, we need to relate the position and orientation variables to the body frame velocity vector ν. The relationship is given by the following two kinematic equations:

$$\dot{\lambda}^e = R_b^e \nu^b; \quad \dot{\eta}^e = \Psi \omega^b \tag{2.13}$$

where $\lambda^e = \begin{bmatrix} x & y & z \end{bmatrix}^T$ is the position of the geometric center of the vehicle in inertial frame, $\eta^e = \begin{bmatrix} \phi & \theta & \psi \end{bmatrix}^T$ is the attitude vector of the vehicle expressed in inertial frame, $\Psi = \begin{bmatrix} 1 & S_\phi T_\theta & C_\phi T_\theta \\ 0 & C_\phi & -S_\phi \\ 0 & \frac{S_\phi}{C_\theta} & \frac{C_\phi}{C_\theta} \end{bmatrix}$ is the transformation matrix at kinematic level.

Combining the kinematics and dynamics, the overall equations of motion of the system are described by:

$$\begin{aligned} \dot{\chi} &= \Lambda \nu \\ M\dot{\nu} &= N + AU + \Delta \end{aligned} \tag{2.14}$$

where $\chi = \begin{bmatrix} \lambda^e & \eta^e \end{bmatrix}^T$ is the position and orientation variables in inertial frame, $\Lambda = \begin{bmatrix} R_b^e & 0 \\ 0 & \Psi \end{bmatrix}$.

2.4 Adaptive Robust Control of the Fully-actuated Vector Thrust UAVs

For control design, we consider the $6-DOF$ motion tracking problem in this paper, i.e., the objective is to synthesize a control input U such that the $\chi(t) \rightarrow \chi_d(t)$ as accurately as possible despite the presence of the uncertain nonlinearity Δ as well as the unknown parameters in M and N. Since $3n > 6$, the system has actuator redundancy. Thus, we develop the following two-step strategy to solve the problem.

- Step 1. Defining $B = AU$ as the virtual control input, which is also recognized as the six-axis force/torque wrench in body frame generated by all the propellers, we design an adaptive robust control law for B such that $\chi(t)$ tracks $\chi_d(t)$.
- Step 2. A constrained optimization problem is solved to obtain U such that $B = AU$ is satisfied while the power consumption of the vehicle is minimized.

2.4.1 Adaptive robust control for UAVs

Design Models and Assumption To fully capture the effect of the inertial parametric uncertainties on the system when the vehicle grabs an unknown object, we define a vector Θ consisting of 10 unknown inertial variables: $\Theta = \begin{bmatrix} m & mr_{gx} & mr_{gy} & mr_{gz} & I_{xx} & I_{xy} & I_{xz} & I_{yy} & I_{yz} & I_{zz} \end{bmatrix}^T$.

From the expressions of M and N, it is seen that each entry of M and N is linear in terms of Θ, i.e., it can be represented as the dot product of Θ and a known regressor function φ, which can be easily derived from the expressions of M and N in the dynamic model section. Thus, M and N can be expressed as:

$M^T(\Theta) = \begin{bmatrix} \varphi_{M1}^T\Theta & \cdots & \varphi_{M6}^T\Theta \end{bmatrix}$, $N(\chi, \nu, \Theta) = \varphi_N^T(\chi, \nu)\Theta$,

where $\varphi_{Mi} \in R^{10\times 6}$ and $\varphi_N \in R^{10\times 6}$.

For simplicity, the following notations are used: $\bullet_i$ for the ith component of the vector $\bullet$, $\bullet_{min}$ for the minimum value of $\bullet$, and $\bullet_{max}$ for the maximum value of $\bullet$. The operation $\leq$ for two vectors is performed in terms of the corresponding elements of the vectors. The following practical assumption is made on Θ and Δ [30].

Assumption 1: The extent of the parametric uncertainties and uncertain nonlinearities are known, i.e.,

$$\begin{aligned} \Theta \in \Omega_\Theta &\triangleq \{\Theta : \Theta_{min} \leq \Theta \leq \Theta_{max}\} \\ \Delta \in \Omega_\Delta &\triangleq \{\Delta : |\Delta| \leq \delta_\Delta\} \end{aligned} \tag{2.15}$$

where $\Theta_{min} = [\Theta_{1min}, \cdots, \Theta_{10min}]^T$, $\Theta_{max} = [\Theta_{1max}, \cdots, \Theta_{10max}]^T$, and δ_Δ are known.

Let $\hat{\Theta}$ denote the estimate of Θ and $\tilde{\Theta}$ the estimation error (i.e., $\tilde{\Theta} = \hat{\Theta} - \Theta$). In view of (5.8), the following adaptation law with discontinuous projection modification is used:

$$\dot{\hat{\Theta}} = Proj_{\hat{\Theta}}(\Gamma\sigma) \tag{2.16}$$

where $\Gamma > 0$ is a diagonal matrix, σ is an adaptation function to be synthesized later. The projection mapping

$Proj_{\hat{\Theta}}(\bullet) = [\ Proj_{\hat{\Theta}_1}(\bullet) \quad Proj_{\hat{\Theta}_2}(\bullet) \quad \cdots Proj_{\hat{\Theta}_{10}}(\bullet)]^T$ is defined as

$$Proj_{\hat{\Theta}_i}(\bullet_i) = \begin{cases} 0, & \text{if } \hat{\Theta}_i = \theta_{imax} \text{ and } \bullet_i > 0 \\ 0, & \text{if } \hat{\Theta}_i = \theta_{imin} \text{ and } \bullet_i < 0 \\ \bullet_i, & \text{otherwise} \end{cases} \tag{2.17}$$

It can be shown that for the adaptation function Θ, the projection mapping used in (2.16) guarantees

$$\begin{aligned} &\textbf{P1} \qquad \hat{\Theta} \in \Omega_\Theta \triangleq \{\hat{\Theta} : \Theta_{min} \le \hat{\Theta} \le \Theta_{max}\} \\ &\textbf{P2} \qquad \tilde{\Theta}^T(\Gamma^{-1} Proj_{\hat{\Theta}}(\Gamma\sigma) - \sigma) \le 0, \quad \forall\sigma \end{aligned} \tag{2.18}$$

ARC Controller Design To develop the adaptive robust control law, a switching-function-like quantity is defined as

$$s = \Lambda^{-1}(\dot{e} + k_1 e) = v - \Lambda^{-1}\dot{\chi}_d + \Lambda^{-1}k_1 e \tag{2.19}$$

where $e = \chi - \chi_d$ is the output tracking error, $k_1 > 0$ is a diagonal feedback gain matrix. Clearly, if s is small or converges to zero exponentially, then the output tracking error e will be small or converge to zero exponentially. So the rest of the

design is to make $s \to 0$. Differentiating (2.19) generates

$$\begin{aligned} & M\dot{s} \\ &= M\dot{v} - M[\dot{\Lambda^{-1}}\dot{\chi}_d + \Lambda^{-1}\ddot{\chi}_d - \dot{\Lambda^{-1}}k_1 e - \Lambda^{-1}k_1(\Lambda v - \dot{\chi}_d)] \\ &= N + B + \Delta - M[\dot{\Lambda^{-1}}(\dot{\chi}_d - k_1 e) + \Lambda^{-1}(\ddot{\chi}_d - k_1\Lambda v + k_1\dot{\chi}_d)] \end{aligned} \tag{2.20}$$

Let $Z = \dot{\Lambda^{-1}}(\dot{\chi}_d - k_1 e) + \Lambda^{-1}(\ddot{\chi}_d - k_1\Lambda v + k_1\dot{\chi}_d)$, using the parametric expressions of M and N, the above equation can be presented as

$$M\dot{s} = B + \Phi^T\Theta + \Delta \tag{2.21}$$

where $\Phi = -[\varphi_{M1}Z \cdots \varphi_{M6}Z] + \varphi_N$. Noting the structure of (2.21), the following ARC control law is proposed:

$$B = B_a + B_s, \qquad B_a = -\Phi^T\hat{\Theta} \tag{2.22}$$

where B_a is the adjustable model compensation needed for achieving perfect tracking, and B_s is a robust control law to be synthesized later. Substituting (2.22) into (2.21), and then simplifying the resulting expression, one obtains

$$M\dot{s} = B_s - \Phi^T\tilde{\Theta} + \Delta \tag{2.23}$$

The robust control function B_s consists of two terms given by

$$B_s = B_{s1} + B_{s2}, \qquad B_{s1} = -k_2 s \tag{2.24}$$

where B_{s1} is used to stabilize the nominal system, which is a simple proportional feedback with $k_2 > 0$ being the diagonal feedback gain matrix in this case; B_{s2} is a robust feedback used to attenuate the effect of model uncertainties. Noting Assumption 1 and P1 of (2.18), there always exists a B_{s2} such that the following two conditions

are satisfied:

$$\begin{array}{ll} 1 & s\{B_{s2} - \Phi^T\tilde{\Theta} + \Delta\} \leq \epsilon \\ 2 & sB_{s2} \leq 0 \end{array} \tag{2.25}$$

where ϵ is a design parameter which can be arbitrarily small and B_{s2} can be chosen according to the previous research [30].

Theorem 1: If the adaptation function in (2.16) is chosen as

$$\sigma = \Phi s \tag{2.26}$$

then the ARC control law (2.22) guarantees the following. 1) In general, all signals are bounded. Furthermore, the positive definite function V_s defined by

$$V_s = \frac{1}{2}Ms^2 \tag{2.27}$$

is bounded above by

$$V_s \leq exp(-\lambda t)V_s(0) + \frac{\epsilon}{\lambda}[1 - exp(-\lambda t)] \tag{2.28}$$

where $\lambda = 2k_{2min}/\lambda_{max}(M)$, k_{2min} is the minimum value of all the entries in k_2, $\lambda_{max}(M)$ is the maximum eigenvalue of matrix M .

2) If after a finite time t_0, there exist parametric uncertainties only(i.e., $\Delta = 0, \forall t \geq t_0$), then, in addition to results in 1), zero final tracking error is also achieved, i.e., $e \to 0$ and $s \to 0$ as $t \to \infty$.

The proof of the above theorem can be worked out in a similar way as in [30]. It is noted that, in order to enhance the performance of parameter adaptation, an Indirect Adaptive Robust Control (IARC) could also be used in which the unknown parameters are estimated through the recursive least squares algorithm [31].

2.4.2 Constrained optimization

The optimization problem has individual thrust vectors as the variables, and the instantaneous power consumption as the objective function. From the Step 1 of ARC design, in order to achieve the desired six-dimensional force wrench generated from the control design step, the following linear constraint must be satisfied:

$$AU = B \tag{2.29}$$

Furthermore, the objective function is the instantaneous total power consumption of a UAV with n rotors, is expressed as

$$\begin{aligned} f(U) = &\sqrt{U(1)^2 + U(2)^2 + U(3)^2} \\ &+ \cdots + \sqrt{U(3n-2)^2 + U(3n-1)^2 + U(3n)^2}, \end{aligned} \tag{2.30}$$

which is a convex function of U. Thus, the optimization problem can be formulated as

$$\begin{aligned} &\min_U f(U) \\ &s.t. \\ &AU = B. \end{aligned} \tag{2.31}$$

This problem has a convex objective function and all the constraints are linear. A variety of iterative algorithms may be applied to obtain the global minima [32].

After obtaining the individual thrust force vectors in the body frame, we can solve for ω_i, tilting angles α_i, β_i as

$$\begin{aligned} \omega_i &= \sqrt{||F_{pi}^b||/k_f} \\ \beta_i &= arcsin[(F_{p_{ix}}^b C_{\gamma_i} + F_{p_{iy}}^b S_{\gamma_i})/||F_{p_i}^b||] \\ \alpha_i &= arctan[(F_{p_{ix}}^b S_{\gamma_i} - F_{p_{iy}}^b C_{\gamma_i})/F_{p_{iz}}^b], i = 1, \cdots, n \end{aligned} \tag{2.32}$$

2.5 Simulation Results

In the simulation, a model of a Vector Thrust Tricopter UAV with three thrust vectoring propellers is constructed. The proposed ARC controller and thrust force

optimization algorithm are applied to make the vehicle optimally track the desired time-varying position and orientation trajectories while the power consumption of the vehicle is minimized. The parameters used in simulation are: $m = 0.51kg; l = 0.33m; x(0) = 0.5m; y(0) = 0.5m; z(0) = 0.5m; \phi(0) = 0.5rad; \theta(0) = 0.5rad; \psi(0) = 0.5rad; r_{gx} = 0.03676m; r_{gy} = 0.03676m; r_{gz} = 0; I_{xx} = 0.0083kg \cdot m^2;$
$I_{yy} = 0.0083kg \cdot m^2; I_{zz} = 0.0166kg \cdot m^2; I_{xy} = -0.00093kg \cdot m^2; I_{xz} = 0; I_{yz} = 0; I_{yx} = -0.00093kg \cdot m^2; I_{zx} = 0; I_{zy} = 0; D_1 = 1; D_2 = -1; D_3 = 1; k = 0.016; k_e = 1.$

The desired time-varying position trajectory vector in inertial frame for this simulation is $\lambda^d = (sin(0.5t), cos(0.5t), 0.1t)m$. The desired time-varying attitude vector in inertial frame is $\eta^d = (sin(0.5t), sin(0.5t), sin(0.5t))rad$. The simulation and the real-time tracking results for position and attitude tracking are illustrated in Figure 2.7. In addition, the parameter estimates shown in Figure 2.8 and 2.9 generally converge to the actual values despite the presence of uncertainties in the system.

In order to demonstrate the advantage of power consumption of the proposed design with the force optimization algorithm, we compare our proposed method (E1) with the traditional one-axis tilting tricopter, where all the propellers can only be tilted about each arm's axis (E2). In this case, there are six actuation variables, which equal to the number of DOFs of the vehicle's body. Thus, the thrust force and tilting angle for each propeller can be uniquely calculated without any optimization. A power consumption rate factor $E = k_e f(X)$ is calculated to indicate the power consumption rate during the same trajectory tracking process for both E1 and E2, where k_e is a constant representing the relation between sum of thrust forces and power consumption rate, as can be seen from Figure 2.10, our proposed design with force optimization (E1) achieves much small power consumption compared to E2, especially when the roll or pitch angle of the vehicle body is large.

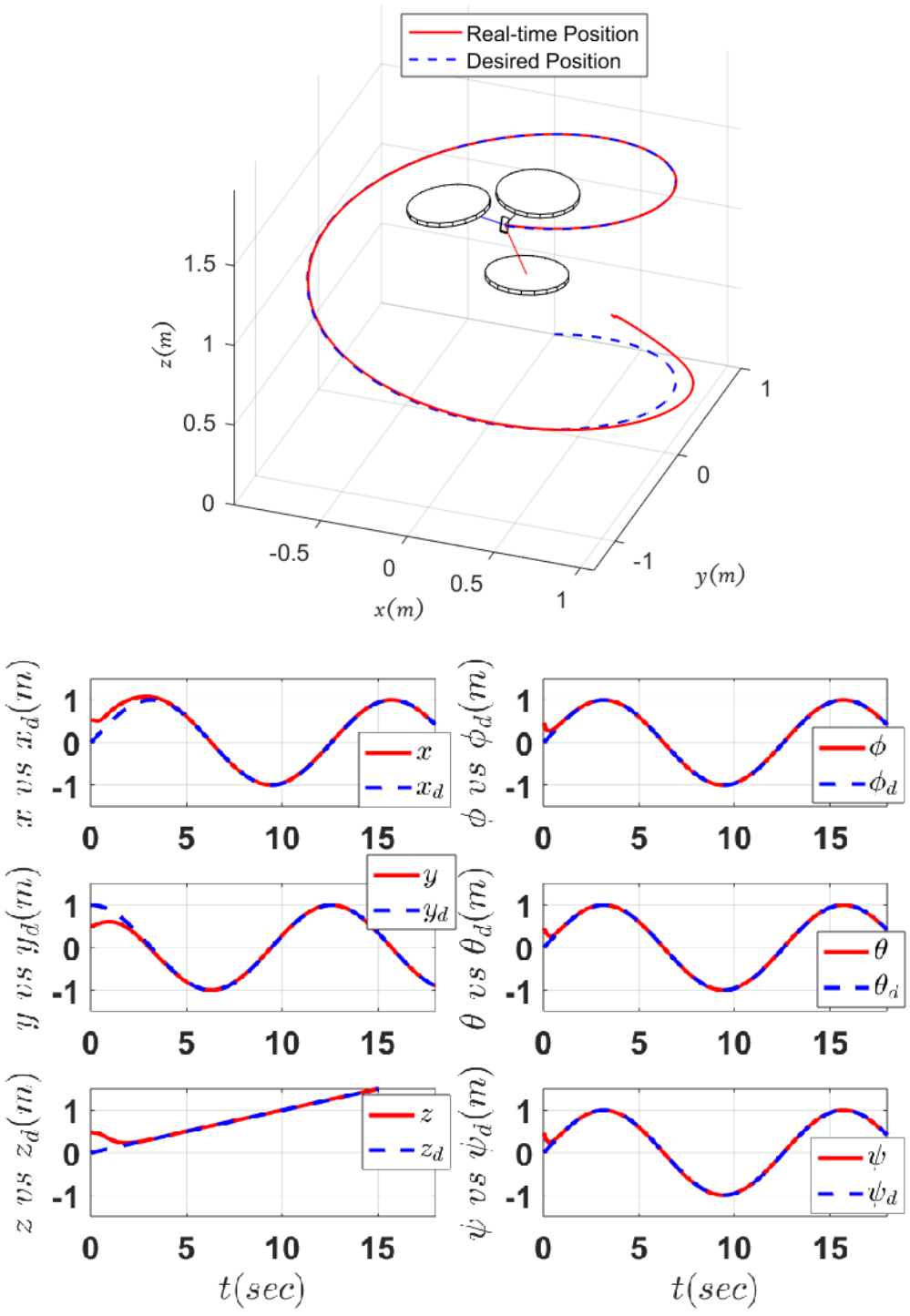

Figure 2.7 3D space tracking and the real-time tracking results for the x,y,z positions and the altitude angles.

2.6 Conclusions

In this study, we proposed an energy-efficient adaptive robust tracking control for a class of novel vector thrust UAVs. The mechanical structure of the vector thrust UAV

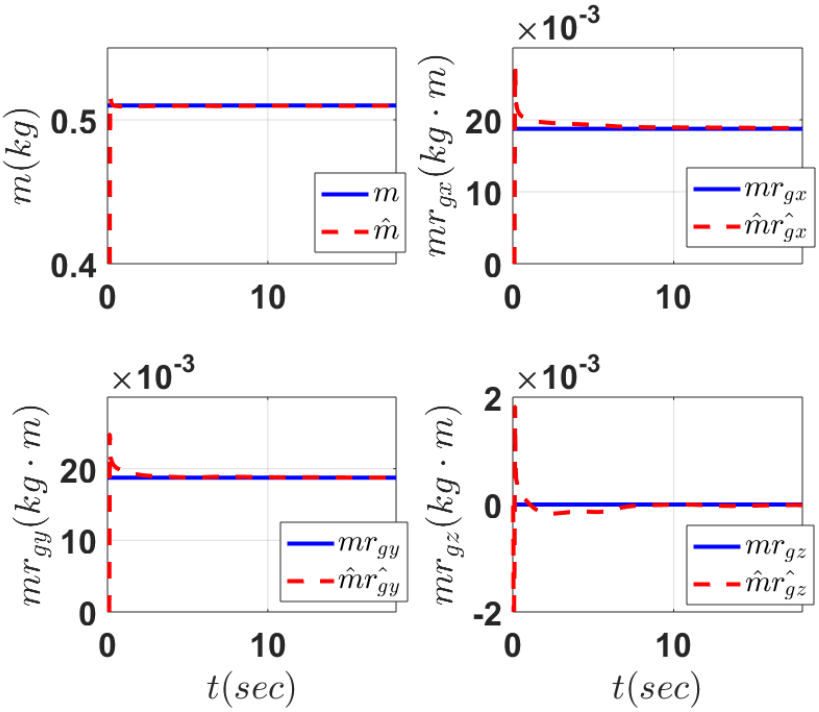

Figure 2.8 The estimates of the mass and the x,y,z positions of the center of mass.

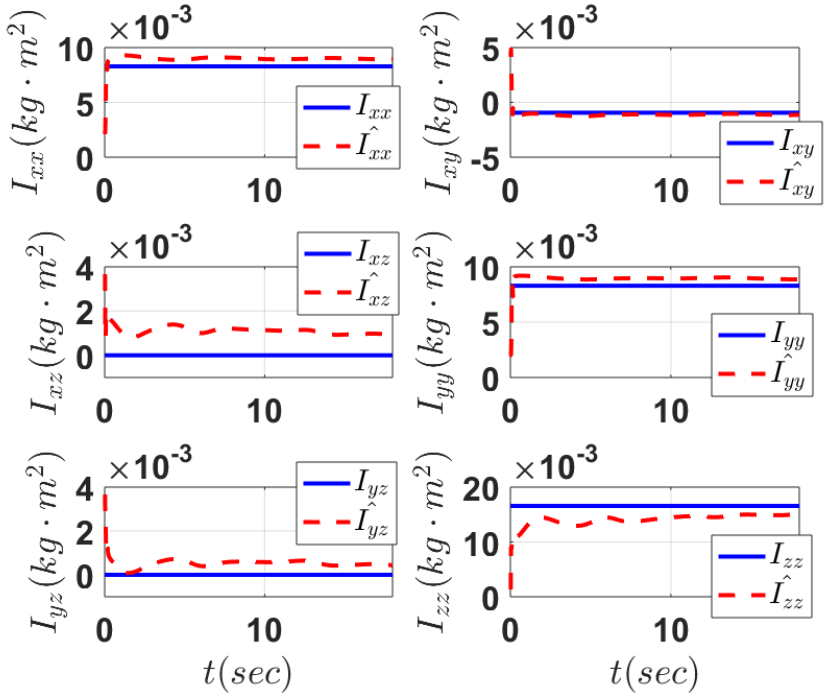

Figure 2.9 The estimates of the moment of inertia.

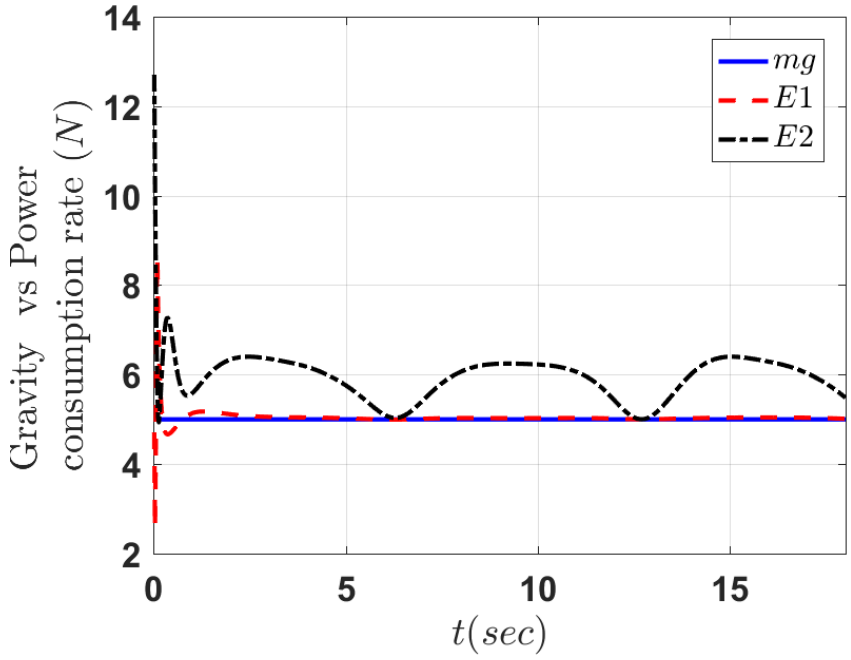

Figure 2.10 Power consumption rates when tracking the spiral trajectory: Red dashed line - the vector thrust tricopter UAV. Black dotted line - a tricopter with rotors tilting only about the arm axial directions. Blue solid line - benchmark power consumption when the vehicle is hovering (equals to the gravity multiplied by the factor k_e).

with all propellers able to tilt about two perpendicular axes was first presented. Based on this design, we formulated the dynamic model of the vehicle with arbitrary number of such propellers in the presence of parametric uncertainties including unknown moment of inertia, mass and center of mass, which previous literature have hardly dealt with. Next, an adaptive robust control was designed for accurate trajectory tracking in the presence of various types of uncertainties. A thrust force optimization problem minimizing the instantaneous power consumption while achieving the desired body force wrench was then solved to obtain the individual thrust force vectors of the rotors. From the simulations, the resulting controller achieved a guaranteed transient performance and final tracking accuracy in the presence of uncertainties. In addition, a higher efficiency of energy utilization can be achieved with the proposed thrust force optimization strategy.

CHAPTER 3

6-DOF AUTOMATED FLIGHT TESTING

3.1 Introduction

After a new vehicle is designed and prototyped, an initial flight testing is necessary to validate the functionality and performance of the vehicle under an emulated free flight environment. A safe and realistic flight testing can effectively guide the redesign of the UAV for performance improvement, reduce the labor cost, and is thus critical in the success of the product development. Unfortunately, the study of flight testing strategy has often been overlooked. Due to possible flaws in the control design, uncertainties in the aerodynamics, external disturbances, and failure of the onboard electronics and communication, the vehicle could become unstable at any time, making the initial flight testing a risky task. In most of the UAV research, the flight testing was conducted by letting the vehicle fly freely in an enclosed area prohibited to humans [33, 34, 35]. However, the crash of the vehicle in an unstable run may lead to damage of the equipment and infrastructures.

To ensure safety and reduce sensor cost in initial flight testing, a few studies focused on the design of test benches on which the vehicle is mounted during the flight. In [36], an indoor micro quadrotor was developed and tested on an OS4 test bench using a universal joint as shown in Figure 3.1(a), which can only be rotated about three axes. The spherical joint rig has also been used as the platform for various UAV flight testing, as shown in Figure 3.1(c), for instance the quadrotor design and control in [37, 38], and the modeling and implementation of a tri-rotor flying robot in [39]. A quadcopter test bench was designed to test up-and-down movement as shown in Figure 3.1(b). However, the movement of the vehicle on certain degrees of freedom is constrained, making the 6-DOF flight testing impossible. Moreover, the inertia and gravity forces of the platform are not compensated during the flight testing due

to the passive nature of the platform. In this chapter, we study a new method of

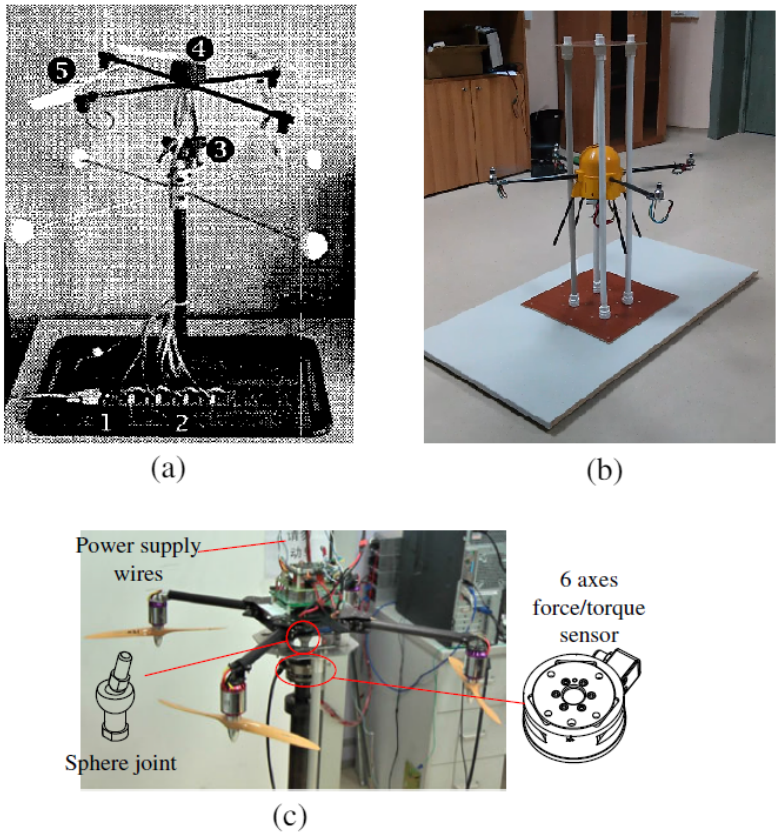

Figure 3.1 Existing test benches developed for initial flight testing: (a) The OS4 test bench using a universal joint; (b) The vertical motion test bench which constrains all other DOFs; (c) The flight test platform using a spherical joint rig.

flight testing of VTOL UAVs by using an articulated humanoid robot arm with a 6-axis force/torque sensor as the test platform. Specifically, the vehicle is mounted to the end-effector of the robot arm through the force/torque sensor. The robot arm carries the vehicle and follows its movement quickly and precisely during the flight testing. To test the performance of the vehicle controller in an emulated free flight environment while ensuring safety, we develop a dual-module control approach to control the robot arm so that the 6-DOF free flight emulation and safety can be ensured simultaneously, which has not been achieved before. Furthermore, with such a platform, the robot end-effector position/orientation can be used to localize the vehicle for its controller implementation, avoiding the use of multi-camera motion

capture systems which are expensive and complicated to set up. A set of experimental verifications show that our system can indeed achieve 6-DOF free flight emulation and guarantee safety simultaneously.

3.2 System Architecture

The system we develop in this research for 6-DOF flight testing automation consists of an articulated humanoid robot arm, a UAV with onboard flight controller to be tested, a six-axis force/torque sensor, and a controller, as shown in Figure 3.2. The vehicle is mounted onto the end-effector through a 6-axis force/torque sensor. During the flight testing, the vehicle flies within the range of motion of the robot arm, while the robot arm closely follows the movement of the vehicle such that the measured interaction force/torque in six dimensions is maintained around zero. In order to achieve the coordinated movement between the robot arm and the vehicle, a host computer runs the robot control algorithm and synchronizes it with the onboard flight controller of the vehicle through wireless communication.

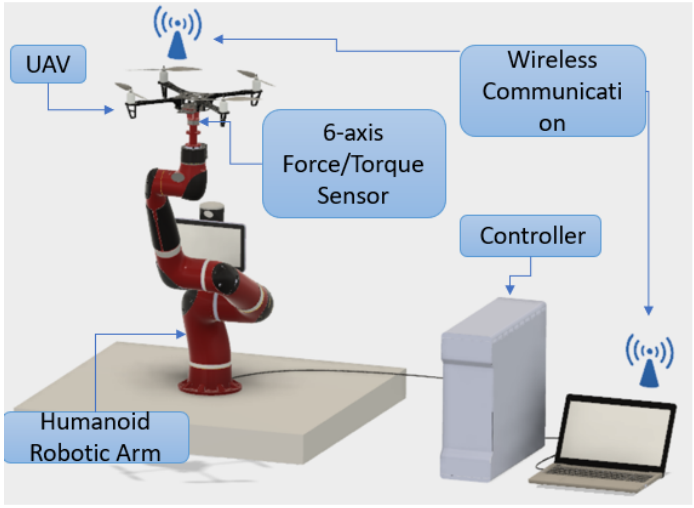

Figure 3.2 The proposed system for 6-DOF flight testing automation.

3.3 System Dynamics and Control Design

3.3.1 System dynamics

In the developed flight testing system, the vehicle is assumed to be a rigid body in the 3D Euclidean space. The humanoid robot arm is assumed to be a serial manipulator with rigid joints. The connection between the vehicle and the end-effector of the robot (including the force/torque sensor and the mounting fixture) is modeled by a 6-DOF spring.

Specifically, the translational and rotational equations of motion of the vehicle are:

$$\begin{aligned} m\ddot{x}_v &= F_v - F_s - mg + \Delta_{vt} \\ \dot{\eta}_v &= \Psi(\eta_v)\omega_v^v \\ I_v^v\dot{\omega}_v^v &= \tau_v^v - \tau_n^v - R_v^{eT}\tau_s^e + \Delta_{vr}, \end{aligned} \tag{3.1}$$

where $x_v \in R^3$ is the position vector. $\eta_v = \begin{bmatrix} \phi_v & \theta_v & \psi_v \end{bmatrix}^T$ is the attitude vector of the vehicle. $\Psi(\eta_v) = \begin{bmatrix} 1 & S_{\phi_v}T_{\theta_v} & C_{\phi_v}T_{\theta_v} \\ 0 & C_{\phi_v} & -S_{\phi_v} \\ 0 & \frac{S_{\phi_v}}{C_{\theta_v}} & \frac{C_{\phi_v}}{C_{\theta_v}} \end{bmatrix}$ is the kinematic transformation matrix. m is the mass of the vehicle. $g \in R^3$ is the vector of the gravitational acceleration. $I_v^v \in R^{3\times3}$ is the moment of inertia matrix. $F_v \in R^3$ is the input force acting on the vehicle, $F_s \in R^3$ is the spring force measured by the force sensor. $\tau_v^v \in R^3$ is the input torque acting on the vehicle represented in the vehicle's body frame. $\tau_n^v \in R^3$ is the nonlinear Coriolis force. $\tau_s^e \in R^3$ is the spring torque measured by the force sensor represented in the vehicle's body frame. $R_j^i \in R^{3\times3}$ is the rotation matrix from frame $\{i\}$ to frame $\{j\}$, where "e" indicates the robot end-effector frame, "v" indicates the vehicle's body frame, and "0" indicates the inertia frame. $\Delta_{vt},\ \Delta_{vr} \in R^3$ are the lumped translational and rotational uncertainties which are assumed to be bounded. For simplicity and

easy illustration, we assume that the force/torque sensor connects to the vehicle at its center of mass.

According to [40], the spring force F_s and the spring torque τ_s^e in the robot end-effector frame can be represented as

$$\begin{aligned} F_s &= K_{st}(x_v - x_e), \\ \tau_s^e &= \Psi(\eta_{ev})^{-1} K_{sr} \eta_{ev}, \\ &\approx K_{sr} \eta_{ev} \end{aligned} \tag{3.2}$$

where $K_{st},\ K_{sr} \in R^{3\times3}$ are diagonal matrices representing translational and rotational stiffnesses. η_{ev} is the relative attitude vector of the vehicle w.r.t. the robot end-effector which is a function of the relative rotation matrix, i.e., $\eta_{ev} = \eta_{ev}(R_v^e)$. As explained in [40], for small angular displacement η_{ev} as a result of high stiffness K_{sr}, $\Psi(\eta_{ev})$ can be treated as the identity matrix I.

In this chapter, we assume that the robot is operating in the velocity control mode, i.e., the joint velocities $\dot{q} \in R^n$ of the robot can be directly set and treated as the control input. Most of the industrial robot manipulators available in the market have their torque-level control algorithm embedded in the firmware, while the end-users are provided with the velocity command interface that is sufficiently fast. By commanding the joint velocities, the complicated robot dynamics can be bypassed (which is actually taken into account in the embeded torque-level control). The control law is thus much simpler, safer and less prone to programming mistakes.

The kinematic relationship between the control input $\dot{q}$ and the end-effector velocity is governed by the following equation:

$$\begin{bmatrix} \dot{x}_e \\ \omega_e \end{bmatrix} = J\dot{q} = \begin{bmatrix} J_t \\ J_r \end{bmatrix} \dot{q}, \tag{3.3}$$

where $J \in R^{6\times n}$ is the Jacobian matrix of the robot end-effector. $\dot{x}_e \in R^3$ and $\omega_e \in R^3$ are the linear and angular velocities of the end-effector represented in inertia frame.

When $n \geq 6$ and the robot arm is not at singular poses, the joint velocities can be determined from the end-effector velocity via the following inverse kinematics formula:

$$\dot{q} = (JJ^T)^{-1} J \begin{bmatrix} \dot{x}_e \\ \omega_e \end{bmatrix} \tag{3.4}$$

Thus, to synthesize the joint velocity input, we only need to design $\dot{x}_e$ and ω_e.

3.3.2 Control design

In this section, we propose a dual-module control structure to achieve an emulated free flight environment while ensuring safety. The control architecture is illustrated in Figure 3.3. Specifically, there are two modules in the control loop. The regular force control module implements a damping force control with feedforward compensation to regulate the interaction force between the robot end-effector and the vehicle towards zero, so that the vehicle flies freely in the air as if it is not attached to the robot. The safety module keeps the vehicle within a predefined safety region by stopping the motion of the robot arm immediately when the vehicle is about to out of the safety boundary. The details regarding the design of each module are presented below.

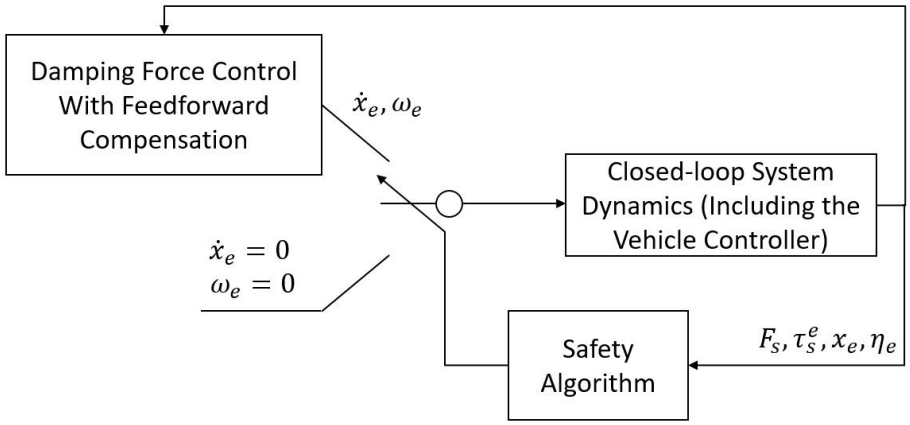

Figure 3.3 The architecture of the proposed control strategy.

Regular force control module In order to regulate the interaction force and torque towards zero, the dynamics of the F_s and τ_s need to be obtained and related to the end-effector velocity variables $\dot{x}_e$ and ω_e, and subsequently the control input $\dot{q}$:

$$\begin{aligned} \dot{F}_s &= K_{st}(\dot{x}_v - \dot{x}_e) \\ \dot{\tau}_s^e &= K_{sr}\dot{\eta}_{ev} \quad \approx K_{sr}(\omega_v^v - \omega_e^e). \end{aligned} \tag{3.5}$$

Again, the assumption that η_{ev} is small is used, which leads to $R_v^0 \approx R_e^0$.

A well-known choice of $\dot{x}_e$ and ω_e to minimize F_s and τ_s^e is the so-called "generalized damper" or "damping control" [41]:

$$\begin{aligned} \dot{x}_e &= k_t F_s \\ \omega_e^e &= k_r \tau_s^e, \end{aligned} \tag{3.6}$$

where k_t and k_r are the control gains or "the artificial damping coefficients" in the translational and rotational directions, respectively. With the damping control, the closed-loop force dynamics becomes

$$\begin{aligned} \dot{F}_s + K_{st}k_t F_s &= K_{st}\dot{x}_v \\ \dot{\tau}_s^e + K_{sr}k_r\tau_s^e &= K_{sr}\omega_v^v. \end{aligned} \tag{3.7}$$

The closed loop force/torque dynamics has $\dot{x}_v$ and ω_v^v as the external uncertainty input, which may result in a large force/torque residual when the vehicle is controlled to track a changing velocity command. To further minimize the interaction force/torque, we propose a direct force control law with feedforward compensation:

$$\begin{aligned} \dot{x}_e &= k_t F_s + \dot{x}_{vd} \\ \omega_e^e &= k_r \tau_s^e + \omega_{vd}^v, \end{aligned} \tag{3.8}$$

under which the closed-loop force/torque dynamics becomes

$$\begin{aligned} \dot{F}_s + K_{st}k_t F_s &= K_{st}(\dot{x}_v - \dot{x}_{vd}) \\ \dot{\tau}_s^e + K_{sr}k_r\tau_s^e &= K_{sr}(\omega_v^v - \omega_{vd}^v). \end{aligned} \tag{3.9}$$

In the above, $\dot{x}_{vd}$ and ω^v_{vd} are the "desired" velocity profiles the vehicle is commanded to follow. Such type of method appeared before in a similar fashion in control theory, and was termed as "desired compensation" [42]. Compared to using actual measurements or estimated variables from an observer, the desired compensation method is less sensitive to system uncertainties, and is able to generate a smoother response and smaller steady-state tracking error.

To obtain the desired velocity profiles $\dot{x}_{vd}$ and ω^v_{vd}, we need to know the desired trajectory the vehicle is controlled to move along. Let the vehicle controller be

$$F_v = F_v(x_v, \dot{x}_v, \eta_v, \omega^v_v, t) \tag{3.10}$$

$$\tau^v_v = \tau^v_v(x_v, \dot{x}_v, \eta_v, \omega^v_v, t), \tag{3.11}$$

The desired signals $\dot{x}_{vd}$ and ω^v_{vd} are obtained by solving the following "desired" closed-loop dynamics excluding all the uncertainties and spring force/torque in real time:

$$\begin{aligned} m\ddot{x}_{vd} &= F_v(x_{vd}, \dot{x}_{vd}, \eta_{vd}, \omega^v_{vd}, t) - mg \\ \dot{\eta}_{vd} &= \Psi(\eta_{vd})\omega^v_{vd} \\ I^v_v \dot{\omega}^v_{vd} &= \tau^v_{vd}(x_{vd}, \dot{x}_{vd}, \eta_{vd}, \omega^v_{vd}, t) - \tau^v_{nd}. \end{aligned} \tag{3.12}$$

In the experiment, since (3.12) is free of disturbance terms, it can be implemented exactly in the host computer, and provides the desired velocity signals $\dot{x}_{vd}(t)$ and $\omega^v_{vd}(t)$ at any time instance t.

The justification of the closed-loop stability requires non-trivial work, because that the entire closed-loop flight testing system consists of two components: the closed-loop vehicle dynamics under the vehicle flight control law (3.10), and the closed-loop spring force/torque dynamics (3.9) under the proposed force control law (3.8) for the robot end-effector. The first component has $(-F_s, -\tau^e_s)$ and other uncertainties as the input and $(\dot{x}_v - \dot{x}_{vd}, \omega^v_v - \omega^v_{vd})$ as the output, while the second component has $(\dot{x}_v - \dot{x}_{vd}, \omega^v_v - \omega^v_{vd})$ as the input and (F_s, τ^e_s) as the output. The two

components form a negative feedback structure, as shown in Figure 3.4. It is clear

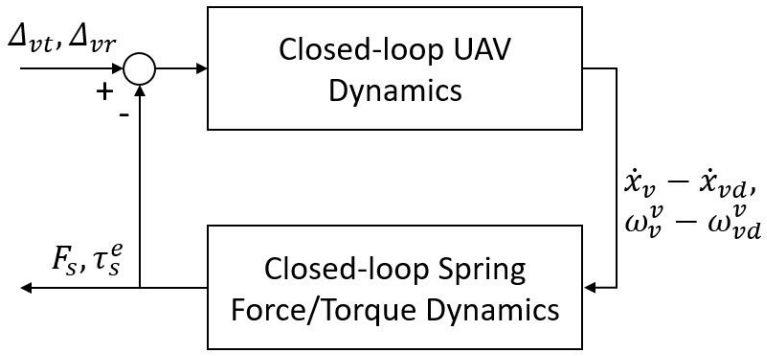

Figure 3.4 The feedback connection of the vehicle subsystem and the spring force/torque subsystem after the controllers for both have been designed.

that for such type of system with feedback connected subcomponents, the stability requires more than the individual stability of both subcomponents. To proceed, we introduce a long-existing yet important concept - passivity [43]: A dynamic system

$$\dot{x} = f(x, u) \tag{3.13}$$

$$y = h(x, u) \tag{3.14}$$

where $u \in R^p$ is the input, $x \in R^n$ is the state, and $y \in R^p$, is said to be passive if there exists a continuously differentiable function $V(x)$ such that

$$u^T y \geq \dot{V} = \frac{\partial V}{\partial x}, \ \forall (x, u) \in R^n \times R^p. \tag{3.15}$$

Furthermore, it is δ-output strictly passive if

$$u^T y \geq \dot{V} + \delta y^T y, \ y^T \rho(y) > 0, \ \forall y \neq 0, \tag{3.16}$$

where $\delta > 0$ is a constant. Intuitively, a system being passive is always dissipating energy internally since the rate of energy increase $\dot{V}$ is always no greater than the external power input $u^T y$. The definition of δ-output strictly passive specifies a special

class of passive systems that possesses more useful properties. The following theorem is a direct result from Lemma 6.8 in [43]: For the feedback connected structure in Figure 3.4, if both the closed-loop vehicle dynamics under the vehicle control law (3.10) and the closed-loop spring force/torque dynamics (3.9) under the proposed force control law are δ-output strictly passive, then we have the following two results:

1. If the external uncertainties (Δ_{vt}, Δ_{vr}) are zero, then $F_s, \tau_s^e \to 0$ as $t \to \infty$.
2. The entire closed-loop system from the uncertainty input (Δ_{vt}, Δ_{vr}) to the output force/torque (F_s, τ_s^e) is finite-gain $\mathcal{L}_2$ stable.

The above theorem gives the stability and robustness conditions of the entire closed-loop flight testing system. Specifically, both subcomponents need to be δ-output strictly passive. It is easy to see that the closed-loop force/torque dynamics (3.9) is δ-output strictly passive since the Lyapunov function V can be chosen as $V = \frac{1}{2}F_s^2 + \frac{1}{2}\tau_s^{e2}$. For the vehicle subsystem, although we can not claim that every stable flight controller that minimizes the tracking error also makes the closed-loop dynamics δ-output strictly passive, this is often true for most types of flight control designs commonly seen, especially those using Lyapunov method. A simple analysis is presented below to justify this fact. Specifically, define the velocity tracking error variables

$$\begin{aligned} \dot{e}_{xv} &= \dot{x}_v - \dot{x}_{vd} \\ e_{\omega_v^v} &= \omega_v^v - \omega_{vd}^v. \end{aligned} \tag{3.17}$$

For a particular control law (3.10) that asymptotically stabilizes the velocity tracking error of the vehicle to the equilibrium $(0, 0)$ in the absence of uncertainties, there always exists a Lyapunov function $V(\dot{e}_{xv}, e_{\omega_v^v})$ such that $\dot{V} < \psi(\dot{e}_{xv}, e_{\omega_v^v})$, where $\psi(\dot{e}_{xv}, e_{\omega_v^v})$ is a positive definite function. Usually, both functions V and ψ contain quadratic terms of the velocity error variables. When the uncertainty terms F_s and τ_s^e are present, we take the time derivative of V, and it can be verified that $\dot{V}$ will be smaller than a

negative quadratic term of $\dot{e}_{xv}$ and $e_{\omega_v^v}$ in ψ, plus two additional terms $-\dot{e}_{xv}^T F_s$ and $-e_{\omega_v^v}^T \tau_s^e$ according to the vehicle dynamics (3.1). From Definition 1, the closed-loop vehicle dynamics from $(-F_s, -\tau_s^e)$ to $(\dot{e}_{xv}, e_{\omega_v^v})$ is δ-output strictly passive.

Safety Module One of the prominent features of our proposed flight testing system is the ability to ensure safety of the experiment. Due to the possible existence of strong aerodynamic uncertainties, flaws in control design, and incorrect setup or failure of the onboard electronics and communication, the vehicle may become unstable at any time during the initial flight testing. By mounting the vehicle on the end-effector of a humanoid robotic arm, we can confine the physical motion of the vehicle within a predefined safety region.

Specifically, let Ω_x and Ω_η be two closed sets in R^3 denoting the safety region for the position and attitude variables of the vehicle. To ensure $x_v \in \Omega_x$ and $\eta_v \in \Omega_\eta$ for all the time, we develop the following safety envelop algorithm:

$$\dot{x}_e = \begin{cases} 0 & \text{if } x_e \in \partial\Omega_x \text{ and } \dot{x}_{en}^T \gamma_x(x_e) > 0 \\ \dot{x}_{en} & \text{otherwise,} \end{cases}$$
$$\omega_e = \begin{cases} 0 & \text{if } \eta_e \in \partial\Omega_\eta \text{ and} \\ & (\Psi(\eta_e) R_0^e \omega_{en})^T \gamma_\eta(\eta_e) > 0 \ , \\ \omega_{en} & \text{otherwise,} \end{cases} \tag{3.18}$$

where $\dot{x}_{en}$ and ω_{en} are the regular control law synthesized in (3.8). $\gamma_x(x_e)$ and $\gamma_\eta(\eta_e)$ are vectors orthogonal to $\partial\Omega_x$ and $\partial\Omega_\eta$ and pointing outward. With the above safety algorithm, once the position or the attitude angles of the robot end-effector hit the boundary and the regular velocity command $\dot{x}_{en}$ or ω_{en} still contains an outward component relative to the boundary of the safety region, the motion of the end-effector will be set to still.

3.4 Experimental Results

In this section, we present experimental results to validate the proposed flight testing system with the dual-module coordinated control algorithm. Sawyer, a 7-DOF humanoid robotic manipulator by Rethink Robotics, is mounted to a heavy base. For illustration purpose, we develop a quadcopter which is structurally simple and easy to control, and use it as the UAV test subject of the platform. More advanced VTOL vehicles could also be designed and tested in this platform. The quadcopter is mounted to the end-effector of Sawyer through a 6-axis force/torque sensor by ATI. The robot arm control algorithm is implemented in a host computer running MATLAB. The host computer communicates with the onboard vehicle controller through XBee radio signal. The entire system is pictured in Figure 3.5.

Figure 3.5 The experimental platform of our flight testing system.

A couple of experiments are conducted on this platform to verify the ability of our proposed algorithm to maintain a minimum interaction force to achieve an emulated free flight environment while ensuring safety. First, we design a PID controller for the vehicle to let its z (up-down) coordinate track a filtered ramp command followed by a sinusoidal desired trajectory $0.1sin(\frac{1}{2}\pi t)$. Two different robot arm control algorithms are used for comparison:

(A) The damping control law (3.6) with the force feedback term alone, where $k_t = 0.035$ and $k_r = 6$.

(B) The proposed control law (3.8) with both the force feedback term and the desired feedforward compensation. The gains k_t and k_r are the same as (A).

The desired and actual positions as well as the interaction force measured by the force/torque sensor along z-axis for both (A) and (B) are plotted in Figure 3.6. As shown in the figure, for the damping control (A), both the z-axis tracking error of the vehicle and the interaction force between the vehicle and the end-effector are large. This is because the force error dynamics of (A) has $\dot{x}_v$ as the external uncertainty input. In comparison, our proposed algorithm (B) has a much smaller vehicle position tracking error and the interaction force (except for the first two seconds when the vehicle just starts to take off) due to the addition of the desired velocity compensation term. The residual force is within $0.7N$ and the position tracking error of the vehicle is almost not visible. This result shows that our algorithm is capable of maintaining a minimum level of interaction force between the vehicle and the robot end-effector during the flight testing, and ensuring a small tracking error of the vehicle if the vehicle controller itself is well designed.

Next, we perform a 6-DOF flight testing experiment on the platform using the proposed control strategy. A human operator uses an XBOX controller to control the movement of the vehicle in the 3D space. The two joysticks on the XBOX controller provide four input signals, which are specified as the desired z-axis (up-down) velocity, angular velocity about z-axis ($\dot{\psi}_v$), roll angle (ϕ_v), and pitch angle (θ_v), as shown in Figure 3.7. The tilting of the roll and pitch angles indirectly controls the movement of the vehicle along the x and y axes, which is the usual way commercial quadcopters are controlled. With such a control strategy, the vehicle can achieve 6-DOF motion in the 3D space. The position trajectory of the vehicle is shown in Figure 3.8, and the interaction force/torque wrench in 6 directions is plotted in Figure 3.9. The interaction

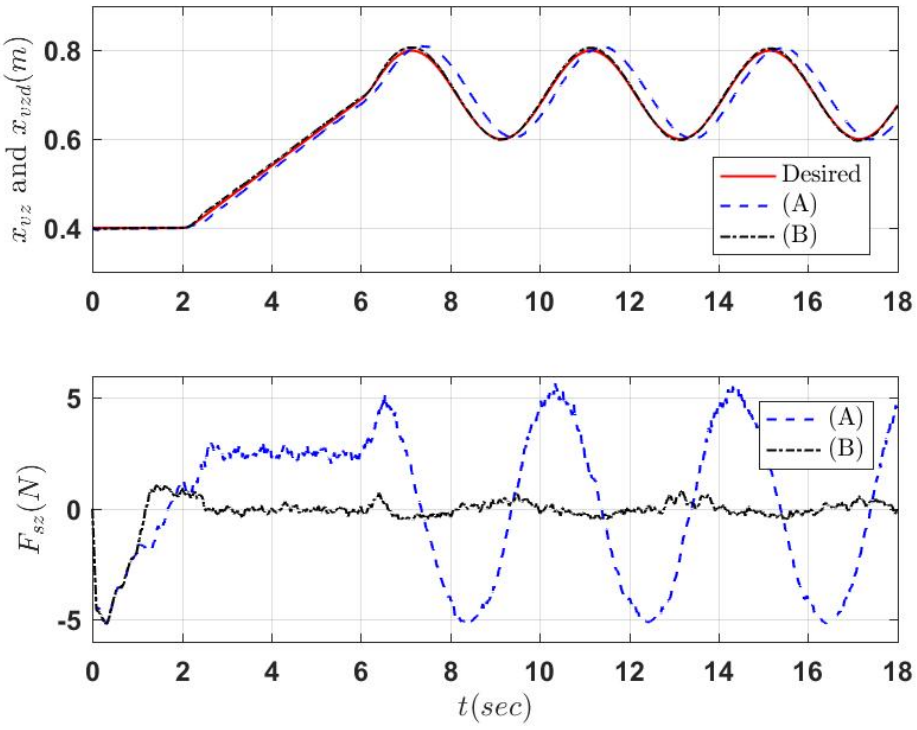

Figure 3.6 The positions and interaction forces along z-axis for (A) and (B).

force/torque wrench is very small, which is almost the same as the noise level of the force/torque sensor.

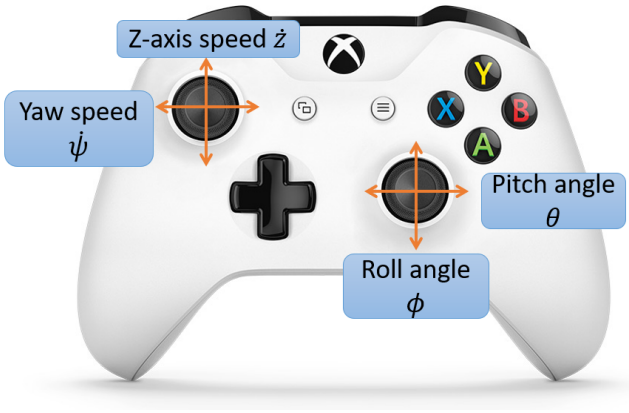

Figure 3.7 The Xbox controller used in the 6-DOF flight testing experiment.

Finally, we demonstrate the safety feature of our proposed algorithm by running another experiment. In the 6-DOF flight testing, the safety region is set to be as

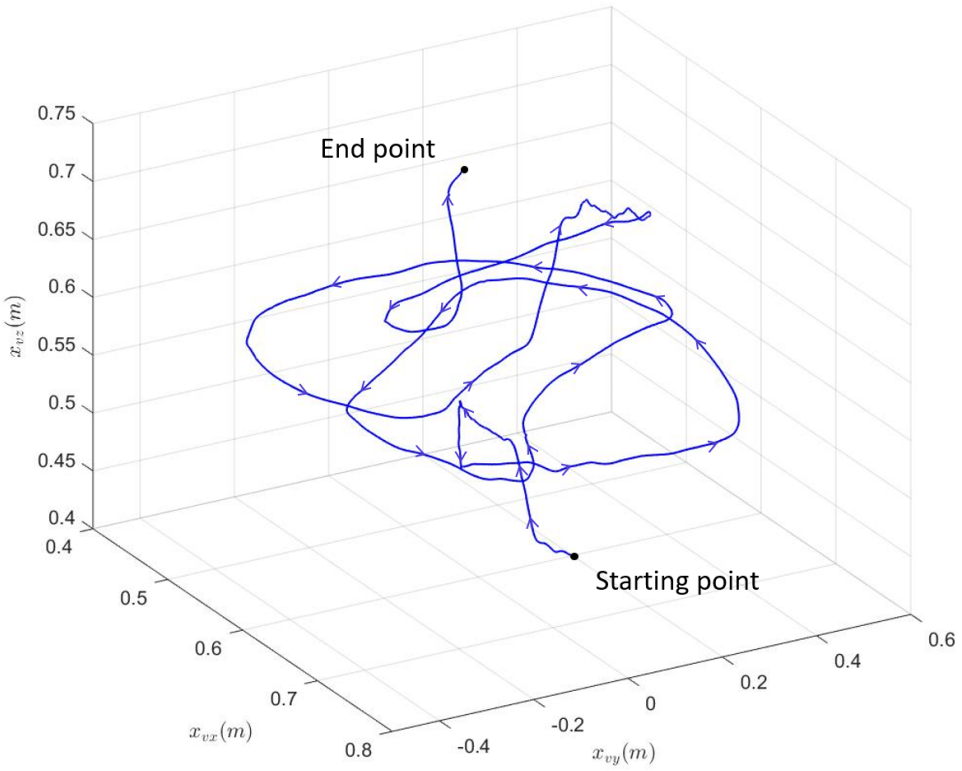

Figure 3.8 The trajectory of the vehicle in the 3D space for the 6-DOF flight testing experiment.

follows:

$$\begin{aligned}\Omega_x = \{x_v | x_{vx} \in [0.4, 0.85]m, x_{vy} \in [-0.6, 0.7]m,\\ x_{vz} \in [0.39, 1.05]m\}\\ \Omega_\eta = \{\eta_v | \phi_v \in [-0.05\pi, 0.05\pi]rad,\\ \theta_v \in [-0.05\pi, 0.05\pi]rad, \psi_v \in [-0.5\pi, 0.5\pi]rad\}.\end{aligned} \tag{3.19}$$

When the human operator tries to drive the vehicle out of the region, or the vehicle becomes unstable due to unexpected reasons, the safety algorithm will be activated. The motion of the robot will be stopped to ensure safety. Now, we let the vehicle hover at the initial position for two seconds, and then make the RPM commands sent to the two motors on one side half of their desired values, so as to mimic the sudden failure or malfunction of the vehicle drive system. The x, y, z positions and the roll,

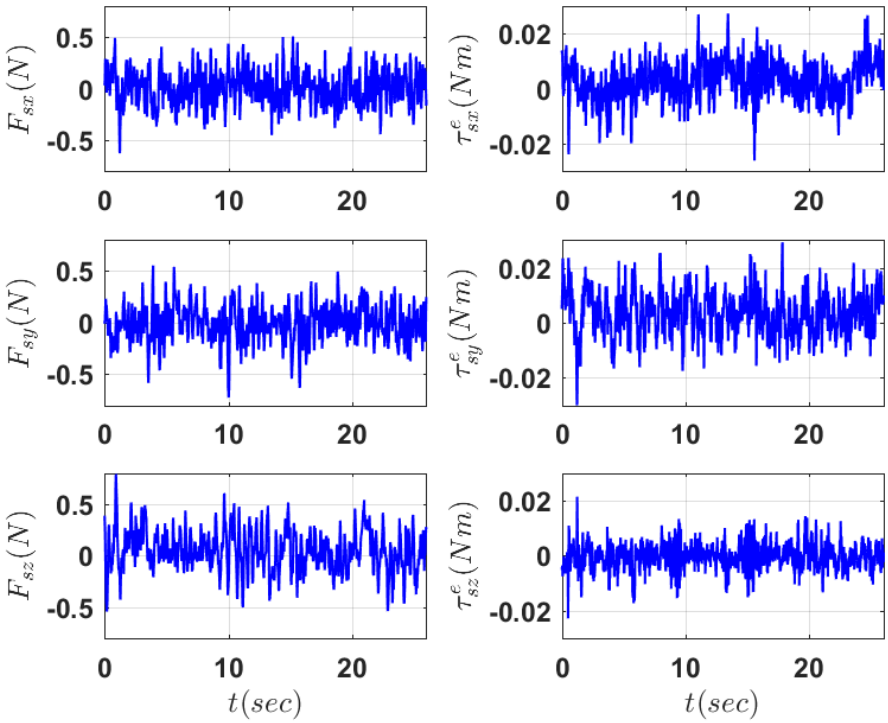

Figure 3.9 The 6-axis force/torque for the 6-DOF flight testing experiment.

pitch, yaw angles are plotted in Figure 3.10. When the safety algorithm detects that the y coordinate of the vehicle exceeds $0.7m$, it stops the motion of the robot and shuts down the motors of the vehicle.

All the three experiments have been recorded and the video can be found online at the link below:

https://youtu.be/L3608cB04Vw.

3.5 Conclusions

In this research, we developed a novel 6-DOF automated flight testing strategy for VTOL UAVs by mounting the vehicle to the end-effector of an articulated humanoid robot arm through a 6-axis force/torque sensor. During the flight testing process, a dual-module control law was executed. In the regular control module, a damping force control with feedforward compensation was implemented to minimize the interaction

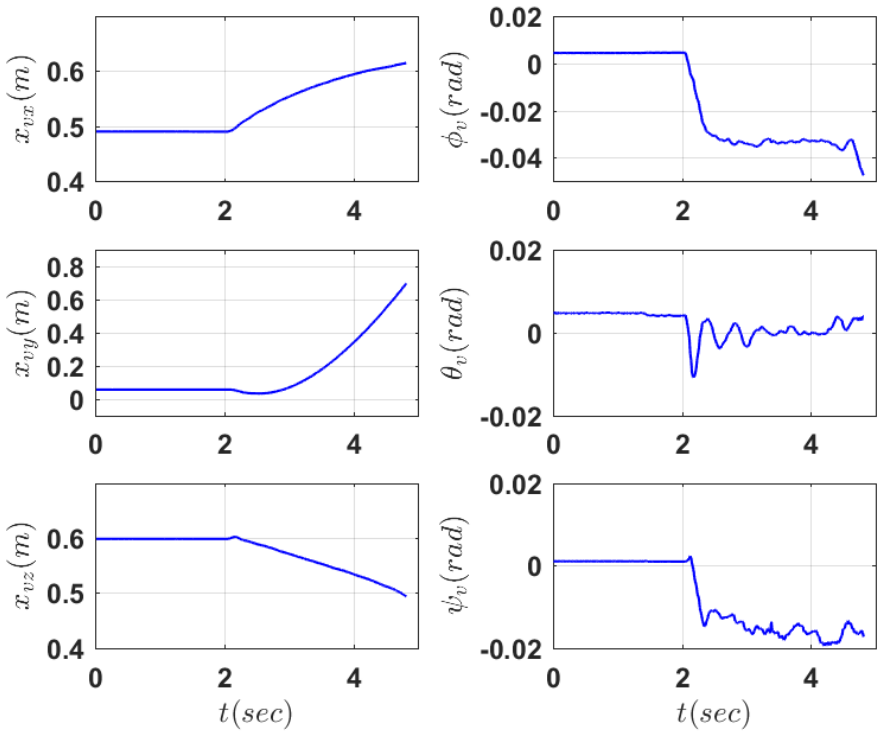

Figure 3.10 The 6-axis positions and attitude angles of the vehicle during the experiment in which two motors are assumed to be malfunctioned after 2 seconds.

force between the vehicle and the robot end-effector regardless of the constantly-changing motion of the vehicle. In the safety module, a safety algorithm was activated to constrain the range of the motion of the vehicle in case of emergency. The proposed strategy was verified to be capable of emulating a realistic free flight environment while ensuring safety through both theoretical justification and experimental validation, making it an ideal choice for initial flight testings.

CHAPTER 4

A TILTING-ROTOR UNMANNED AERIAL VEHICLE FOR ENHANCED AERIAL LOCOMOTION AND MANIPULATION CAPABILITIES: DESIGN, CONTROL, AND APPLICATIONS

4.1 Introduction

The past decade has seen a dramatic growth of research efforts on multirotor Unmanned Aerial Vehicles(UAVs), both for civilian and military applications such as remote surveillance, photography, inspection, search and rescue operations [44, 45, 46]. Nevertheless, the study of new designs and controls of multirotor UAVs never stops, as more and more frontier applications require the vehicles to actively interact with external environments, instead of just being the under-actuated passive sensing platforms. Due to the complexity and possibly unstructured nature of external environments, tasks such as navigation in clustered and tight spaces [47], manipulation of objects in the environment [48, 49], and interaction/collaboration with humans [50] (as illustrated in Figure 4.1) require superior locomotion and manipulation capabilities from UAVs. Such stringent requirements demand that the next generation of multirotors should possess improved mobility, stability, motion accuracy and energy efficiency compared to traditional ones.

Figure 4.1 Application scenarios in which aerial locomotion in constrained and clustered spaces or fine aerial manipulation is required. From left to right: underground exploration, aerial power maintenance, pipeline system inspection and repair.

Standard coplanar multirotor UAVs such as quadcopters have been well developed in terms of mechatronic design and motion control, which makes them stable platforms for conventional aerial locomotion and sensing tasks. The rotors of these multirotor UAVs are fixed to the body frame and aligned in a same plane, with all the thrust vectors pointing along a single direction for most of the vehicles. This kind of design avoids complex mechanical control linkage, and thus can achieve a more stable, more robust, and safer flight compared to traditional vertical-take-off-and-landing (VTOL) helicopters [51, 52]. However, the mobility and controllability of these coplanar multirotor vehicles are limited due to their inherent underactuation nature, i.e., if the vehicle needs to move forward, it has to rotate its body to generate a forward thrust. As a result, the dynamics of rotational and translational motions are coupled, making these standard UAVs incapable of tracking arbitrary position and orientation trajectories [1], and in addition, not able to generate arbitrary force and torque wrench. Thus, these UAVs may run into problems when the specific application demands a change of the hovering attitude or generation of force and torque wrench in a particular direction while maintaining motion accuracy, good stability, and energy efficiency [53]. These applications may include obstacle avoidance in clustered environments, and object manipulation such as opening a valve on the wall.

From the above analyses on the pros and cons of existing UAV structures, it is clear that the next generation of multirotor UAVs needs to have the following important characteristics in order to meet the challenging goals of enhanced aerial locomotion and manipulation in unstructured environments:

1. More motion DOFs than traditional UAVs, which is characterized by the ability of the vehicle to change one or two of its attitude angles independently from the translational motions.
2. Simple mechanical structure, which is to avoid stability, robustness, and high weight issues arising from over-complicated designs.

3. Avoidance of thrust force cancellation (through both the design and control) to achieve high power efficiency.
4. High motion control precision and the ability to adapt to changing parameters during locomotion and manipulation in unknown environments.

In this chapter, we propose the design and control of a novel multirotor UAV that is capable of achieving the above-mentioned capabilities for enhanced aerial locomotion and manipulation performances. The vehicle has a tilting-rotor architecture. Specifically, two independently-controlled tilting arms are placed at both sides of the vehicle in an "H" configuration. With such a design, the vehicle has one more DOF of motion than the traditional quadcopters, allowing it to have independent roll angle regulation at the expense of only two additional servo motors with minimum transmission needed. Based on the dynamics of the proposed UAV design, a dual-level adaptive robust control (ARC) method is formulated to cope with parametric uncertainties and uncertain nonlinearities that may occur during aerial maneuvering and manipulation. Additionally, a thrust force optimization problem minimizing power consumption while achieving the desired body force wrench is solved precisely and efficiently to resolve the redundancy in actuation. For potential applications of the proposed novel UAV design with control, we conduct four challenging experiments to show the advantage of our innovation in real aerial locomotion and manipulation tasks: circular trajectory tracking, passing through a narrow tunnel, picking up an object from a cluttered shelf, and aerial hole drilling.

4.2 System Architecture and Mechanical Design

As discussed in the previous section, a tilting-rotor structure is necessary for the vehicle to avoid ineffective thrust force cancellation while achieving decoupled rotational and translational motions. The fully-actuated (6-DOF) design and the 5-DOF actuation design can both achieve higher DOFs than traditional quadcopters. It is noted, however, that the fully-actuated version requires each rotor to be tiltable around at

least two axes to make full use of the thrust forces while avoiding ineffective thrust force cancellation. This makes the design extremely complicated with very high weight introduced by a large number of servos. The 5-DOF version, although not fully actuated, can provide an independent roll angle regulation decoupled from the translational motion control, which is sufficient for most applications as the vehicle can fly almost "vertically" with this design.

Existing 5-DOF designs published in recent years used either one single servo to control the tilt angles of all four rotors [54], or four servos to independently control the tilt angle of each rotor [55]. The former requires a complicated transmission system which may introduce extra backlash and uncertainties, while the latter weights much higher and may have motion accuracy issue caused by the slight difference of the four servo angles of the four rotors. In view of this, we propose a novel tilting-rotor architecture which uses two servo motors. Specifically, two pairs of rotors are mounted on two independently-controlled rotating arms placed at both sides of the vehicle in an "H" configuration, as shown in Figure 4.2. In other words, each arm is tilted by a single servo motor, and carries two rotors attached to its two ends. Hence, the direction of thrust forces generated by the two rotors on each arm can be simultaneously switched, eliminating any possible tilt angle mismatches for each pair of rotors on the same arm. Furthermore, only two additional servos are needed compared to traditional quadcopters, leading to a less total weight and smaller probability of fault occurrence than designs with too many servos. In the mechanical design, we 3D print two "Ω"-shaped connectors, one for each arm, to link the tilting motions of the two rotors together, which avoids additional backlash and flexibility issue in a complicated transmission system. A prototype of this UAV made in the Assistive and Intelligent Robotics Laboratory at the Mechanical & Industrial Engineering Department at NJIT is shown in Figure 4.3.

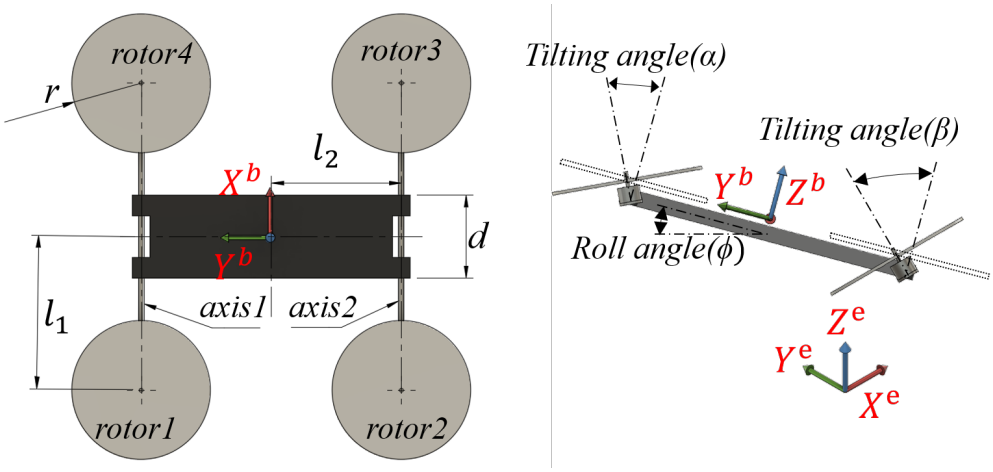

Figure 4.2 Top view and front view of the proposed tilting multirotor UAV. Tilting angles α and β are the rotating angles about axis1 and axis2 of the two arms respectively. The zero-angle position (shown in dash lines) of each arm is where the rotor's rotation plane is parallel to the main body.

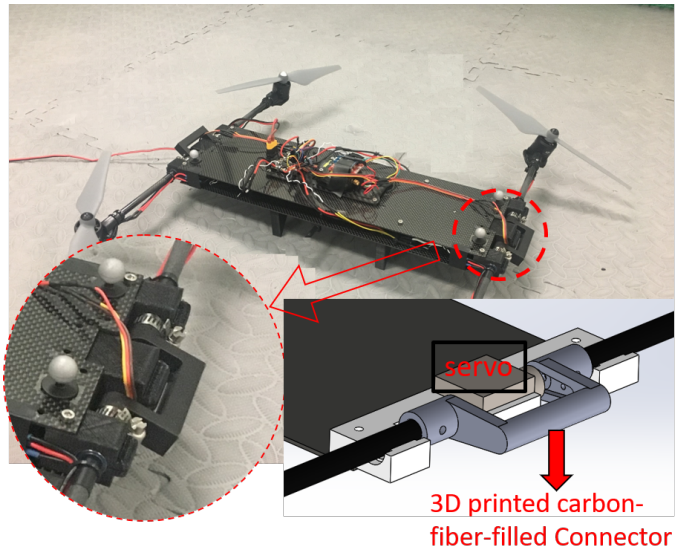

Figure 4.3 A prototype of the proposed multirotor UAV, and the detailed view of one of its tilting-rotor arms.

4.3 System Modeling

4.3.1 Coordinate systems

To develop the dynamic model of the UAV, we consider the following right-hand coordinate systems as shown in Figure 4.2.

$\{e\}$: The earth (inertial) frame with axes $X^e; Y^e; Z^e$.

$\{b\}$: The body-fixed frame with axes $X^b; Y^b; Z^b$.

For convenience of mathematical derivation, the $X^b - Y^b$ plane is defined to be parallel to the plane formed by the two tilting axes, and X^b is parallel to the two tilting axes, as shown in Figure 4.2 (right).

The rotational matrix [7] between the defined coordinate systems is denoted by:

R_b^e: the rotational matrix from frame $\{e\}$ to frame $\{b\}$.

$$R_b^e = \begin{bmatrix} C_\theta C_\psi & S_\theta C_\psi S_\phi - S_\psi C_\phi & S_\theta C_\psi C_\phi + S_\psi S_\phi \\ C_\theta S_\psi & S_\theta S_\psi S_\phi + C_\psi C_\phi & S_\theta S_\psi C_\phi - C_\psi S_\phi \\ -S_\theta & C_\theta S_\phi & C_\theta C_\phi \end{bmatrix},$$

where ϕ, θ, and ψ are the Euler angles (roll, pitch, yaw angles) of the UAV body, and "C" and "S" are shorthand notations for cos and sin, respectively.

4.3.2 Forces and torques

The total force The total force acting on the UAV and expressed in the body coordinate system is described as :

$$F^b = [F_x^b, F_y^b, F_z^b]^T = F_p^b + F_g^b + F_\Delta^b, \tag{4.1}$$

where $F_p^b = \sum_{i=1}^{4} F_{p_i}^b$ is the total thrust force which equals to the sum of all individual thrust forces expressed in body frame $\{b\}$. $F_g^b = mR_b^{eT}G$ is the gravitational force expressed in the body frame, m is the total mass of the UAV, $G = [0, 0, -g]^T$ is the gravitational acceleration vector in inertia frame. $F_\Delta^b \in R^3$ is the force uncertainty term represented in body frame. $F_\Delta^b \in R^3$ and the torque uncertainty τ_Δ^b to appear in (4.3) may incorporate unmodeled aerodynamic effects, imbalances caused by batteries and/or on-board sensors, motion of a robotic arm placed for aerial manipulations, interactions with the environment, wind and so on.

It is noted that since the propeller cannot turn around Y^b, the projection of the thrust force onto X^b is equal to zero, i.e., $F_p^b = [0, F_{py}^b, F_{pz}^b]^T$. Defining F_1, F_2, F_3, F_4 as the absolute values of the thrust forces of the four propellers and α, β as the front and rear tilting angles, as shown in Figure 4.2, the F_{py}^b and F_{pz}^b can be expressed as:

$$\begin{aligned} F_{py}^b &= (F_1 + F_4)S_\alpha + (F_2 + F_3)S_\beta, \\ F_{pz}^b &= (F_1 + F_4)C_\alpha + (F_2 + F_3)C_\beta. \end{aligned} \tag{4.2}$$

The total torque The total torque acting on the UAV and expressed in the body frame is

$$\tau^b = [\tau_x^b, \tau_y^b, \tau_z^b]^T = \tau_p^b + \tau_\Delta^b, \tag{4.3}$$

where $\tau_p^b = \sum_{i=1}^{4} r_i^b \times F_{p_i}^b + \sum_{i=1}^{4} D_i k F_{p_i}^b$ is the total torque generated by the propellers, including the thrust torque $\sum_{i=1}^{4} r_i^b \times F_{p_i}^b$ and drag torque $\sum_{i=1}^{4} D_i k F_{p_i}^b$, in which r_i^b is the coordinate vector of the center of the *i-th* propeller in body frame, k is a constant ratio of drag torque to thrust force, and D_i is a constant equal to 1 when the *i-th* propeller rotates in clockwise direction, and -1 when it rotates in counterclockwise direction. $\tau_\Delta^b \in R^3$ is the torque uncertainty term represented in body frame.

Defining l_1 as the half distance between the two rotors on each tilting axis, l_2 as the half distance between the two tilting axes, the x, y, z components of τ_p^b can be expressed as

$$\begin{aligned} \tau_{px}^b &= (F_1 + F_4)l_2 C_\alpha - (F_2 + F_3)l_2 C_\beta, \\ \tau_{py}^b &= (F_1 - F_4)(C_\alpha l_1 + S_\alpha k) + (F_2 - F_3)(C_\beta l_1 - S_\beta k), \\ \tau_{pz}^b &= (F_4 - F_1)(S_\alpha l_1 - C_\alpha k) + (F_3 - F_2)(S_\beta l_1 + C_\beta k). \end{aligned} \tag{4.4}$$

4.3.3 Dynamic model

The total force and torque applied to the vehicle are related to the vehicle's motion through the following dynamic equations:

1) Translational motion:

$$F^b = F_p^b + F_g^b + F_\Delta^b = m \cdot (\dot{v}^b + \omega^b \times v^b), \tag{4.5}$$

where $v^b = [v_x^b, v_y^b, v_z^b]^T$ and $\omega^b = [\omega_x^b, \omega_y^b, \omega_z^b]^T$ are the vehicle's translational and rotational velocities respectively expressed in body frame.

2) Rotational motion:

$$\tau^b = \tau_p^b + \tau_\Delta^b = I^b \dot{\omega}^b + (I^b \omega^b) \times \omega^b, \tag{4.6}$$

where $I^b \in R^{3\times3}$ is the body frame inertial tensor matrix of the vehicle.

In this chapter, we assume that the center of mass of the vehicle is close enough to body frame center, while the discrepancy during the aerial manipulation process when payload changes are lumped to the uncertainty term F_Δ^b. The reason we make this assumption is because explicitly considering the effect of unknown center of mass shift on the body frame acceleration for such an underactuated vehicle will make the dynamic system in a non-strict feedback form, whose internal state stability is hard to guarantee without making very restrictive assumptions and sacrificing the tracking performance [56]. Up to now, there has been no rigorous study on stabilizing an underactuated UAV with unknown center of mass location (works such as [57, 58, 59] have been shown to be flawed as the control laws were simply designed in 6 dimensions with the underactuation constraint ignored [60]). In fact, as long as the unknown center of mass displacement is not too significant, it can be effectively dealt with by the guaranteed robustness of the controller, as can be seen from the experimental results to be shown later as well as many commercially successful quadcopters that add and drop payload frequently.

4.3.4 Kinematic relationship

Let $\lambda = [x, y, z]^T$ be the vehicle's position (the coordinate of the origin of the body frame $\{b\}$) expressed in inertia frame $\{e\}$, $\eta = [\phi, \theta, \psi]^T$ be the attitude vector of the vehicle. The kinematic relationship between the position/attitude of the vehicle and the body frame velocities is given by the following two equations:

$$\dot{\lambda} = R_b^e v^b, \quad \dot{\eta} = \Psi \omega^b, \tag{4.7}$$

where $\Psi = \begin{bmatrix} 1 & S_\phi T_\theta & C_\phi T_\theta \\ 0 & C_\phi & -S_\phi \\ 0 & \frac{S_\phi}{C_\theta} & \frac{C_\phi}{C_\theta} \end{bmatrix}$ is the transformation matrix at kinematic level.

4.4 Control Design

Defining $\chi = [x, y, z, \phi, \psi]^T$ as the vector of vehicle states to be controlled, which consists of the vehicle's position, and the roll, yaw angles, the control objective is to synthesize a control input $U = [F_1, F_2, F_3, F_4, \alpha, \beta]^T$ including four rotors' thrust forces and two tilting angles, such that $\chi(t)$ tracks its desired trajectory $\chi_d(t)$ as accurately as possible despite the presence of uncertain nonlinearities F_Δ^b, τ_Δ^b as well as the unknown inertia parameters m, I_{xx}, I_{yy}, I_{zz}, I_{xy}, I_{yz}, I_{xz}. We develop the following two-stage control strategy:

- Stage 1. Dual-level adaptive robust tracking control
  Defining $B = [F_{py}^b, F_{pz}^b, \tau_{px}^b, \tau_{py}^b, \tau_{pz}^b]^T$ as the 5-DOF body force wrench input to the system, we develop a novel dual-level adaptive robust control (ARC) structure to achieve trajectory tracking.

- Stage 2. Constrained optimization for redundancy resolution
  At the second stage, the actual input U consisting of two tiling angles as well as four thrust forces are calculated based on the desired 5-DOF body force wrench B. To solve the actuation redundancy issue, a thrust force optimization problem minimizing power consumption while achieving the desired body force wrench will be formulated and solved efficiently online.

4.4.1 Dual-level adaptive robust control design

A closer look at the system dynamics leads to an interesting discovery: although the input variables F_{py}^b and F_{pz}^b can directly affect the translational acceleration of the vehicle, they lack one DOF to fully stabilize the vehicle's 3D position (x, y, z). With the given desired trajectory of the roll angle ϕ and yaw angle ψ, the vehicle has to utilize the extra pitch angle θ to indirectly compensate for the lack of F_{px}^b in the translational dynamics. Thus, the highest relative order from the input variables to the output variables is equal to 4.

For this high-order cascaded system with parameter uncertainties, instead of using backstepping ARC [61] which is theoretically complicated and non-intuitive for gain tuning in real implementations, we propose a dual-level ARC which decouples the control of attitude angles and the control of linear position variables:

- *Low-level attitude tracking controller:*
  A low-level attitude controller is first designed using ARC to achieve accurate tracking for the roll, pitch, and yaw angles with respect to their desired trajectories.
- *High-level position tracking controller:*
  A high-level position controller is then designed to generate the virtual (ideal) translational force vector in inertia frame using another ARC, such that the vehicle's position tracks its desired trajectory as accurately as possible.
- *Connection between high-level and low-level controllers:*
  In the final step, the actual body force inputs F_{py}^b, F_{pz}^b and the desired low-level pitch angle trajectory are generated from the virtual control law obtained from high-level position controller.

Similar two-level architectures have already been used for robot and quadcopter control [62, 63, 64]. However, the dual-level ARC we develop here is the first one to be applied to this unique UAV with 5-DOF actuation and 6-DOF motion. In addition, the effect of low-level tracking error on the high-level control performance is explicitly taken care of in the design, making the algorithm more theoretically rigorous than the previous two-level control methods.

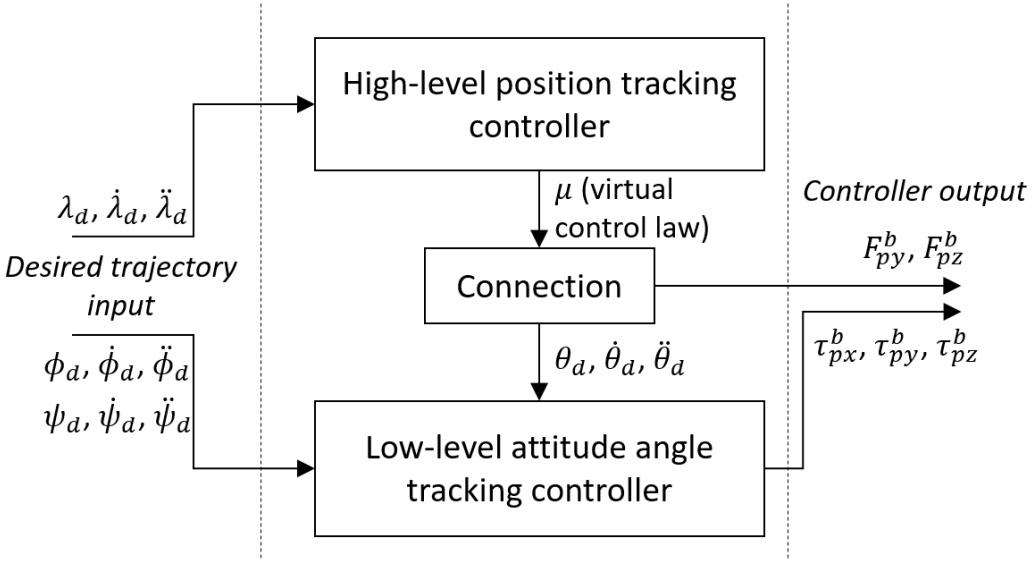

Figure 4.4 Schematic diagram of the proposed dual-level ARC design.

To begin with, let us define the uncertainty variables as:

$$\begin{aligned} \Theta_L &= [I_{xx}, I_{yy}, I_{zz}, I_{xy}, I_{yz}, I_{xz}, d^b_{\tau x}, d^b_{\tau y}, d^b_{\tau z}]^T, \\ \Theta_H &= [\tfrac{1}{m}, \tfrac{d^b_{Fx}}{m}, \tfrac{d^b_{Fy}}{m}, \tfrac{d^b_{Fz}}{m}]^T, \\ \tilde{F}^b_\Delta &= F^b_\Delta - d^b_F, \quad \tilde{\tau}^b_\Delta = \tau^b_\Delta - d^b_\tau, \end{aligned} \tag{4.8}$$

where Θ_L and Θ_H are the vectors of low-level and high-level unknown parameters, respectively. d^b_{Fx}, d^b_{Fy}, d^b_{Fz}, $d^b_{\tau x}$, $d^b_{\tau y}$, $d^b_{\tau z}$ are constant portions of the uncertainty terms F^b_Δ and τ^b_Δ. $\tilde{F}^b_\Delta$ and $\tilde{\tau}^b_\Delta$ are time-varying portions of the uncertainties. The following practical assumption is made on the uncertainties [30]:

The extent of the parametric uncertainties and uncertain nonlinearities are known, i.e.,

$$\begin{aligned} \Theta_L \in \Omega_{\Theta_L} &\triangleq \{\Theta_L : \Theta_{Lmin} \le \Theta_L \le \Theta_{Lmax}\}, \\ \Theta_H \in \Omega_{\Theta_H} &\triangleq \{\Theta_H : \Theta_{Hmin} \le \Theta_L \le \Theta_{Hmax}\}, \\ \tilde{F}^b_\Delta \in \Omega_{\tilde{F}^b_\Delta} &\triangleq \{\tilde{F}^b_\Delta : |\tilde{F}^b_\Delta| \le \delta_F\}, \\ \tilde{\tau}^b_\Delta \in \Omega_{\tilde{\tau}^b_\Delta} &\triangleq \{\tilde{\tau}^b_\Delta : |\tilde{\tau}^b_\Delta| \le \delta_\tau\}, \end{aligned} \tag{4.9}$$

where $\Theta_{Lmin} = [\Theta_{L1min}, \cdots, \Theta_{L9min}]^T$, $\Theta_{Lmax} = [$
$\Theta_{L1max}, \cdots, \Theta_{L9max}]^T$, $\Theta_{Hmin} = [\Theta_{H1min}, \cdots, \Theta_{H4min}$
$]^T$, $\Theta_{Hmax} = [\Theta_{H1max}, \cdots, \Theta_{H4max}]^T$, δ_F, and δ_τ are the known upper and lower bounds of the uncertainties.

Let $\hat{\Theta}_L$, $\hat{\Theta}_H$ denote the estimate of Θ_L, Θ_H and $\tilde{\Theta}_L$, $\tilde{\Theta}_H$ the estimation errors (i.e., $\tilde{\Theta}_L = \hat{\Theta}_L - \Theta_L$, $\tilde{\Theta}_H = \hat{\Theta}_H - \Theta_H$). The following adaptation law with discontinuous projection modification is used:

$$\dot{\hat{\Theta}}_L = Proj_{\hat{\Theta}_L}(\Gamma_L \sigma_L), \quad \dot{\hat{\Theta}}_H = Proj_{\hat{\Theta}_H}(\Gamma_H \sigma_H), \tag{4.10}$$

where Γ_L, $\Gamma_H > 0$ are diagonal matrices of adaptation gains, σ_L, σ_H are adaptation functions to be synthesized later. The projection mapping $Proj_{\hat{*}}(\bullet) = [\cdots, Proj_{\hat{*}_i}(\bullet_i), \cdots]^T$ is defined as

$$Proj_{\hat{*}_i}(\bullet_i) = \begin{cases} 0, & \text{if } \hat{*}_i = *_{imax} \text{ and } \bullet_i > 0, \\ 0, & \text{if } \hat{*}_i = *_{imin} \text{ and } \bullet_i < 0, \\ \bullet_i, & \text{otherwise.} \end{cases} \tag{4.11}$$

It can be shown that for any adaptation functions σ_L and σ_H, the projection mappings used in (4.11) guarantee

$$\begin{aligned} &\textbf{P1} \qquad \hat{\Theta}_L \in \Omega_{\Theta_L}, \quad \hat{\Theta}_H \in \Omega_{\Theta_H}, \\ &\textbf{P2} \qquad \tilde{\Theta}_L^T(\Gamma_L^{-1} Proj_{\hat{\Theta}_L}(\Gamma_L \sigma_L) - \sigma_L) \le 0, \\ &\qquad\quad \tilde{\Theta}_H^T(\Gamma_H^{-1} Proj_{\hat{\Theta}_H}(\Gamma_H \sigma_H) - \sigma_H) \le 0. \end{aligned} \tag{4.12}$$

Low-level attitude tracking controller Let $\eta_d(t) = [\phi_d(t), \theta_d(t), \psi_d(t)]^T$ be the desired attitude angle trajectory, and $e_\eta = \eta - \eta_d$ be the attitude tracking error. We define the following switching-function-like quantity for the attitude tracking error as

$$s_\eta = \Psi^{-1}(\dot{e}_\eta + k_{\eta 1} e_\eta) = \omega^b - \Psi^{-1}\dot{\eta}_d + \Psi^{-1} k_{\eta 1} e_\eta, \tag{4.13}$$

where $k_{\eta 1} > 0$ is a diagonal gain matrix. Clearly, if s_η is small or converges to zero exponentially, then the attitude tracking error e_η will be small or converge to zero exponentially. So the rest of the design is to make $s_\eta \to 0$. Differentiating (4.13) and using (4.6):

$$\begin{aligned} I^b \dot{s}_\eta &= I^b \dot{\omega}^b - I^b [\dot{\Psi}^{-1} \dot{\eta}_d + \Psi^{-1} \ddot{\eta}_d - \dot{\Psi}^{-1} k_{\eta 1} e_\eta \\ &\quad - \Psi^{-1} k_{\eta 1} (\Psi \omega^b - \dot{\eta}_d)] \\ &= \tau_p^b + N_\eta(\eta, \omega^b, e_\eta, \eta_d, \dot{\eta}_d, \ddot{\eta}_d)\Theta_L + \tilde{\tau}_\Delta^b, \end{aligned} \tag{4.14}$$

where N_η is the regressor matrix depending upon the system states, tracking error, and desired trajectory.

The following ARC control law is proposed:

$$\tau_p^b = \tau_{ps}^b + \tau_{pa}^b, \quad \tau_{pa}^b = -N_\eta(\eta, \omega^b, e_\eta, \eta_d, \dot{\eta}_d, \ddot{\eta}_d)\hat{\Theta}_L, \tag{4.15}$$

where τ_{pa}^b is the adjustable model compensation term, τ_{ps}^b is the robust feedback term synthesized as

$$\tau_{ps}^b = \tau_{ps1}^b + \tau_{ps2}^b, \quad \tau_{ps1}^b = -k_{\eta 2} s_\eta, \tag{4.16}$$

where τ_{ps1}^b is a proportional feedback term with $k_{\eta 2} > 0$ being the diagonal gain matrix. τ_{ps2}^b is a robust feedback to attenuate the effect of nonlinear model uncertainties caused by parameter estimation error, which satisfies the following two conditions:

$$\begin{aligned} &1. \quad s_\eta^T(\tau_{ps2}^b - N_\eta \tilde{\Theta}_L + \tilde{\tau}_\Delta^b) \le \epsilon_\eta, \\ &2. \quad s_\eta^T \tau_{ps2}^b \le 0, \end{aligned} \tag{4.17}$$

where ϵ_η is a design parameter which can be arbitrarily small and τ_{ps2} can be found in the following way [30]. Let h_η be any smooth function satisfying $h_\eta \ge \|\Theta_{LM}\|\|N_\eta\| + \delta_\tau$, where $\Theta_{LM} = \Theta_{Lmax} - \Theta_{Lmin}$. Then, τ_{ps2}^b can be chosen as

$$\tau_{ps2}^b = -\frac{1}{4\epsilon_\eta} h_\eta^2 s_\eta. \tag{4.18}$$

If the control law (4.15) is used, with the adaptation function in (4.10) chosen as $\sigma_L = N_\eta^T s_\eta$, then the following results are guaranteed:

1) In general, all signals are bounded. Furthermore, the positive definite function V_η defined by $V_\eta = \frac{1}{2} s_\eta^T I^b s_\eta$ is bounded above by $V_\eta \leq exp(-\varepsilon_\eta t) V_\eta(0) + \frac{\epsilon_\eta}{\varepsilon_\eta}[1 - exp(-\varepsilon_\eta t)]$, where $\varepsilon_\eta = 2k_{\eta 2min}/\lambda_{max}(I^b)$, $k_{\eta 2min}$ is the minimum value of all the entries in $k_{\eta 2}$, $\lambda_{max}(I^b)$ is the maximum eigenvalue of matrix I^b .

2) If after a finite time t_0, there exist parametric uncertainties only(i.e., $\tilde{\tau}_\Delta^b = 0, \forall t \geq t_0$), then, in addition to results in 1), zero final tracking error is also achieved, i.e., $e_\eta \to 0$ and $s_\eta \to 0$ as $t \to \infty$.

The proof of the above theorem can be worked out in a similar way as in [30]. From part 1) of the above theorem, it is clear that at steady state, the attitude tracking error e_η is upper bounded in magnitude. Let us denote the infinity norm of e_η (the maximum absolute value among its three elements) at steady state as δ_η, i.e., $|e_\eta|_\infty \leq \delta_\eta$. It is easy to see that the bound δ_η can be set arbitrarily small by increasing the gains $k_{\eta 1}$ and $k_{\eta 2}$. Later on, the attitude tracking error e_η will be explicitly considered and suppressed in the high-level position controller with the known bound δ_η.

High-level position tracking controller Let $\lambda_d(t) = [x_d(t), y_d(t), z_d(t)]^T$ be the desired position trajectory in inertia frame, and $e_\lambda = \lambda - \lambda_d$ be the position tracking error. We define the following switching-function-like quantity for the position tracking error as

$$s_\lambda = (\dot{e}_\lambda + k_{\lambda 1} e_\lambda) = R_b^e v^b - \dot{\lambda}_d + k_{\lambda 1} e_\lambda, \tag{4.19}$$

where $k_{\lambda 1} > 0$ is a diagonal gain matrix. Then according to (4.5), the dynamics of s_λ is

$$\begin{aligned} \dot{s}_\lambda &= \dot{R}_b^e v^b + R_b^e \dot{v}^b - \ddot{\lambda}_d + k_{\lambda 1}\dot{e}_\lambda \\ &= \Theta_{H1} F_p^e + G - \ddot{\lambda}_d + k_{\lambda 1}\dot{e}_\lambda + R_b^e[\Theta_{H2}, \Theta_{H3}, \Theta_{H4}]^T \\ &\quad + R_b^e \tilde{F}_\Delta^b, \end{aligned} \tag{4.20}$$

where $F_p^e = R_b^e F_p^b$ is the vector of thrust forces projected to the X^e, Y^e, Z^e axes in inertia frame, known as the "translational force vector".

Let $F_{pd}^e = R_b^e(\eta_d) F_p^b$ denote the "desired" translational force vector, in which the actual attitude angles are replaced by the desired ones. Then, $F_p^e = \tilde{R}_b^e F_{pd}^b$, where $\tilde{R}_b^e = R_b^e R_b^e(\eta_d)^T$ is the error on the rotation matrix caused by low-level controller. It is noted that by choosing the low-level attitude control gains to be high enough, the error matrix $\tilde{R}_b^e$ can be made arbitrarily close to identity matrix $I_{3\times 3}$. Substituting F_p^e with $\tilde{R}_b^e F_{pd}^b$, the dynamics of s_λ is represented by

$$\begin{aligned} \dot{s}_\lambda &= \Theta_{H1} \tilde{R}_b^e F_{pd}^b + G - \ddot{\lambda}_d + k_{\lambda 1}\dot{e}_\lambda \\ &\quad + R_b^e[\Theta_{H2}, \Theta_{H3}, \Theta_{H4}]^T + R_b^e \tilde{F}_\Delta^b. \end{aligned} \tag{4.21}$$

The desired virtual control input law for F_{pd}^e is designed as follows:

$$\begin{aligned} \mu &= \mu_s + \mu_a, \\ \mu_a &= -\tfrac{1}{\hat{\Theta}_{H1}}(G - \ddot{\lambda}_d + k_{\lambda 1}\dot{e}_\lambda + R_b^e[\hat{\Theta}_{H2}, \hat{\Theta}_{H3}, \hat{\Theta}_{H4}]^T), \end{aligned} \tag{4.22}$$

where μ_a is the model compensation term, μ_s is the robust feedback term synthesized as

$$\mu_s = \mu_{s1} + \mu_{s2}, \quad \mu_{s1} = -\frac{k_{\lambda 2}}{\Theta_{H1min}} s_\lambda, \tag{4.23}$$

where $k_{\lambda 2} > 0$ is a constant gain matrix, μ_{s2} is a robust feedback to attenuate the effect of nonlinear model uncertainties caused by parameter estimation error, which

satisfies the following two conditions:

$$\begin{aligned} &1. \quad s_\lambda^T[\Theta_{H1}\tilde{R}_b^e\mu_{s2} - (I_{3\times3} - \tilde{R}_b^e)N_\lambda\hat{\Theta}_H - N_\lambda\tilde{\Theta}_H + R_b^e\tilde{F}_\Delta^b] \\ &\quad \leq \epsilon_\lambda, \\ &2. \quad s_\lambda^T\tilde{R}_b^e\mu_{s2} \leq 0, \end{aligned} \tag{4.24}$$

where $N_\lambda = \begin{bmatrix} \mu_a, & R_b^e \end{bmatrix}$ is the regressor matrix, ϵ_λ is a design parameter which can be arbitrarily small. Clearly, for $\tilde{R}_b^e$ sufficiently close to identify matrix $I_{3\times3}$, μ_{s2} can be chosen in a similar way as τ_{ps2}. Specifically, let h_λ be any smooth function satisfying $h_\lambda \geq (\gamma_\lambda\|\Theta_{HM1}\|\|N_\lambda\| + \|\Theta_{HM}\|\|N_\lambda\| + \delta_F)/\Theta_{H1min}$, where

$$\begin{aligned} \Theta_{HM} &= \Theta_{Hmax} - \Theta_{Hmin}, \\ \Theta_{HM1} &= [\max(|\Theta_{H1max}|, |\Theta_{H1min}|), \cdots, \\ &\quad \max(|\Theta_{H4max}|, |\Theta_{H4min}|)]^T, \end{aligned} \tag{4.25}$$

and γ_λ is a small positive constant to suppress the effect of $\tilde{R}_b^e$ when it is close to but not equal to identity matrix. Then, μ_{s2} can be chosen as

$$\mu_{s2} = -\frac{1+\gamma_\lambda}{4\Theta_{H1min}\epsilon_\lambda}h_\lambda^2 s_\lambda. \tag{4.26}$$

If F_{pd}^e in the dynamic equation (4.21) is replaced by the virtual control law (4.22), with the adaptation function in (4.10) chosen as $\sigma_H = N_\lambda s_\lambda$, then:

1) In general, all signals are bounded. Furthermore, the positive definite function V_λ defined by $V_\lambda = \frac{1}{2}s_\lambda^T s_\lambda$ is bounded above by $V_\lambda(\infty) \leq \frac{\epsilon_\lambda}{\varepsilon_\lambda}$ at steady state, where $\varepsilon_\lambda = 2k_{\lambda2min}$, $k_{\lambda2min}$ is the minimum value of all the entries in $k_{\lambda2}$.

2) If after a finite time t_0, there exist parametric uncertainties only(i.e., $\tilde{F}_\Delta^b = 0, \forall t \geq t_0$), and the low-level attitude controller achieves perfect tracking, i.e., $\tilde{R}_b^e = I_{3\times3}$, then, in addition to results in 1), zero final tracking error is also achieved, i.e., $e_\lambda \to 0$ and $s_\lambda \to 0$ as $t \to \infty$.

The proof can be worked out in the same way as Theorem 4.4.1.

Connection between high-level and low-level controllers The high level controller designed above generates the virtual control law μ for position tracking. If the desired translational force vector F^e_{pd} is directly taken as μ, then assuming pre-specified desired roll and yaw angle trajectories, the three other unknown variables F^b_{py}, F^b_{pz}, and θ_d can be determined from solving the equations $F^e_{pd} = R^e_b(\phi_d, \theta_d, \psi_d)[0, F^b_{py}, F^b_{pz}]^T$. And then θ_d obtained is fed into the low-level attitude controller.

This type of method has been used extensively in UAV controls, even the most recent research such as [65]. However, it cannot generate $\dot{\theta}_d$ and $\ddot{\theta}_d$ instantaneously, which are required for low-level trajectory tracking besides θ_d. We present two ways to avoid this problem:

- Method 1 (Using a 2^{nd} order filter for derivative generation)
  Let us first define the "reference" trajectory of pitch as θ_r. We solve the equations $R^e_b(\phi_d, \theta_r, \psi_d)[0, F^b_{py}, F^b_{pz}]^T = \mu$ to obtain F^b_{py}, F^b_{pz}, and θ_r in terms of known ϕ_d, ψ_d, μ:

$$\begin{aligned} F^b_{py} &= (\mu_x C_{\psi_d} + \mu_y S_{\psi_d})^2 S_{\phi_d} + \mu_z^2 S_{\phi_d} \\ &\quad +(\mu_x S_{\psi_d} - \mu_y C_{\psi_d}) C_{\phi_d}, \\ F^b_{pz} &= (\mu_x C_{\psi_d} + \mu_y S_{\psi_d})^2 C_{\phi_d} + \mu_z^2 C_{\phi_d} \\ &\quad +(\mu_x S_{\psi_d} - \mu_y C_{\psi_d}) C_{\phi_d}, \\ \theta_r &= atan\left(\frac{\mu_x C_{\psi_d} + \mu_y S_{\psi_d}}{\mu_z}\right). \end{aligned} \tag{4.27}$$

  Then, we use a fast 2^{nd} order filter to generate θ_d, $\dot{\theta}_d$ and $\ddot{\theta}_d$ from θ_r:

$$\begin{aligned} \theta_d &= \mathcal{L}^{-1}\left(\frac{\omega_n^2}{s^2+2\zeta\omega_n s+\omega_n^2}\right) * \theta_r, \\ \dot{\theta}_d &= \mathcal{L}^{-1}\left(\frac{\omega_n^2 s}{s^2+2\zeta\omega_n s+\omega_n^2}\right) * \theta_r, \\ \ddot{\theta}_d &= \mathcal{L}^{-1}\left(\frac{\omega_n^2 s^2}{s^2+2\zeta\omega_n s+\omega_n^2}\right) * \theta_r, \end{aligned} \tag{4.28}$$

  where $\mathcal{L}^{-1}$ denotes the inverse Laplace transform, $*$ denotes the convolution operator. The damping ratio ζ is often selected as 0.707 and the natural frequency is chosen sufficiently high to ensure a close following of θ_d with respect to θ_r. In practice, this method is very easy to implement. Although theoretically $F^e_{pd} \neq \mu$ using this method, they are very close with a sufficiently fast filter, and thus the performance is excellent, as can be seen from our experimental results.

- Method 2 (Using backstepping design for derivative generation)
  A more theoretically rigorous method is to treat $\ddot{F}^e_{pd}$ as the actual input instead of F^e_{pd}, and extends the high-level position control dynamics to 4^{th}-order. The additional dynamic equations from F^e_{pd} to $\ddot{F}^e_{pd}$ to be appended to (4.21) is thus

$$\begin{aligned} \frac{d(F^e_{pd})}{dt} &= \dot{F}^e_{pd}, \\ \frac{d(\dot{F}^e_{pd})}{dt} &= \ddot{F}^e_{pd}. \end{aligned} \tag{4.29}$$

  Then, two additional backstepping steps, same as [61], can be worked out to generate $\ddot{F}^e_{pd}$ from the virtual input μ in (4.22). Finally, the variables $\ddot{F}^b_{py}$, $\ddot{F}^b_{pz}$, $\ddot{\theta}_d$ are obtained by solving the expression of $\ddot{F}^e_{pd}$ in terms the three desired attitude angles, F^b_{py}, F^b_{pz} and their 1^{st} and 2^{nd}-order derivatives. This backstepping method is the rigorous way to address the problem in terms of control theory. But due to its mathematical complication and non-intuitive gain tuning process, it is not practically farorable as Method 1.

4.4.2 Constrained optimization for redundancy resolution

The goal of the second stage is to generate the individual thrust forces F_1, F_2, F_3, F_4 in positive scalars as well as two tilting angles α and β, such that the 5-DOF body force wrench generated by the ARC design is satisfied and certain objectives such as power consumption is minimized. Since each propeller thrust force F_i is proportional to the square of the rotating speed of the corresponding rotor, the total power consumption is roughly equal to $F_1 + F_2 + F_3 + F_4$. Thus, we aim at solving the following constrained optimization problem:

$$\begin{gathered} \min_{F_1,F_2,F_3,F_4,\alpha,\beta} F_1 + F_2 + F_3 + F_4, \\ \text{subject to} \\ F_i \geq 0,\ i = 1,2,3,4, \\ \tau^b_{px} = (F_1 + F_4) l_2 C_\alpha - (F_2 + F_3) l_2 C_\beta, \\ \tau^b_{py} = (F_1 - F_4)(C_\alpha l_1 + S_\alpha k) + (F_2 - F_3)(C_\beta l_1 - S_\beta k) \\ \tau^b_{pz} = (F_4 - F_1)(S_\alpha l_1 - C_\alpha k) + (F_3 - F_2)(S_\beta l_1 + C_\beta k). \\ F^b_{py} = (F_1 + F_4) S_\alpha + (F_2 + F_3) S_\beta, \\ F^b_{pz} = (F_1 + F_4) C_\alpha + (F_2 + F_3) C_\beta. \end{gathered} \tag{4.30}$$

The above nonlinear constrained optimization problem seems very computationally challenging and difficult to be solved online. However, we have discovered that it is feasible to use the Lagrange multiplier method to find out a simple relationship between the two tilting angles α and β, which eliminates the redundancy, and then use this relationship to precisely solve the 5 constrained equations in a very efficient way. Specifically, defining the objective function as $f(F_1, F_2, F_3, F_4)$, and the constrained equations as $g_i(F_1, F_2, F_3, F_4, \alpha, \beta)$, $i = 1, 2, 3, 4, 5$. The Lagrangia of the constrained optimization problem is

$$\begin{aligned} &\mathcal{L}\left(F_1, \ldots, F_4, \alpha, \beta, \lambda_1, \ldots, \lambda_5\right) = \\ &f\left(F_1, \ldots, F_4\right) + \sum_{k=1}^{5} \lambda_k g_k\left(F_1, \ldots, F_4, \alpha, \beta\right). \end{aligned} \tag{4.31}$$

At the local minimum point, the following first-order equalities must be satisfied:

$$\begin{aligned} &\nabla_{F_1,\ldots,F_4,\alpha,\beta,\lambda_1,\ldots,\lambda_5} \mathcal{L}\left(F_1, \ldots, F_4, \alpha, \beta, \lambda_1, \ldots, \lambda_5\right) = 0, \\ &\Longleftrightarrow \\ &\begin{cases} \nabla f\left(F_1, \ldots, F_4\right) + \sum_{k=1}^{5} \lambda_k \nabla g_k\left(F_1, \ldots, F_4, \alpha, \beta\right) = 0, \\ g_1\left(F_1, \ldots, F_4, \alpha, \beta\right) = \cdots = g_5\left(F_1, \ldots, F_4, \alpha, \beta\right) = 0. \end{cases} \end{aligned} \tag{4.32}$$

By solving equation (4.32) the following simple relationship between α and β can be found:

$$S_\alpha = S_\beta \iff \alpha = \beta \quad \text{or} \quad \alpha + \beta = \pi. \tag{4.33}$$

It means that the optimal tilting angles α and β are either the same, or sum up to π. In the former case, the thrust forces generated by the four propellers point to the same direction, while in the latter case the direction of the two front thrust forces and the direction of the two rear thrust forces are symmetric about the rotor's plane. The former case is usual for most of the hovering situations, and the latter case may occur when a large amount of torque in the roll direction needs to be generated, which usually happens when the vehicle is interacting with external environments (such as

screwing, valve opening, etc). In our algorithm, we plug in the two relationships to the five constrained equations, eliminating β, and solve for F_1, F_2, F_3, F_4, α with $F_1, F_2, F_3, F_4 \geq 0$. The solution with the smallest objective function value will be taken as the final optimal solution.

4.5 Applications to Aerial Locomotion and Manipulation

4.5.1 System Setup

In this section, we present experimental results on several challenging applications to validate the proposed new design and control for performing aerial locomotion and manipulation in unstructured environments. The newly designed multirotor is equipped with two tilting arms driven by two individual servo motors, which have well-controlled 180 deg rotation. The low-level attitude tracking control algorithm runs at $300Hz$ in a Lynxmotion MCU board on the aerial vehicle, with the roll and pitch angles and three angular velocities estimated at $300Hz$ using a PX4 Pixhawk module which communicates with the MCU through an UART port. An OptiTrack motion capture system is set up around the flight testing area to acquire attitude and position measurement of the vehicle at $120Hz$. The attitude and position information is sent back to a host computer running MATLAB code for high-level position control. The host computer communicates with the onboard flight controller via XBee modules at $120Hz$. The flight testing area is pictured in Figure 4.5.

4.5.2 Controller parameter selection

The controller parameters, including the low-level and high-level feedback gains and the parameter adaptation gains, are selected as follows: $k_{\eta 1} = diag\{10, 10, 10\}$, $k_{\eta 2} = diag\{0.8, 1.3, 4\}$, $k_{\lambda 1} = diag\{1.5, 1.5, 1.5\}$, $k_{\lambda 2} = diag\{0.5,$
$0.5, 0.5\}$, $\Gamma_L = diag\{0.1, 0.5, 0.5, 0.1, 0.1, 01, 5, 5, 5\}$, $\Gamma_H = diag\{0.1, 5, 5, 5\}$. The tuning of feedback and adaptation gains at each level starts with estimating the initial

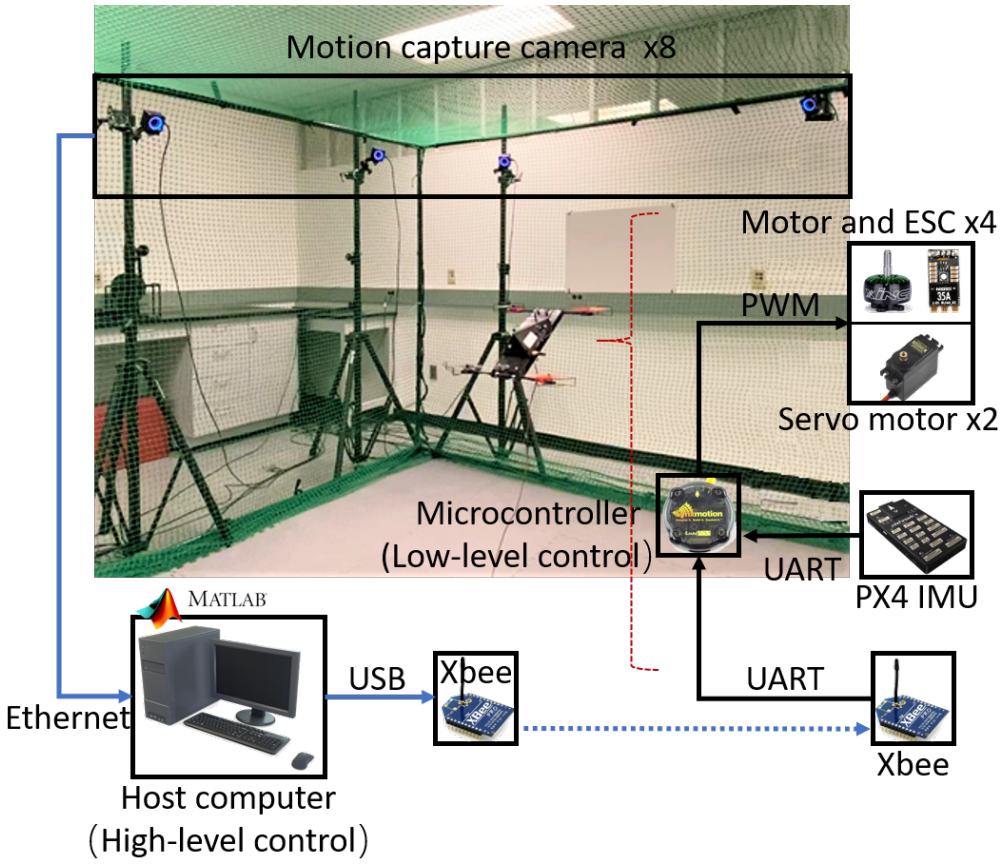

Figure 4.5 Overall system architecture of the novel UAV experiment, showing the key components of the system, and the data flow between onboard and off-board components.

values from a conservative prespecified closed-loop bandwidth [30]. These values are increased gradually during real flight testing until the tracking and parameter adaptation performance cannot be further improved without sacrificing system stability. The filter parameters for pitch angle trajectory generation are selected as $\zeta = 0.707$ and $\omega_n = 100 rad/sec$ to guarantee a sufficiently high bandwidth under the sampling rate constraint.

4.5.3 Applications with experimental results

We conduct four challenging experiments to demonstrate the novel multirotor vehicle's capability of performing enhanced maneuvering and manipulation in real applications. The video of the experiments is available at: https://youtu.be/jOAlprsPI9k.

Circular trajectory tracking In the first experiment, the vehicle is commanded to track a circular trajectory, where the desired position, roll angle and yaw angle are $x_d = 0.4sin(t)\ m$, $y_d = 0.4cos(t)\ m$, $z_d = 1.15\ m$, $\phi_d = 32\ deg$ and $\psi_d = 10sin(t)\ deg$. The actual x-y-z position and roll/yaw angle versus the desired values are plotted in Figure 4.6. From the figure, it is seen that the vehicle achieves sufficiently high tracking accuracy for both position and orientation. To validate the effectiveness of the optimization of thrust force, the graph of thrust forces delivered by the rotors is presented in Figure 4.7.

Passing through a narrow tunnel In the second experiment, we command the vehicle to pass through a narrow tunnel. The width of the tunnel is smaller than the length/width of the vehicle plus the propeller diameter. Thus, a traditional quadcopter of the same size is not able to complete the task. Thanks to our tilting-rotor design, we set the desired roll angle to 60 deg to shrink the horizontal body width, and increase the x-direction trajectory to let the vehicle slowly pass through the tunnel, as shown in Figure 4.8. The tracking performance is demonstrated in Figure 4.9. It can be seen that the proposed tilting-rotor UAV can adapt to the narrow tunnel by flipping up its body while maintaining a stable flight and accurate tracking, showing its enhanced capability of aerial locomotion in a constrained and possibly unstructured environment.

Picking up an object from a cluttered shelf Using UAV to pick up an object is the simplest yet one of the most frequently performed tasks of aerial manipulation.

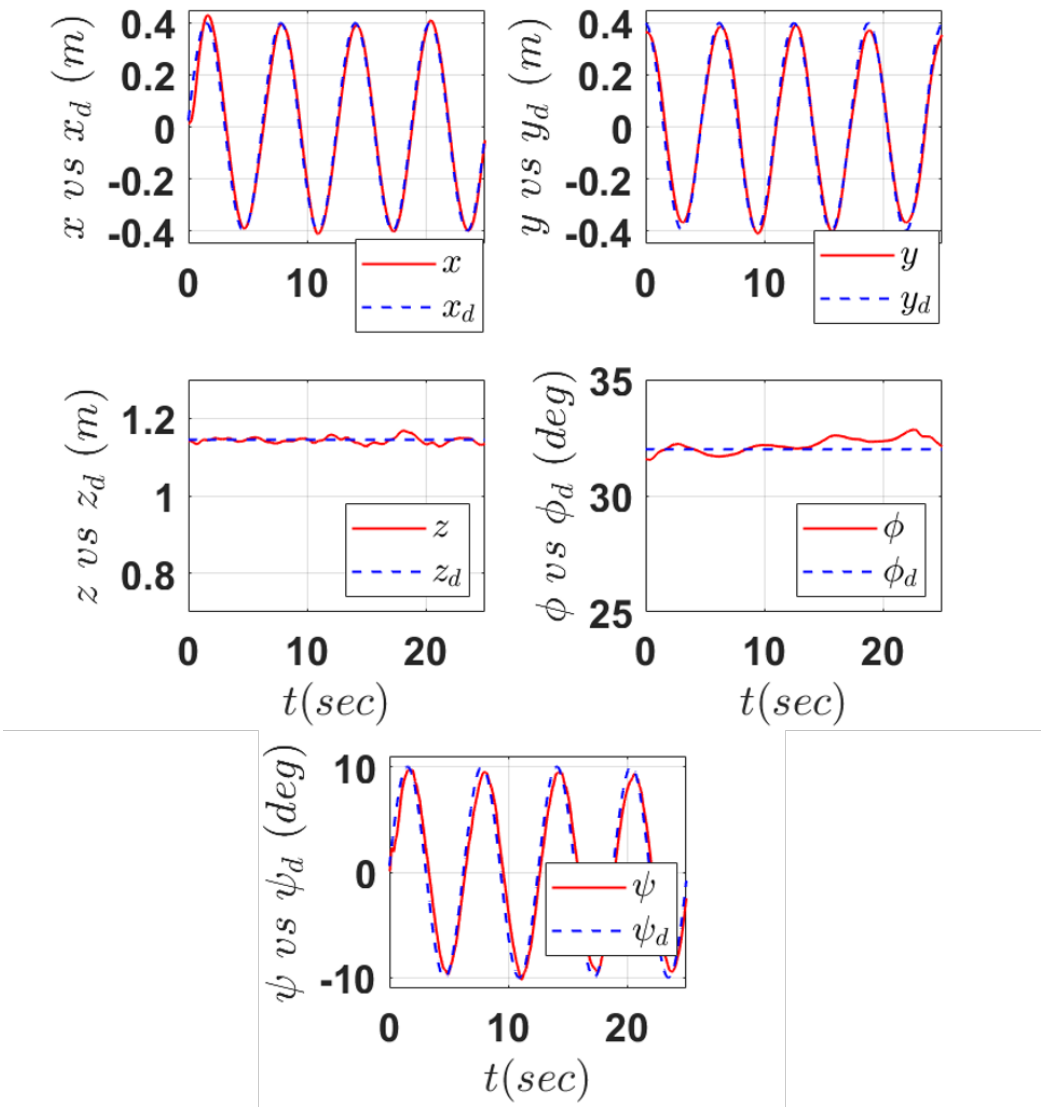

Figure 4.6 The circular trajectory tracking results, showing the X, Y, Z positions and the roll, yaw angles.

Existing research studies and commercial applications only focus on picking up objects from underneath the vehicle. However, in many situations, the object to be picked up is placed in a cluttered environment with obstacles around or above it. In this case, traditional methods fail to apply. In the third experiment, we command our novel vehicle to pick up a box on a shelf, on which there exist other objects and bars as constraints. To complete the task, we mount a small 1-DOF manipulator underneath

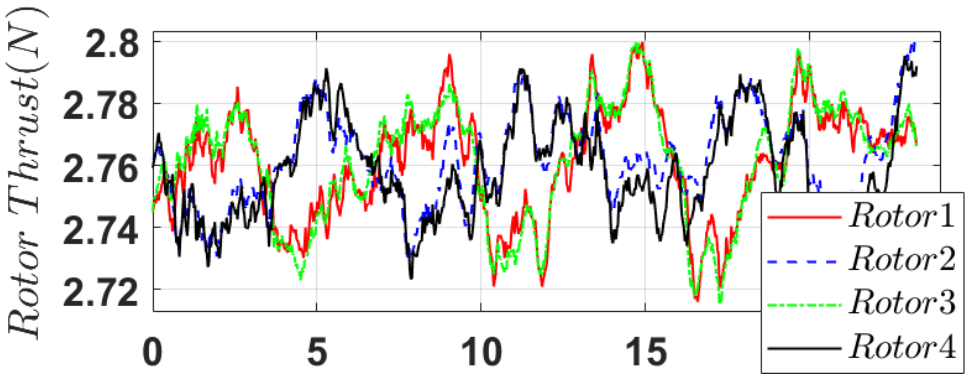

Figure 4.7 The thrust forces delivered by the rotors during circular trajectory tracking.

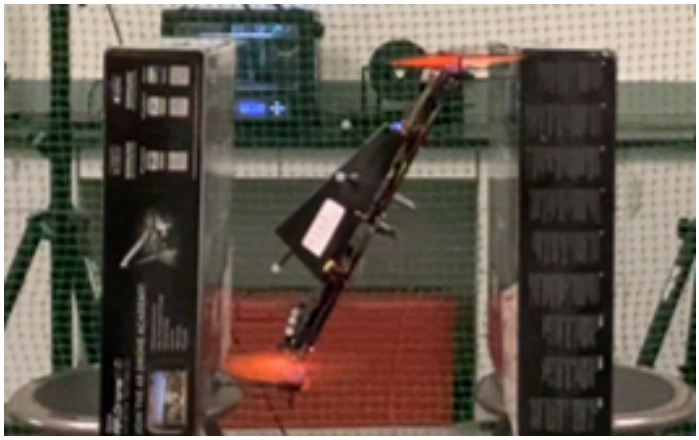

Figure 4.8 The proposed tilting-rotor UAV with a width of $0.6m$ flies through a narrow tunnel that is $0.45m$ wide by increasing its roll angle and maintaining a steep orientation.

the vehicle for reaching out to the object. The pickup process is simply illustrated by adding a small magnet to the tip of the manipulator to attract the other magnet on the box to achieve the pickup (which could be replaced by a parallel-jaw gripper in the future). Since the focus of this chapter is not on the automatic vision recognition and tracking of objects in a cluttered environment, we perform this experiment in a tele-operated manner, i.e., a human operator remotely commands the desired trajectory of the vehicle through an Xbox controller, as shown in Figure 4.10.

After the experiment starts, the vehicle first "flips up" its body (changing the roll angle to 50 deg), then approaches to the shelf and lifts up the manipulator,

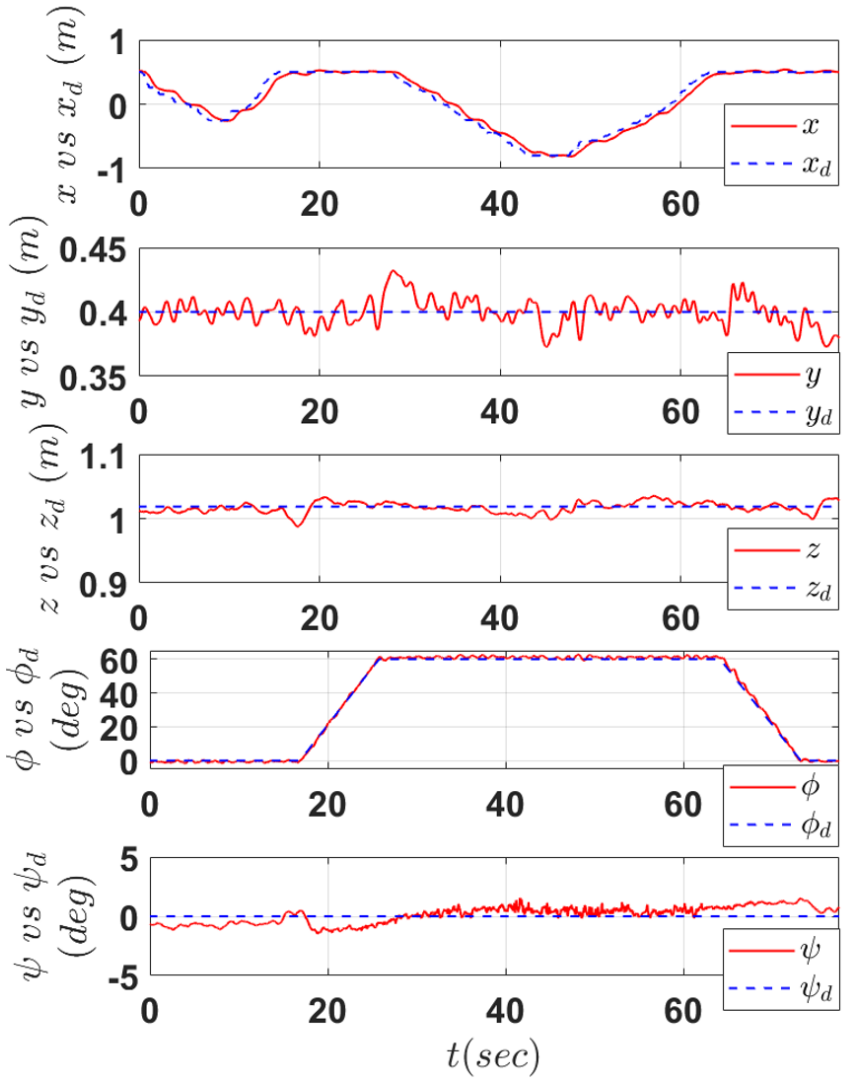

Figure 4.9 The tracking results of passing through a narrow tunnel, showing the X, Y, Z positions and the roll, yaw angles.

and finally picks up the object, retreats, and flips back to normal orientation. The snapshots of different stages of the experiment are shown in Figure 4.11, and the parameter adaptation results are shown in Figure 4.12 and 4.13. It can be seen that the vehicle can successfully pick up the object from a highly constrained environment by effectively coordinating its linear position, roll angle, and manipulator movement. After the payload jumps up, the estimated mass immediately converges to the true value. Although the estimates of moment of inertia parameters do not converge as

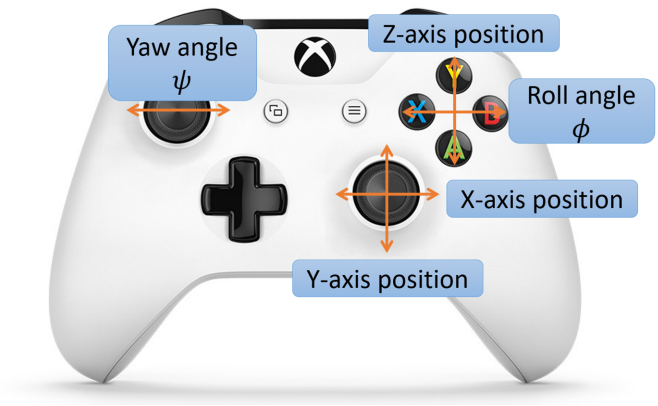

Figure 4.10 The joysticks and buttons of the Xbox controller used to remotely command the desired trajectory in experiment 3.

nicely as the mass due to minimum angular acceleration during the course of the experiment, the estimated uncertainty components do stand out, trying to compensate for the unmodeled effect caused by the change of center of mass.

Human-guided aerial hole drilling Hole drilling is a practically meaningful yet challenging task which demands complex hybrid motion-force control. Using UAV to perform aerial hole drilling has not been done before. One major difficulty is the coupling between translational and rotational motions for the traditional quadcopter design, which prevents the independent contact force regulation. Another main problem is the ineffective thrust force cancellation in various existing aerial manipulation platforms (as mentioned in the introduction), which makes it difficult to exert a sufficient force along the feeding direction to push the drill bit against the workpiece and penetrate its surface. These challenges can all be overcome by employing the proposed novel UAV design. A human-guided aerial hole drilling experiment is conducted in the lab to validate the enhanced aerial manipulation ability of the system, as shown in Figure 4.14. In the experiment, instead of designing more advanced controller such as impedance control along the feeding direction Y^e, we simply do a slight modification to the existing high-level ARC controller to show the

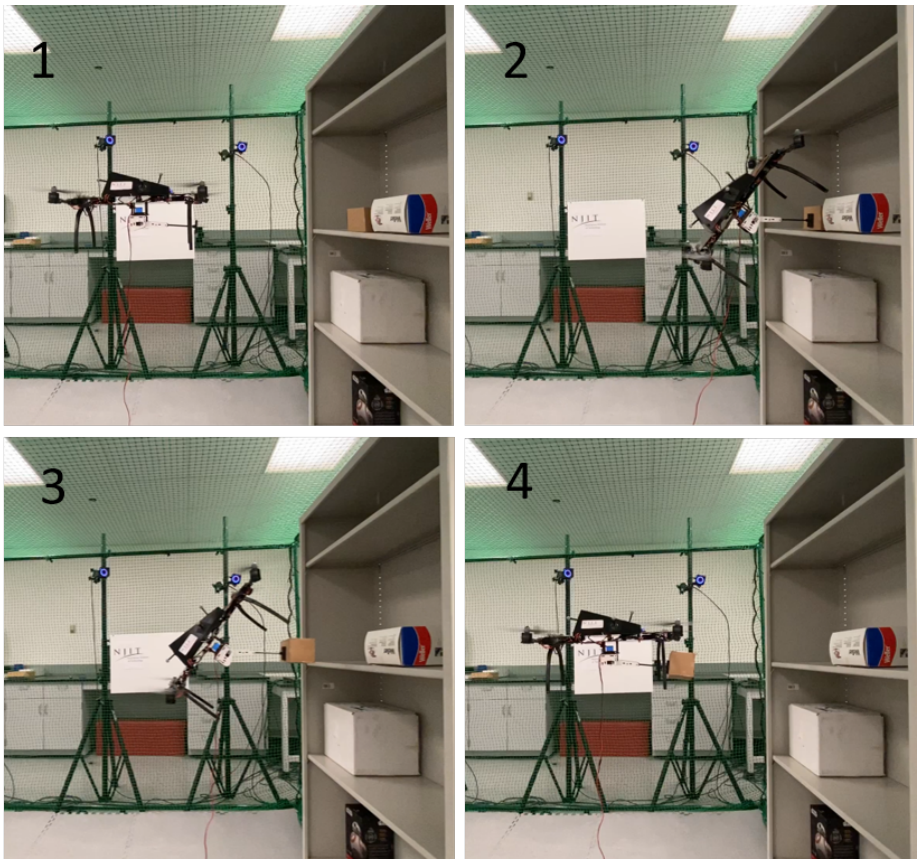

Figure 4.11 Different stages of the object picking-up experiment (experiment 3): 1. the vehicle starts from hovering in the air; 2. the vehicle changes its roll angle to 50 deg and approaches to the shelf; 3. the vehicle picks up the object and retreats; 4. the vehicle changes its roll angle back to 0.

proof-of-concept hole-drilling process. Specifically, after the drill bit touches the wood board, the desired thrust force F^e_{pd} along Y^e direction is set to be directly commanded by human instead of synthesized through the ARC position control law. This is to let the human operator directly tune the desired contact force during the drilling process. The feeding rate and position of the aerial manipulator are plotted in Figure 4.15, along with the corresponding force command. After less than $15sec$, the $12mm$ thick wood board is drilled through, showing the effectiveness of our approach in hole-drilling applications.

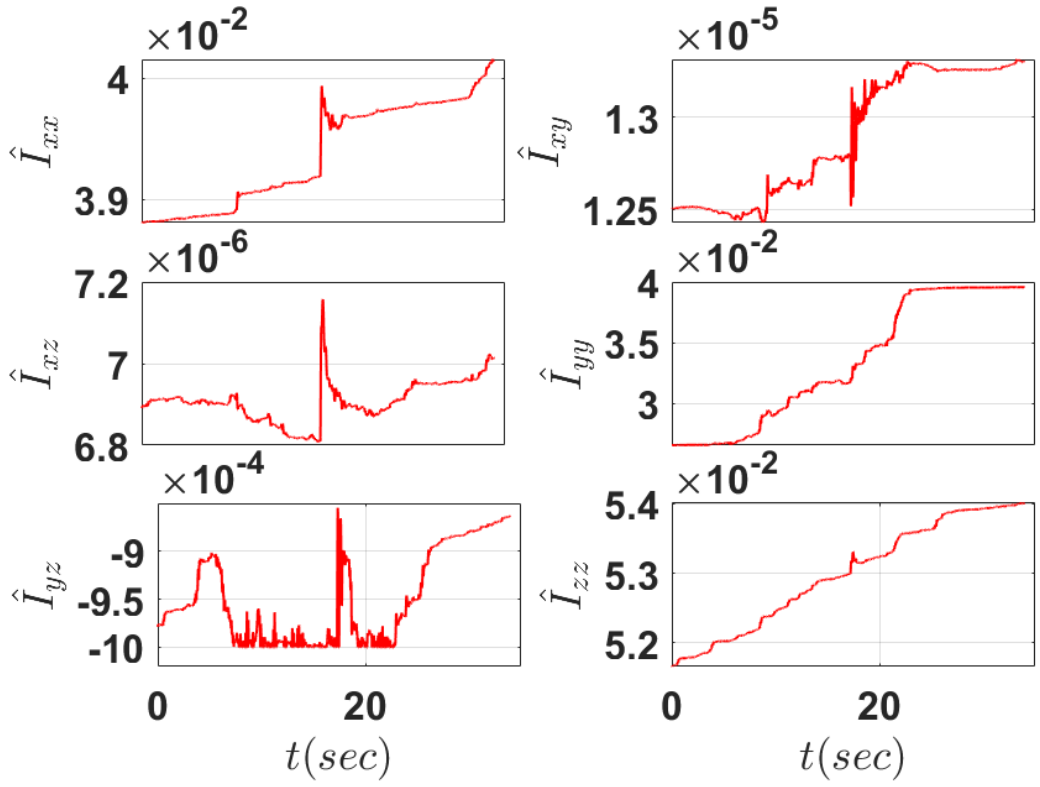

Figure 4.12 The estimates of moment of inertial parameters.

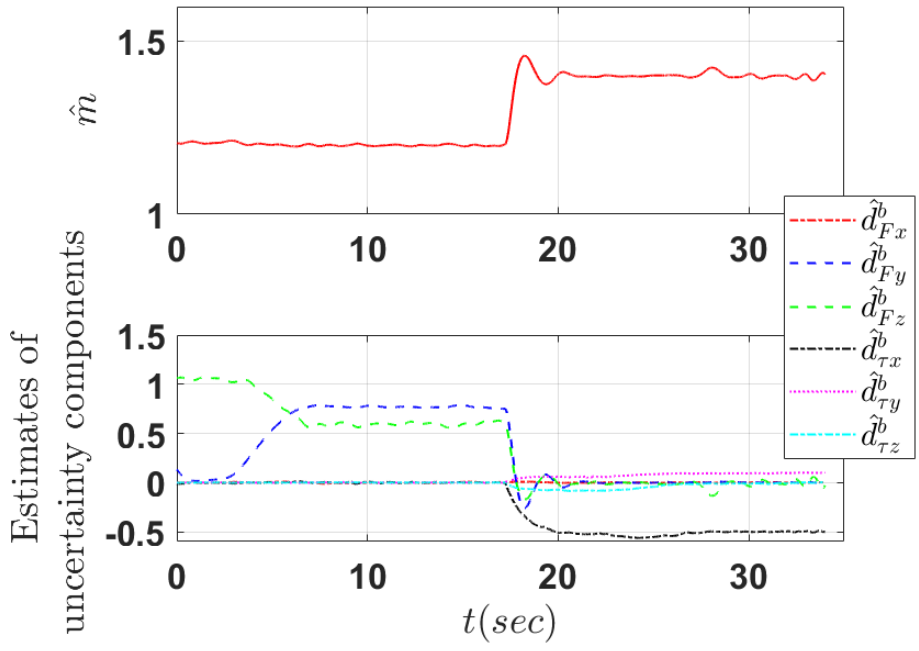

Figure 4.13 The estimates of mass and uncertainty components.

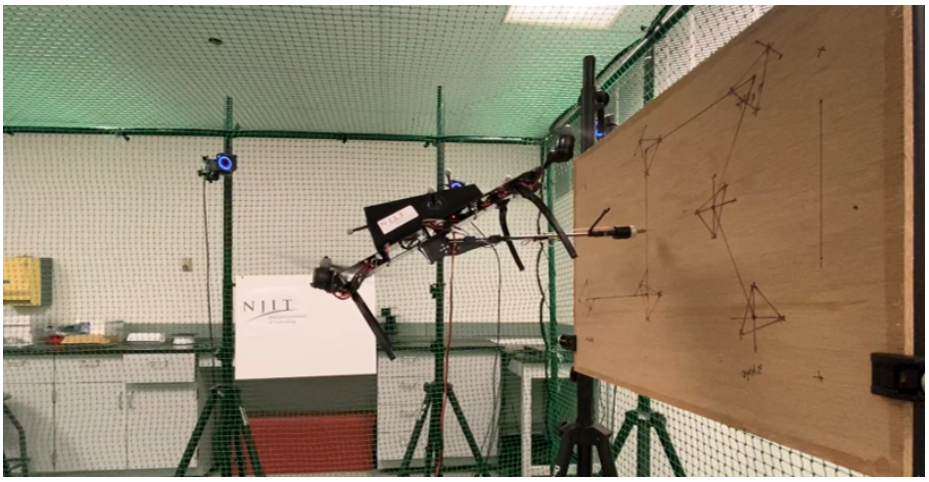

Figure 4.14 The human-guided aerial hole drilling experiment on a 12*mm* thick wood panel board. A custom-designed drill with a 1*mm* drill bit is mounted to the end-effector for this experiment.

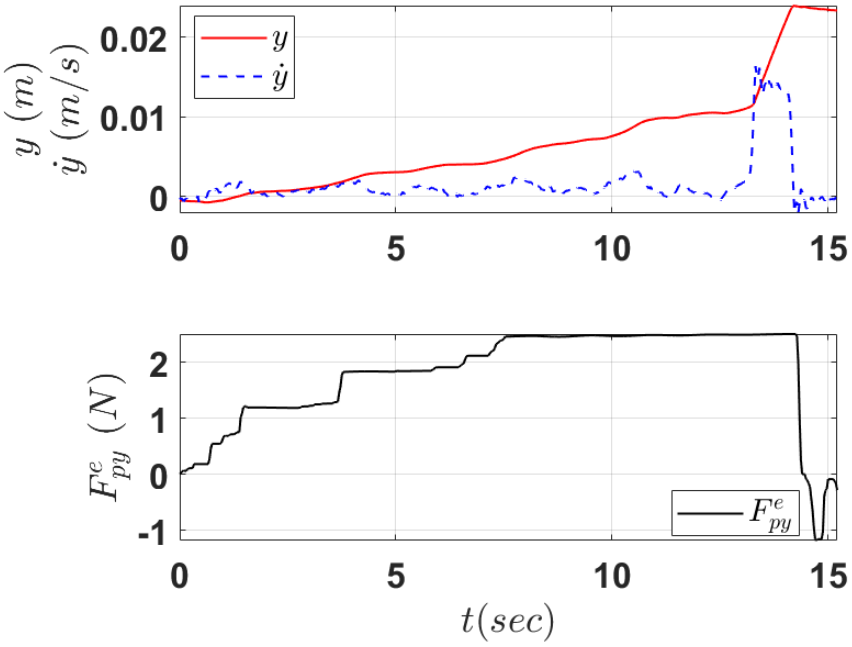

Figure 4.15 The position, velocity, and the corresponding force command along the Y^e direction in the aerial hole drilling experiment.

4.6 Conclusions

In this study, we proposed the design, control and applications of a novel multirotor UAV for enhanced aerial locomotion and manipulation performances. The aerial vehicle

employs a tilting-rotor architecture, and was designed to be in an "H" configuration. With such a design, the UAV has independent roll angle regulation to be able to perform challenging aerial locomotion and manipulation tasks, at the expense of only two additional servo motors with minimum transmission needed. Based on the dynamics of the proposed UAV, we formulated a dual-level adaptive robust control (ARC) method to cope with parametric uncertainties and uncertain nonlinearities that may occur during aerial maneuvering and manipulation. Additionally, we proposed and precisely solved a thrust force optimization problem minimizing power consumption while achieving the desired body force wrench to efficiently resolve the redundancy in actuation. Finally, we validated the applicability of the complete system through four challenging experiments: tracking a circular trajectory, passing through a narrow tunnel, picking up an object from a cluttered shelf, and human-guided hole drilling. Experimental results showed the superior performance of the design and control when performing real demanding aerial locomotion and manipulation tasks in unstructured environments.

CHAPTER 5

DESIGN, SENSING, AND CONTROL OF A NOVEL UAV PLATFORM FOR AERIAL DRILLING AND SCREWING

5.1 Introduction

As Unmanned Aerial Vehicles (UAVs) are technologically maturing, novel applications of UAVs have sprung forth that exploit and extend their inherent aerial capabilities. In particular, an increasing number of applications require UAVs to actively interact with environment rather than simply serving as a passive sensing platform. Among them, aerial manipulation tasks, such as grasping [66], fetching [67], writing [68], peg-in-hole [69], and object transporting are of particular interest to researchers, as they can potentially replace human workers in a variety of construction, maintenance, and transportation tasks to be performed at hard-to-reach or dangerous locations. However, these tasks are at an entry level and require only very basic interaction between UAV and environment. Many practically meaningful applications that involve sophisticated contact and force control remain hardly achievable under the traditional design and control of aerial manipulators. Particularly, hole drilling and screwing tasks, as two of the most common and essential operations to be conducted together in engineering, have only been touched in the aerial manipulation scenario to a very limited extent, e.g., vertical drilling down to the ground or a workpiece [70, 71, 72, 73].

The frequently performed drilling and screwing operations share some features in common. Specifically, there are two forces (torques) present in both operations. One is the pushing (pressing) force normal to the surface of the workpiece, and the other is the torque around the normal axis. To achieve a successful drilling/screwing operation, a strong pushing force must be exerted, while the other degrees of freedom of the end-effector should be accurately position-controlled despite the reaction normal force and torque. Such a feature makes it problematic for traditional quadcopter

platforms to implement drilling and screwing on a vertical wall no matter how the onboard manipulator is designed. This is because traditional quadcopters are highly underactuated, with the translational motion on the horizontal plane tightly coupled with rotational motion. In order to compensate for the strong contact force along the horizontal drilling/screwing direction, the body of the quadcopter has to rotate, letting the propellers face sideways to generate sufficient propulsion force. Whereas, frequently tilting UAV's body to match the desired contact force will make the system highly unstable. Therefore, accurate position-level control along other degrees of freedom is impossible.

Thus, it is clear that the translation and rotation of the UAV body need to be independently controlled at least along a certain horizontal direction for a successful drilling/screwing. This requires the UAV body to have a degree of freedom of actuation higher than four. Various fully-actuated (6-DOF) UAVs and 5-DOF actuated UAVs have been proposed up to date. Depending on the designs, they can be classified into two categories. The first one uses multiple fixed rotors facing different directions to achieve higher-DOF actuation [5, 6, 74, 69]. This type of design is structurally simple. But since the rotors point to different directions, ineffective internal force cancellation will inevitably occur, lowering the power efficiency and load capacity of the vehicles. The second type of design employs a tilting-rotor structure, i.e., the introduction of one/two extra servo motors for each rotor to empower it with one/two-axis tilting ability[7, 1, 8, 75]. With the additional tilting capability of the rotor axes, this type of design can partially or completely avoid ineffective force cancellation. However, the inclusion of a large number of movable servo parts makes the designs mechanically more complicated, with other potential problems such as higher weight and backlash from the intricate transmission system.

Besides the issue of the architecture and design, there still exist other challenges unique to the aerial drilling and screwing. For example, how to identify and

precisely track the target for drilling/screwing, how to smoothly incorporate human users' command into the system, and how to achieve contact force regulation while maintaining accurate position-level control in other DOFs, remain to be solved. In this chapter, we present a human-guided semi-automated aerial drilling/screwing platform based on a novel tilting-rotor aerial manipulator design. The design features a novel quadrotor UAV with each pair of rotors independently tilted by a servo, forming an "H" configuration, on which a simple 1-DOF manipulator carrying a motorized drill or screw driver is mounted, moving on the longitudinal plane. With only three additional servos needed (two for UAV body and one for manipulator) compared to the traditional coplanar quadcopters, the controls of the body's translational and rotational motions on the longitudinal plane are completely decoupled, and the end-effector can face any direction to apply a strong contact force for drilling and screwing on the longitudinal plane without the need of changing the vehicle body's orientation. Thus, the proposed platform can achieve omnidirectional drilling/screwing. Based on the dynamics of the proposed UAV design, a dual-level control law is proposed. The low-level attitude controller uses an adaptive robust control (ARC) to accurately regulate the attitude angles in the presence of force/torque uncertainties that may occur during the drilling and screwing process, while a selective impedance controller is implemented at high level to indirectly control the contact force commanded by the user. In addition, a vision-based guidance scheme is developed to identify and track the target feature on the workpiece. For verification, we conduct various indoor hole drilling and bolt screwing experiments on a vertical wood plate to show the applicability of our approach.

5.2 System Architecture And Mechanical Design

From the previous discussion, it is clear that the key to successfully implementing ominidirectional aerial drilling/screwing is to allow the end-effector face any desired

feeding direction and exert a sufficiently large force while maintaining a stable UAV posture. To solve this challenge, we develop a novel quadrotor with two tiltable arms as the UAV body, on which a 1-DOF manipulator carrying a motorized drill or screw driver is mounted, as shown in Figure 5.1. Specifically, the UAV platform consists of two pairs of rotors mounted on two independently-actuated arms placed at both sides of the vehicle in an "H" configuration, similar to [76, 77]. Each arm is tilted by a single servomotor, allowing independent adjustment of the thrust force direction of the pair of rotors it carries. Then, a 1-DOF lightweight manipulator carrying a self-designed drilling/screwing end-effector is mounted. The joint of the manipulator rotates on the longitudinal plane and is driven by a servo to align the drill/screwdriver with the desired feeding direction. To generate the spinning motion for the drilling/screwing process, we use a micro DC motor with $5V/2.5A$ power input to carry the tool and fix it to the end-effector. Additionally, a vision camera is installed on the manipulator. This eye-in-hand configuration is used to position and track a target point on an object of interest to complete aerial hole drilling and screwing tasks.

Such a configuration has the following advantages which make it a perfect choice for aerial drilling/screwing platform:

1. By changing the two tilting angles α and β and the manipulator angle γ, the vehicle body can be actuated in 5 DOFs independently, while the end-effector can face any direction on the longitudinal plane (Y^bZ^b plane) and independently exert a large enough contact force. This feature is particularly useful when conducting drilling/screwing on a vertical wall.
2. Ineffective internal propeller force cancellation can be avoided by setting $\alpha = \beta$, making the design energy efficient.
3. Only three additional servos (two for UAV body and one for manipulator) are used compared to traditional quadcopters with no extra transmission mechanism needed, leading to a less total weight and less probability of fault occurrence than other designs with too many servos.

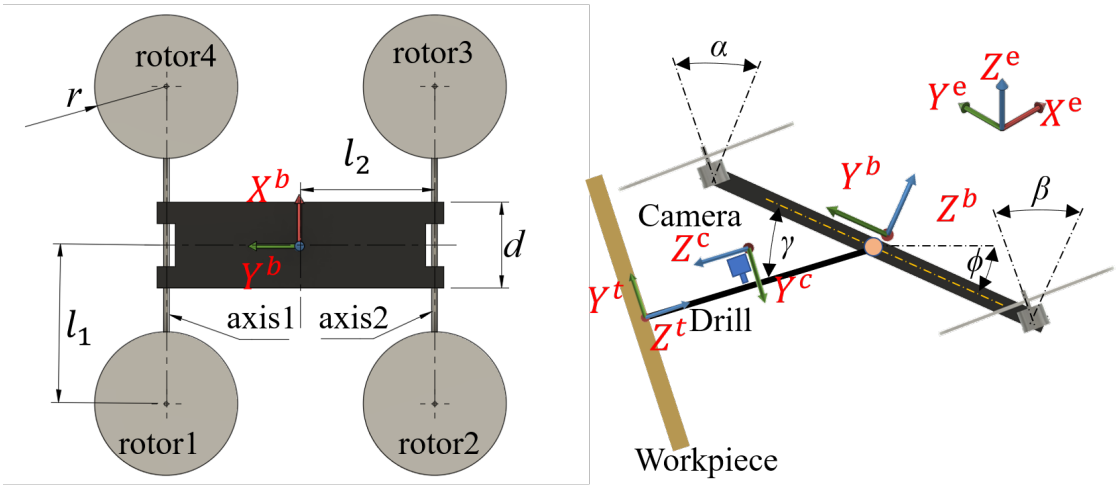

Figure 5.1 The top view and front view of the proposed aerial drilling/screwing platform. α and β are the tilting angles of the two left motors and two right motors about axis1 and axis2 respectively. ϕ is the roll angle of the vehicle's body. γ is the rotating angle of the 1-DOF onboard manipulator.

5.3 System Modeling

5.3.1 Coordinate systems and assumptions

The following right-hand coordinate systems will be used throughout the rest of the chapter, as shown in Figure 5.1.

$\{e\}$: The earth (inertial) frame $\{O_e - X^eY^eZ^e\}$.

$\{b\}$: The UAV body-fixed frame $\{O_b - X^bY^bZ^b\}$.

$\{c\}$: The camera frame $\{O_c - X^cY^cZ^c\}$.

$\{t\}$: The target frame $\{O_t - X^tY^tZ^t\}$.

It is assumed that the origin of the body frame O_b is located at the center of mass of the UAV. The origin of the target frame O_t is located at the target point on the workpiece to drill or screw in, and the axis Z^t is perpendicular to the workpiece surface. Furthermore, since the 1-DOF onboard manipulator weights much less compared to the UAV body and its servomotor has very quick response and high tracking accuracy, we can safely ignore the dynamics of the manipulator and simply set the manipulator

angle $\gamma = \phi + \angle(Z^t, X^eY^e)$, where ϕ is the roll angle of the UAV body, and $\angle(Z^t, X^eY^e)$ is the angle between the drill/screw direction Z^t and the X^eY^e plane of the inertia frame. This choice of γ allows the end-effector to be aligned with the drilling/screwing direction.

5.3.2 Forces and torques

Since the dynamics of the manipulator is ignored, all the contact forces and torques during the drilling/screwing process are directly transmitted to the UAV body. The total force acting on the UAV expressed in the body coordinate system is described as :

$$F^b = \begin{bmatrix} F_x^b & F_y^b & F_z^b \end{bmatrix}^T = F_p^b + F_g^b + F_c^b, \tag{5.1}$$

where $F_p^b = \sum_{i=1}^{4} F_{p_i}^b$ is the total thrust force which equals to the sum of all individual thrust forces expressed in body frame $\{b\}$. $F_g^b = mR_b^{eT}G$ is the gravitational force expressed in the body frame, m is the total mass of the UAV, $G = [0 \;\; 0 \;\; -g]^T$ is the gravitational acceleration vector in inertia frame. $F_c^b \in R^3$ is the lumped contact force between end-effector tool and the workpiece represented in body frame.

It is noted that since the propeller cannot rotate around Y^b, the projection of the thrust force onto X^b is equal to zero, i.e., $F_p^b = [0 \;\; F_{py}^b \;\; F_{pz}^b]^T$. Defining F_1, F_2, F_3, F_4 as the absolute values of the thrust forces of the four propellers and α, β as the front and rear tilting angles, as shown in Figure 5.1, the F_{py}^b and F_{pz}^b can be expressed as:

$$\begin{aligned} F_{py}^b &= (F_1 + F_4)S_\alpha + (F_2 + F_3)S_\beta, \\ F_{pz}^b &= (F_1 + F_4)C_\alpha + (F_2 + F_3)C_\beta. \end{aligned} \tag{5.2}$$

The total torque acting on the UAV expressed in the body frame is

$$\tau^b = \begin{bmatrix} \tau_x^b & \tau_y^b & \tau_z^b \end{bmatrix}^T = \tau_p^b + \tau_\Delta^b, \tag{5.3}$$

where $\tau_p^b = \sum_{i=1}^{4} r_i^b \times F_{p_i}^b + \sum_{i=1}^{4} D_i k F_{p_i}^b$ is the total torque generated by the propellers, including the thrust torque $\sum_{i=1}^{4} r_i^b \times F_{p_i}^b$ and drag torque $\sum_{i=1}^{4} D_i k F_{p_i}^b$, in which r_i^b is the coordinate vector of the center of the *i-th* propeller in body frame, k is a constant ratio of drag torque to thrust force, and D_i is a constant equal to 1 when the *i-th* propeller rotates in clockwise direction, and -1 when it rotates in counterclockwise direction. $\tau_\Delta^b \in R^3$ is the torque uncertainty incorporating the uncertain reaction torque between end-effector tool and the workpiece, and the torque caused by the contact force.

Defining l_1 as the half distance between the two rotors on each tilting axis, l_2 as the half distance between the two tilting axes, the x, y, z components of τ_p^b can be expressed as

$$\begin{aligned} \tau_{px}^b &= (F_1 + F_4) l_2 C_\alpha - (F_2 + F_3) l_2 C_\beta, \\ \tau_{py}^b &= (F_1 - F_4)(C_\alpha l_1 + S_\alpha k) + (F_2 - F_3)(C_\beta l_1 - S_\beta k), \\ \tau_{pz}^b &= (F_4 - F_1)(S_\alpha l_1 - C_\alpha k) + (F_3 - F_2)(S_\beta l_1 + C_\beta k). \end{aligned} \tag{5.4}$$

5.3.3 Dynamic model

The system dynamics are derived in the Newton-Euler form as

$$\begin{bmatrix} F^b \\ \tau^b \end{bmatrix} = \begin{bmatrix} M & 0 \\ 0 & I^b \end{bmatrix} \begin{bmatrix} \dot{v}^b \\ \dot{\omega}^b \end{bmatrix} + \begin{bmatrix} \omega^b \times M v^b \\ \omega^b \times I^b \omega^b \end{bmatrix}, \tag{5.5}$$

where $v^b = \begin{bmatrix} v_x^b & v_y^b & v_z^b \end{bmatrix}^T$ and $\omega^b = \begin{bmatrix} \omega_x^b & \omega_y^b & \omega_z^b \end{bmatrix}^T$ are the vectors of vehicle's translational and angular velocities represented in body frame. I^b is the moment of inertia about the center of mass. $M = m \cdot I_3$ is the mass matrix.

5.3.4 Kinematic relationship

Let $\lambda = \begin{bmatrix} x & y & z \end{bmatrix}^T$ be the vehicle's position (the coordinate of the body frame origin O_b) expressed in inertia frame $\{e\}$, $\eta = \begin{bmatrix} \phi & \theta & \psi \end{bmatrix}^T$ be the attitude vector of the vehicle.

The kinematic relationship between the position/attitude of the vehicle and the body frame velocity is given by the following two equations:

$$\dot{\lambda} = R_b^e v^b, \quad \dot{\eta} = \Psi \omega^b, \tag{5.6}$$

where $\Psi = \begin{bmatrix} 1 & S_\phi T_\theta & C_\phi T_\theta \\ 0 & C_\phi & -S_\phi \\ 0 & \frac{S_\phi}{C_\theta} & \frac{C_\phi}{C_\theta} \end{bmatrix}$ is the transformation matrix at kinematic level.

5.4 Control Design

Based on the dynamics, a dual-level control architecture is proposed as illustrated in Figure 5.2. The low-level attitude controller uses an adaptive robust control (ARC) to accurately regulate the attitude angles in the presence of force/torque uncertainties that may occur during the drilling and screwing process, while a selective impedance controller is implemented at high level to indirectly control the contact force commanded by the user and track the target position in X^tY^t plane. Finally, the five body-frame force and torque inputs will be used to generate the propeller thrust force commands and the tilt angle set points to be fed into the rotors and servos. It is noted that since the system has 5-DOF independent actuation (one more DOF than traditional fix-rotor quadcopters), only the desired pitch angle θ_d is indirectly determined inside the control loop, while the desired setpoints for all the other DOFs are either determined from the target position/orientation or specified by the user. Specifically, $x_d^t = y_d^t = 0$ to let the UAV follow the target position in X^tY^t plane, z_d^t comes from the user-specified contact force setpoint to be discussed later in the impedance control design, the desired roll angle ϕ_d is specified by the user, and $\psi_d = \angle(proj(Z^t, X^eY^e), X^e)$ guarantees the manipulator side of the vehicle is facing the target.

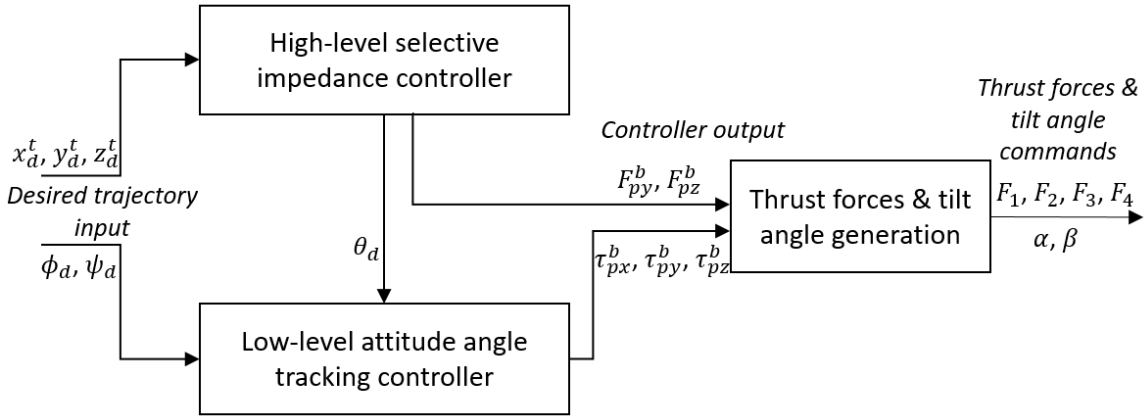

Figure 5.2 The schematics of the proposed dual-level control strategy.

5.4.1 Low-level attitude control

The adaptive robust control (ARC) has demonstrated its powerfulness in many industrial applications that require precision motion control [30, 78, 79]. Specifically, ARC can effectively deal with both parametric uncertainties and uncertain nonlinearities in the system and accurate motion tracking. Thus, ARC is a perfect choice of controller for the low-level attitude angle control of the drilling/screwing operation in which a high tracking accuracy is required even in the presence of strong contact force/torque uncertainties. To proceed with the proposed ARC design, we first define

$$\begin{aligned} \Theta &= [d_{\tau x}^b,\ d_{\tau y}^b,\ d_{\tau z}^b]^T, \\ \tilde{\tau}_\Delta^b &= \tau_\Delta^b - d_\tau^b = \tau_\Delta^b - [d_{\tau x}^b,\ d_{\tau y}^b,\ d_{\tau z}^b]^T, \end{aligned} \tag{5.7}$$

where Θ is the vector of constant portion of the lumped torque uncertainties to be adapted, and $\tilde{\tau}_\Delta^b$ is the time-varying portion. The following practical assumption is made on the uncertainties [30]:

The extent of the parametric uncertainties and uncertain nonlinearities are known, i.e.,

$$\begin{aligned} \Theta \in \Omega_\Theta &\triangleq \{\Theta : \Theta_{min} \le \Theta_L \le \Theta_{max}\}, \\ \tilde{\tau}_\Delta^b \in \Omega_{\tilde{\tau}_\Delta^b} &\triangleq \{\tilde{\tau}_\Delta^b : |\tilde{\tau}_\Delta^b| \le \delta_\tau\}, \end{aligned} \tag{5.8}$$

where $\Theta_{min} = [\Theta_{1min}, \Theta_{2min}, \Theta_{3min}]^T$, $\Theta_{max} = [\Theta_{1max}, \Theta_{2max}, \Theta_{3max}]^T$, and δ_τ are the known bounds of the uncertainties.

Let $\hat{\Theta}$ denote the estimate of Θ, and $\tilde{\Theta}$ the estimation error (i.e., $\tilde{\Theta} = \hat{\Theta} - \Theta$). The following adaptation law with discontinuous projection modification is used:

$$\dot{\hat{\Theta}} = Proj_{\hat{\Theta}}(\Gamma\sigma), \tag{5.9}$$

where $\Gamma > 0$ is the diagonal matrix of adaptation gains, σ is the adaptation function to be synthesized later. The projection mapping $Proj_{\hat{*}}(\bullet) = [\cdots \quad Proj_{\hat{*}_i}(\bullet_i) \quad \cdots]^T$ is defined as

$$Proj_{\hat{*}_i}(\bullet_i) = \begin{cases} 0, & \text{if } \hat{*}_i = *_{imax} \text{ and } \bullet_i > 0, \\ 0, & \text{if } \hat{*}_i = *_{imin} \text{ and } \bullet_i < 0, \\ \bullet_i, & \text{otherwise.} \end{cases} \tag{5.10}$$

It can be shown that for any adaptation functions σ_L and σ_H, the projection mappings used in (5.10) guarantees

$$\begin{aligned} &\textbf{P1} \qquad \hat{\Theta} \in \Omega_\Theta, \\ &\textbf{P2} \qquad \tilde{\Theta}^T(\Gamma_L^{-1} Proj_{\hat{\Theta}}(\Gamma\sigma) - \sigma) \leq 0. \end{aligned} \tag{5.11}$$

Let $\eta_d(t) = [\phi_d(t)\ \theta_d(t)\ \psi_d(t)]^T$ be the desired attitude angle trajectory, and $e_\eta = \eta - \eta_d$ be the attitude tracking error. We define the following switching-function-like quantity for the attitude tracking error as

$$s_\eta = \Psi^{-1}(\dot{e}_\eta + k_{\eta 1} e_\eta) = \omega^b - \Psi^{-1}\dot{\eta}_d + \Psi^{-1} k_{\eta 1} e_\eta, \tag{5.12}$$

where $k_{\eta 1} > 0$ is a diagonal gain matrix. Clearly, if s_η is small or converges to zero exponentially, then the attitude tracking error e_η will be small or converge to zero exponentially. So the rest of the design is to make $s_\eta \to 0$. Differentiating (5.12) and

using (5.5):

$$\begin{aligned} I^b \dot{s}_\eta &= I^b \dot{\omega}^b - I^b [\dot{\Psi}^{-1} \dot{\eta}_d + \Psi^{-1} \ddot{\eta}_d - \dot{\Psi}^{-1} k_{\eta 1} e_\eta \\ &\quad -\Psi^{-1} k_{\eta 1} (\Psi \omega^b - \dot{\eta}_d)] \\ &= \tau_p^b + \Theta + B + \tilde{\tau}_\Delta^b, \end{aligned} \tag{5.13}$$

where $B = -(I^b \omega^b) \times \omega^b - I^b [\dot{\Psi}^{-1} \dot{\eta}_d + \Psi^{-1} \ddot{\eta}_d - \dot{\Psi}^{-1} k_{\eta 1} e_\eta - \Psi^{-1} k_{\eta 1} (\Psi \omega^b - \dot{\eta}_d)]$ is the known nonlinear term to be compensated directly.

The following control law is proposed:

$$\tau_p^b = \tau_{ps}^b + \tau_{pa}^b, \quad \tau_{pa}^b = -\hat{\Theta} - B, \tag{5.14}$$

where τ_{pa}^b is the adjustable disturbance compensation term, τ_{ps}^b is the robust feedback term synthesized as

$$\tau_{ps}^b = \tau_{ps1}^b + \tau_{ps2}^b, \quad \tau_{ps1}^b = -k_{\eta 2} s_\eta, \tag{5.15}$$

where τ_{ps1}^b is a proportional feedback term with $k_{\eta 2} > 0$ being the diagonal gain matrix. τ_{ps2}^b is a robust feedback to attenuate the effect of nonlinear model uncertainties caused by parameter estimation error, which satisfies the following two conditions:

$$\begin{aligned} &1. \quad s_\eta^T (\tau_{ps2}^b - \tilde{\Theta}_L + \tilde{\tau}_\Delta^b) \leq \epsilon_\eta, \\ &2. \quad s_\eta^T \tau_{ps2}^b \leq 0, \end{aligned} \tag{5.16}$$

where ϵ_η is a design parameter which can be arbitrarily small and τ_{ps2} can be chosen according to the previous research [30]. Similar to [30], theoretical results on the robust performance and asymptotic tracking can be obtained, which are omitted here due to page limit.

5.4.2 High-level selective impedance control

In the high level, the 3-DOF translation of the vehicle's body is controlled such that the end-effector applies the user-specified desired contact force F_{cd} normal to the workpiece surface, while the coordinates along the two other DOFs closely track the point to drill or screw in. To achieve this goal, we first transform the position coordinates of the vehicle from inertia frame to the target frame whose origin coincides with the point to drill/screw and Z^t axis is perpendicular to the workpiece surface, then derive the decoupled system dynamics along X^t, Y^t, Z^t directions of the target frame. Based on this dynamics, a selective impedance control is designed such that the user can specify different impedance parameters to achieve different force-position characteristics along different axes of the target frame.

To begin with, let us define $\lambda^t = [x^t \ y^t \ z^t]^T$ as the coordinate vector of vehicle's position O_b expressed in the target frame. A coordinate transformation leads to the following relationship:

$$\lambda^t = R_e^t(\lambda - \lambda_t), \tag{5.17}$$

where R_e^t is the rotation matrix from target frame to inertia frame. λ_t is the coordinate of the target frame origin O_t expressed in inertia frame. Both R_e^t and λ_t are constants for a particular drilling/screwing operation. Differentiating the above equation twice, and applying (5.5), (5.6), we have

$$M\ddot{\lambda}^t = F_p^t + F_g^t + F_c^t, \tag{5.18}$$

where F_p^t, F_g^t, F_c^t are the total thrust force, gravity force, and contact force represented in target frame, respectively.

The selective impedance controller is designed as

$$F_p^t = -F_g^t - F_c^t + M\ddot{\lambda}_d^t - C\dot{e}_\lambda^t - Ke_\lambda^t, \tag{5.19}$$

where $e^t_\lambda = \lambda^t - \lambda^t_d$ is the position tracking error in target frame, λ^t_d is the desired position, $C = diag(C_x, C_y, C_z)$ and $K = diag(K_x, K_y, K_z)$ are diagonal matrices consisting of all the virtual damping and spring parameters along X^t, Y^t, Z^t. With the proposed design, it is clear that the following impedance model relating the position tracking error to the contact force holds true:

$$M\ddot{e}^t_\lambda + C\dot{e}^t_\lambda + Ke^t_\lambda = F^t_c. \tag{5.20}$$

The damping and spring parameters for different axes can be selected differently to achieve the hybrid motion/force control objective. For the proposed drilling/screwing application, K_x and K_y are chosen to be big enough to ensure an accurate target point tracking on the tangential plane if λ^t_{dx} and λ^t_{dy} are both set as zero. Since the tangential contact force is normally very small, the position tracking error $e^t_{\lambda x}$ and $e^t_{\lambda y}$ will exponentially converge to zero. In comparison, K_z is selected to be relatively small to make the impedance model more flexible along the normal direction, allowing an efficient indirect normal contact force regulation by properly tuning the desired position. It can be seen that at steady state, the contact force along Z^t converges to its desired setpoint F^t_d if the desired position along Z^t is set to be $z^t_d = z^t - \frac{F^t_d}{K_z}$. After all the spring constants for the impedance model are set, the damping constants will be selected to maximize the transient performance. For example, C can be chosen as $1.414\sqrt{KM}$ so that the closed-loop damping ratio of each axis is 0.707, which gives the maximum bandwidth without any resonant peak in the bode magnitude plot.

After synthesizing the target frame thrust force F^t_p, the inertia frame thrust force can be calculated as $F^e_p = R^e_t F^t_p$. To achieve this required thrust force in inertia frame, the body-frame thrust components F^b_{py}, F^b_{pz} as well as the desired pitch angle

θ_d fed into the low-level controller are calculated as follows

$$\begin{aligned} F_{py}^b &= (F_{px}^e C_\psi + F_{py}^e S_\psi)^2 S_\phi + {F_{pz}^e}^2 S_\phi \\ &\quad +(F_{px}^e S_\psi - F_{pz}^e C_\psi) C_\phi, \\ F_{pz}^b &= (F_{px}^e C_\psi + F_{py}^e S_\psi)^2 C_\phi + {F_{pz}^e}^2 C_\phi \\ &\quad +(F_{px}^e S_\psi - F_{py}^e C_\psi) C_\phi, \\ \theta_d &= atan\left(\frac{F_{px}^e C_\psi + F_{py}^e S_\psi}{F_{pz}^e}\right). \end{aligned} \tag{5.21}$$

Finally, by setting $\alpha = \beta$ and solving the five equations in (5.2) and (5.4), the individual rotor thrust forces and the tilt angle can be obtained as:

$$\begin{aligned} \alpha = \beta &= atan(\frac{F_{py}^b}{F_{pz}^b}) \\ F_1 &= \frac{F_{pz}^b k l_1 l_2 + k l_1 \tau_{px}^b + {C_a}^2 l_2 (k\tau_{py}^b + l_1 \tau_{pz}^b) + C_a S_a l_2 (l_1 \tau_{py}^b - k\tau_{pz}^b)}{4 C_a k l_1 l_2} \\ F_2 &= \frac{F_{pz}^b k l_1 l_2 - k l_1 \tau_{px}^b + {C_a}^2 l_2 (k\tau_{py}^b - l_1 \tau_{pz}^b) - C_a S_a l_2 (l_1 \tau_{py}^b + k\tau_{pz}^b)}{4 C_a k l_1 l_2} \\ F_3 &= \frac{F_{pz}^b k l_1 l_2 - k l_1 \tau_{px}^b - {C_a}^2 l_2 (k\tau_{py}^b - l_1 \tau_{pz}^b) + C_a S_a l_2 (l_1 \tau_{py}^b + k\tau_{pz}^b)}{4 C_a k l_1 l_2} \\ F_4 &= \frac{F_{pz}^b k l_1 l_2 + k l_1 \tau_{px}^b - {C_a}^2 l_2 (k\tau_{py}^b + l_1 \tau_{pz}^b) - C_a S_a l_2 (l_1 \tau_{py}^b - k\tau_{pz}^b)}{4 C_a k l_1 l_2}. \end{aligned} \tag{5.22}$$

5.5 Vision-based Target Identification and Tracking

During the aerial drilling/screwing operation, the end-effector needs to be aligned with the target point. This process could be extremely time consuming and inaccurate if conducted by a human operator who takes action based on the visual feedback information sent from the onboard camera. To overcome this challenge, a real-time vision-based target identification and tracking method is proposed, and is integrated with our human-guided manipulation to help improve positioning accuracy and efficiency for drilling and screwing. Under the proposed control framework, the vision-based target identification and tracking system aims at obtaining the relative position and orientation of the target frame w.r.t camera frame (λ_t^c and R_t^c) first, and subsequently the tracking error e_λ^t to be used in the high-level impedance controller. The vision system consists of the following three steps.

5.5.1 Target identification using a YOLO v3 object detector

The YOLO v3 detector eliminates the RoI extraction stage, and adopts a unified architecture that directly extracts feature maps from input images, then it regards the whole feature maps as candidate regions to predict bounding boxes and categories[80, 81]. Its characteristics of realtime object identification and high detection precision, make it a perfect solution for our object detection task in unstructured environments. Additionally, the target workpiece to be operated in real-world conditions may be in different sizes or trimmed to fit different environments, a more general and robust detector can be trained with more labeled images taken from different applications and environments. Each detector model utilized in this study is trained before the task based on a set of 600 images of the target taken from different distances and angles, and labeled by ourselves. This object detector will search for the target in the view of camera and predict a bounding box to indicate the position of the target in the image.

5.5.2 Target tracking using a Kanade-Lucas-Tomasi (KLT) tracker

Although YOLO is a robust and powerful object detector, the outcoming bounding box does not estimate the rotation of object caused by the change of UAV's pitch angle θ. Besides, the DNN-based YOLO object detector is computationally expensive since it extracts feature maps from the entire input image. Thus, to track the target position and orientation in real time, we use the computationally efficient Kanade-Lucas-Tomasi (KLT) algorithm that can estimate and track all basic 2D transformations of the target in a small local region of the input image [82].

Following the first step, once the target workpiece is located by YOLO v3 object detector, a bounding box is inserted around the workpiece to indicate a small template image for tracking, the next step is to extract feature points within the bounding box that can be reliably tracked, using the proposed method from [83]. The type of 2D

transformation to be tracked in this work is called similarity including translation, rotation and scaling, which can be expressed as

$$\boldsymbol{x}' = \begin{bmatrix} s\boldsymbol{R} & \boldsymbol{t} \end{bmatrix} \overline{\boldsymbol{x}} \tag{5.23}$$

where $\boldsymbol{x}'$ is the point coordinate in image plane after transformation, $\overline{\boldsymbol{x}}$ is the homogenous coordinate before transformation, s is an arbitrary scale factor, $\boldsymbol{R}$ is an orthonormal rotation matrix, $\boldsymbol{t} = [t_x, t_y]^T$ is the translation vector.

To better parameterize the transformation for tracking, the warping function is defined as

$$\mathbf{W}(\mathbf{x};\mathbf{p}) = \begin{bmatrix} a & -b & t_x \\ b & a & t_y \end{bmatrix} \begin{bmatrix} x \\ y \\ 1 \end{bmatrix}, \tag{5.24}$$

where $\mathbf{x} = [x, y]^T$, and $\mathbf{p} = \begin{bmatrix} t_x, t_y, a, b \end{bmatrix}^{\mathrm{T}}$ is the vector of transformation parameters. At every time instance, the optimal parameter increase $\Delta\mathbf{p}$ is calculated by solving the following the problem minimizing the feature point difference between the template image and warped-back image [84]:

$$\min_{\Delta\mathbf{p}} \sum_{\mathbf{x}} [I(\mathbf{W}(\mathbf{x};\mathbf{p}+\Delta\mathbf{p})) - T(\mathbf{x})]^2, \tag{5.25}$$

where $T(\mathbf{x})$ is template image. $I(\mathbf{W}(\mathbf{x};\mathbf{p}+\Delta\mathbf{p}))$ is input image warped back onto the coordinate frame of the template.

The parameters $\mathbf{p}$ will be updated iteratively according to $\Delta\mathbf{p}$, and transformation is then applied to the bounding box around the target feature for real-time tracking.

5.5.3 Morphological image processing to obtain the target coordinate

The objective in the final step is to acquire the camera-frame coordinate of the point of interest for drilling/screwing on the target feature. This goal can be achieved by

investigating the structure of the feature and extracting geometrical elements from the structure. However, numerous noises and errors would be introduced into the image by disturbances from the unstructured environments. Thus, the morphological image processing method [85] is applied to remove the noises and enhance image quality by accounting for the form and structure of the image, furthermore, to generate accurate coordinate information of the point of interest in camera frame.

Customized morphological structuring elements can be defined to locate the specific geometry element and the point for drilling and screwing on the target feature. After that, the position of target point $\begin{bmatrix} x_t^c & y_t^c & z_t^c \end{bmatrix}^{\mathrm{T}}$ expressed in camera frame can be derived from the pixel coordinate(u_i, v_i) of it in image plane through the follow relation:

$$\begin{bmatrix} x_t^c \\ y_t^c \\ z_t^c \end{bmatrix} = z_t^c \begin{bmatrix} \alpha_x f & sf & p_x \\ 0 & \alpha_y f & p_y \\ 0 & 0 & 1 \end{bmatrix}^{-1} \begin{bmatrix} u_{\mathrm{i}} \\ v_{\mathrm{i}} \\ 1 \end{bmatrix}, \tag{5.26}$$

where f is the focal length, α_x, α_y are pixel scaling factors, (p_x, p_y) is the principle point (where optical axis hits image plane) , s is the slant factor when the image plane is not normal to the optical axis.

5.6 Experiments

In this section, the proposed novel UAV platform for aerial drilling and screwing are experimentally validated at the Assistive and Intelligent Robotics Lab of NJIT. Experimental setup is first illustrated, then followed by experimental results and discussions. The video of the experiments is available at https://youtu.be/uw6Aw78jlgY.

5.6.1 Experimental setup

The newly designed aerial manipulator used in the experiment is equipped with an ARM Cortex based PX4 Pixhawk2 flight controller for computing the control input

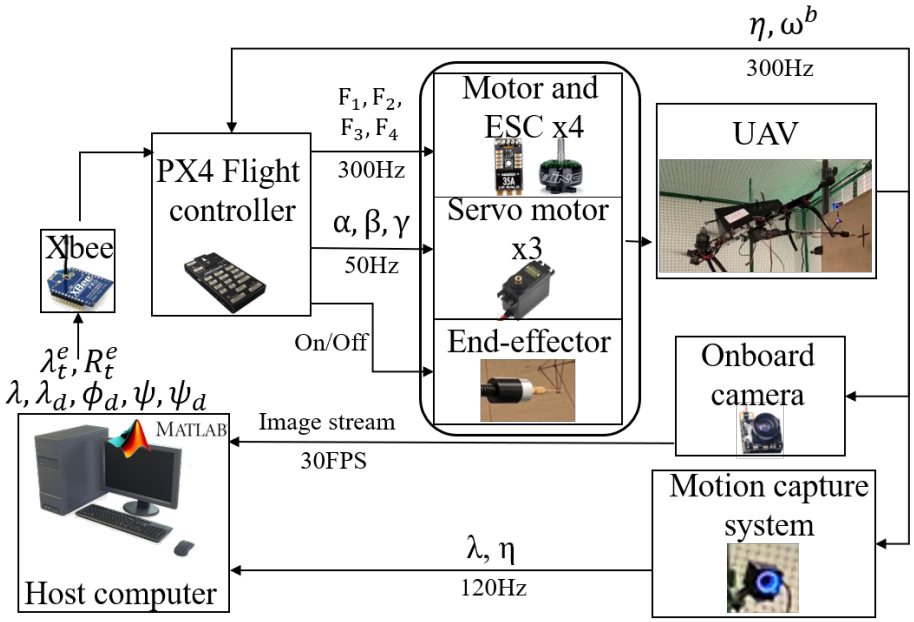

Figure 5.3 The overall system architecture of the experiment, showing the key components and the data flow.

and communicating with ground host computer through an XBee module, as shown in Figure 5.3. To detect the target object, a zero-latency all-in-one camera (including an FPV camera, a transmitter and an antenna) is installed with eye-in-hand configuration. The camera has about 120° FOV and the resolution of the image is 640×480 with 30 fps. An OptiTrack motion capture system is set up around the flight testing area to acquire attitude and position measurement of the vehicle at $120Hz$, and send it to the host computer. The host computer also receives video from the onboard camera in realtime through a $5.8G$ $150CH$ UVC receiver. Based on received video and motion capture information, the proposed vision-based identification and tracking algorithm is running on the host computer, and commands are sent to the UAV through Xbee.

5.6.2 Experimental results and discussions

First, to verify the vehicle's decoupled motion and force control performances on the longitudinal plane, which are regulated by the low-level ARC attitude control and the high-level selective impedance control respectively, we carry out a contact force test

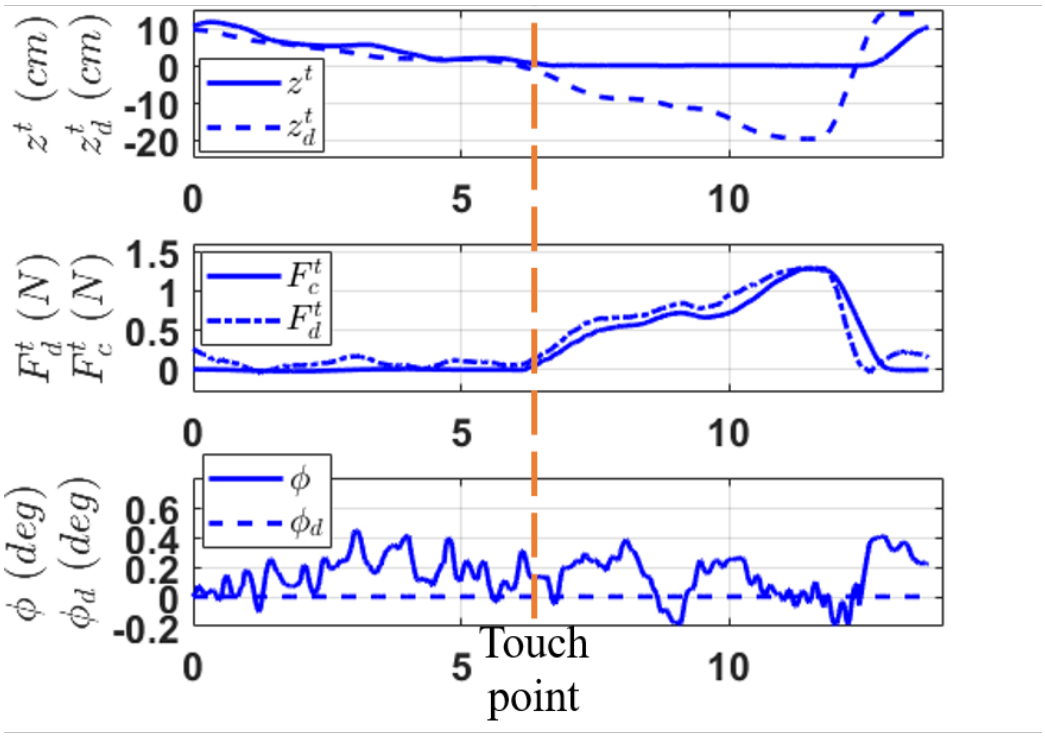

Figure 5.4 Experimental characterizations of the impedance controller and the attitude controller. Touch point is where the arm begins touching the wood board.

by pushing the manipulator arm (with end-effector removed) against a wood board attached to a 6-axis ATI F/T sensor while maintaining a stable body hovering. As shown in Figure 5.4, before the end-effector touches the board, the forward motion is well controlled with z^t close to z_d^t. After contact is established, z^t stays constant, while $z_d^t = z^t - \frac{F_d^t}{K_z}$ penetrates into the board to generate the required contact force. The corresponding force command $F_d^t = K_z(z^t - z_d^t)$ matches the real measured force F_c^t very well. The independent rotational motion (ϕ) keeps stationary during the whole test, even as the manipulator arm is in contact with the board, showing the reliability of the controller.

Next, we conduct three tests for both the aerial hole drilling and the bolt screwing tasks, as shown in Figure 5.5 and illustrated in the video file attached. A 12mm thick wood board is used as the workpiece and is placed vertically in the lab zone. For demonstration purpose, we simply draw cross-shaped center marks on

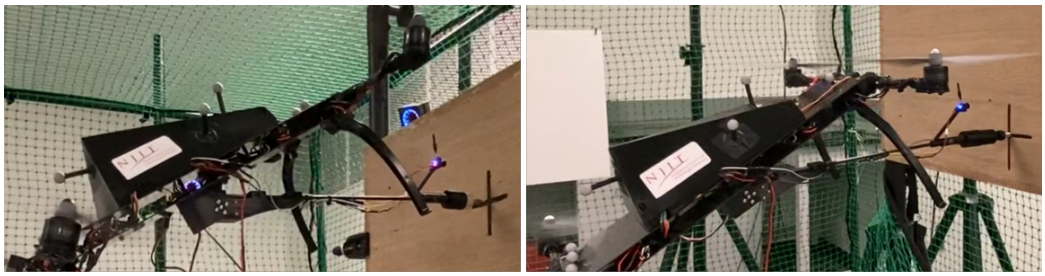

(a) Drilling (b) Screwing

Figure 5.5 Aerial hole drilling and screwing with the proposed human-guided semi-automated aerial drilling/screwing platform

the board to represent the target locations for drilling/screwing operations. After the aerial manipulator is guided close to the board, and a proper view of the cross marker is obtained, the vision-based identification and tracking system is activated and successfully implemented, as shown in Figure 5.6. The position tracking error between the target point and the end-effector, captured by the vision guidance system, expressed in the target frame is shown in Figure 5.7. The plots demonstrate that the vision-based guidance system can successfully capture the position of the target and output smooth tracking error, enabling accurate and fast target tracking for drilling/screwing.

After the drill/screwdriver is aligned with the target point, a human operator guides the aerial manipulator to conduct feeding operation by tuning the contact force command. The selective impedance control law running on host computer takes the contact force command as input and automatically generates desired position commands to indirectly regulate the contact force between the end-effector and wood board along the feeding direction. As can be seen in Figure 5.8, to approach to the wood board, very light and short-time force commands are given to gradually drive the aerial manipulator forward. After contact is established, strong and continuous contact force is exerted to execute and accelerate the drilling/screwing operation. It can be found that the drilling requires a stronger contact force to penetrate wood

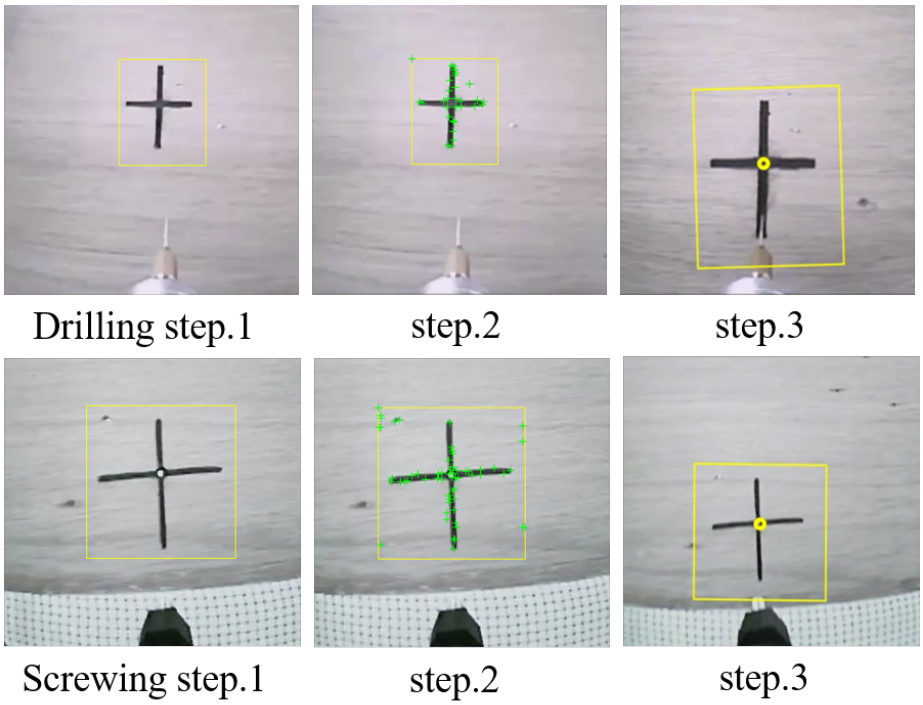

Figure 5.6 The three steps of vision-based positioning and tracking method: the first step is target object detection by a YOLO v3 detector, the second step is feature points extraction and 2D transformation tracking using KLT tracker, the third step is to capture the point of interest for drilling/screwing.

board surface compared with the screwing process. Overall, the experimental results show the effectiveness of the proposed platform with design, control and sensing in aerial hole drilling and bolt screwing. The accuracy over all the three drilling tests is within $\pm 2.5mm$, as shown in Figure 5.9.

5.7 Conclusions

This chapter presented the design, sensing, and control of a novel UAV platform for omnidirectional aerial drilling and screwing. To solve the coupling between translational and rotational motions of aerial manipulators based on traditional multirotors, a novel 5-DOF actuated energy efficient aerial manipulator was designed with the capability of independently exerting strong drilling/screwing force to the workpiece along any direction on the longitudinal plane. A dual-level control

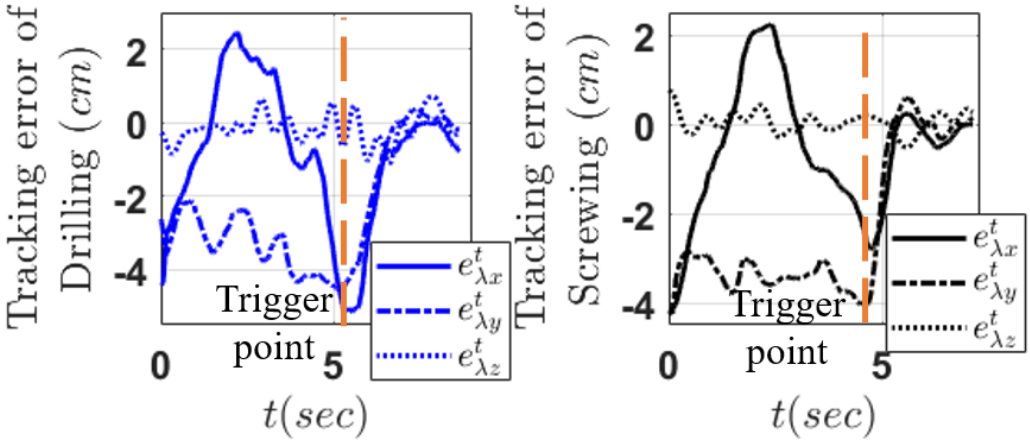

Figure 5.7 Position of the target point with respect to end-effector estimated by the vision guidance system and expressed in the target frame. At the trigger point, command is sent to align the end-effector tool with the target point.

architecture was proposed, with a low-level adaptive robust control (ARC) to accurately track the attitude angles in the presence of force/torque uncertainties, and a high level selective impedance control to indirectly control the contact force commanded by the user and track the target position. A vision-based identification and tracking scheme was developed by integrating a robust YOLO v3 object detector with feature tracking and morphological techniques, achieving automatically alignment between the drill/screwdriver and target point. Experimental results conducted indoor under the motion capture system were presented to verify the proposed aerial manipulation platform. In the future, we expect to use onboard sensors for localization and apply the platform to various challenging outdoor applications in construction, decoration, transportation, or maintenance at hard-to-reach locations.

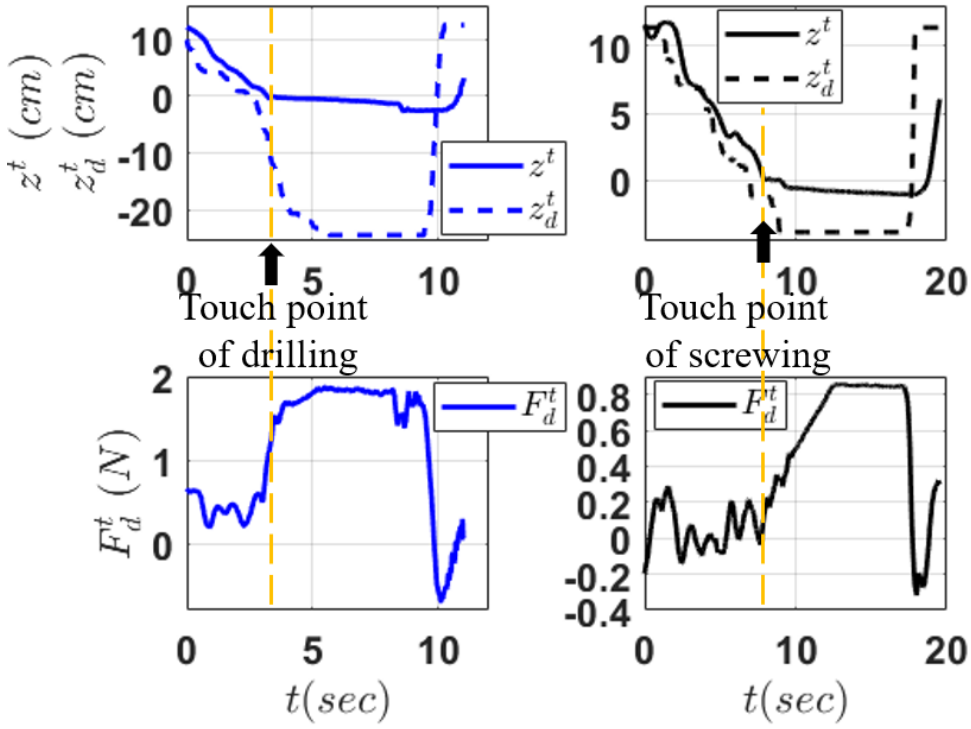

Figure 5.8 The force command F_d^t along Z^t for drilling (left) and screwing (right). Touch point is where the end-effector begins touching the wood board.

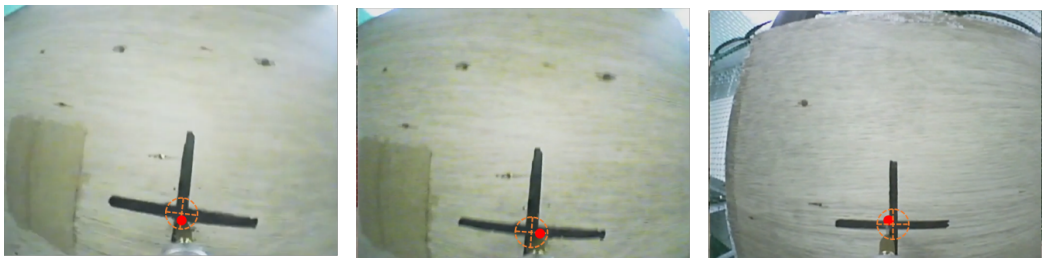

Figure 5.9 The drilling accuracy over all the three aerial drilling tests.

CHAPTER 6

CONCLUSIONS

In this dissertation, firstly we studied an energy-efficient adaptive robust tracking control for a class of novel vector thrust UAVs. The mechanical structure of the vector thrust UAV with all propellers able to tilt about two perpendicular axes was first presented. Based on this design, we formulated the dynamic model of the vehicle with arbitrary number of such propellers in the presence of parametric uncertainties including unknown moment of inertia, mass and center of mass, which previous literature have hardly dealt with. Additionally, an adaptive robust control was designed for accurate trajectory tracking in the presence of various types of uncertainties. A thrust force optimization problem minimizing the instantaneous power consumption while achieving the desired body force wrench was then solved to obtain the individual thrust force vectors of the rotors. From the simulations, the resulting controller achieved a guaranteed transient performance and final tracking accuracy in the presence of uncertainties. In addition, a higher efficiency of energy utilization can be achieved with the proposed thrust force optimization strategy.

Next, we developed a novel 6-DOF automated flight testing strategy for VTOL UAVs by mounting the vehicle to the end-effector of an articulated humanoid robot arm through a 6-axis force/torque sensor. During the flight testing process, a dual-module control law was executed. In the regular control module, a damping force control with feedforward compensation was implemented to minimize the interaction force between the vehicle and the robot end-effector regardless of the constantly-changing motion of the vehicle. In the safety module, a safety algorithm was activated to constrain the range of the motion of the vehicle in case of emergency. The proposed strategy was verified to be capable of emulating a realistic free flight environment while ensuring

safety through both theoretical justification and experimental validation, making it an ideal choice for initial flight testings.

With the help of the developed 6-DOF automated flight testing platform, we studied the design, control and applications of a novel multirotor UAV for enhanced aerial locomotion and manipulation performances. The aerial vehicle employs a tilting-rotor architecture, and was designed to be in an "H" configuration. With such a design, the UAV has independent roll angle regulation to be able to perform challenging aerial locomotion and manipulation tasks, at the expense of only two additional servo motors with minimum transmission needed. Based on the dynamics of the proposed UAV, we formulated a dual-level adaptive robust control (ARC) method to cope with parametric uncertainties and uncertain nonlinearities that may occur during aerial maneuvering and manipulation. Additionally, we studied and precisely solved a thrust force optimization problem minimizing power consumption while achieving the desired body force wrench to efficiently resolve the redundancy in actuation. At the end, we validated the applicability of the complete system through four challenging experiments: tracking a circular trajectory, passing through a narrow tunnel, picking up an object from a cluttered shelf, and human-guided hole drilling. Experimental results showed the superior performance of the design and control when performing real demanding aerial locomotion and manipulation tasks in unstructured environments.

Finally, a human-guided semi-automated aerial drilling/screwing platform based on our developed novel tilting-rotor aerial manipulator was presented. To solve the coupling between translational and rotational motions of aerial manipulators, the novel 5-DOF actuated aerial manipulator was employed because of its capability of independently exerting strong drilling/screwing force to the workpiece along any direction on the longitudinal plane. A dual-level control architecture was studied, with a low-level adaptive robust control (ARC) to accurately track the attitude angles

in the presence of force/torque uncertainties, and a high level selective impedance control to indirectly control the contact force commanded by the user and track the target position. A vision-based identification and tracking scheme was developed by integrating a robust YOLO v3 object detector with feature tracking and morphological techniques, achieving automatically alignment between the drill/screwdriver and target point. Experimental results conducted indoor under the motion capture system were presented to verify the proposed aerial manipulation platform. In the future, we expect to use onboard sensors for localization and apply the platform to various challenging outdoor applications in construction, decoration, transportation, or maintenance at hard-to-reach locations.

REFERENCES

[1] M. Ryll, H. H. Bülthoff, and P. R. Giordano, "A novel overactuated quadrotor unmanned aerial vehicle: Modeling, control, and experimental validation," *IEEE Transactions on Control Systems Technology*, vol. 23, no. 2, pp. 540–556, 2015.

[2] T. Bartelds, A. Capra, S. Hamaza, S. Stramigioli, and M. Fumagalli, "Compliant aerial manipulators: Toward a new generation of aerial robotic workers," *IEEE Robotics and Automation Letters*, vol. 1, no. 1, pp. 477–483, 2016.

[3] G. Heredia, A. Jimenez-Cano, I. Sanchez, D. Llorente, V. Vega, J. Braga, J. Acosta, and A. Ollero, "Control of a multirotor outdoor aerial manipulator," in *Intelligent Robots and Systems (IROS), IEEE/RSJ International Conference on*, pp. 3417–3422, 2014.

[4] D. Brescianini and R. D'Andrea, "Design, modeling and control of an omni-directional aerial vehicle," in *IEEE International Conference on Robotics and Automation (ICRA)*, pp. 3261–3266, 2016.

[5] G. Jiang and R. Voyles, "A nonparallel hexrotor uav with faster response to disturbances for precision position keeping," in *Safety, Security, and Rescue Robotics (SSRR), IEEE International Symposium on*, pp. 1–5, 2014.

[6] H. Mehmood, T. Nakamura, and E. N. Johnson, "A maneuverability analysis of a novel hexarotor uav concept," in *International Conference on Unmanned Aircraft Systems (ICUAS)*, pp. 437–446, IEEE, 2016.

[7] M. K. Mohamed and A. Lanzon, "Design and control of novel tri-rotor uav," in *Proceedings of UKACC International Conference on Control*, pp. 304–309, IEEE, 2012.

[8] S. Rajappa, M. Ryll, H. H. Bülthoff, and A. Franchi, "Modeling, control and design optimization for a fully-actuated hexarotor aerial vehicle with tilted propellers," in *IEEE International Conference on Robotics and Automation (ICRA)*, pp. 4006–4013, 2015.

[9] M. Ryll, D. Bicego, and A. Franchi, "Modeling and control of fast-hex: A fully-actuated by synchronized-tilting hexarotor," in *IEEE/RSJ International Conference on Intelligent Robots and Systems (IROS)*, pp. 1689–1694, 2016.

[10] D. De Martini, G. V. Gramazio, A. Bertini, C. Rottenbacher, and T. Facchinetti, "Design and modeling of a quadcopter with double axis tilting rotors," *Unmanned Systems*, vol. 5, no. 03, pp. 169–180, 2017.

[11] H. Lee and H. J. Kim, "Estimation, control, and planning for autonomous aerial transportation," *IEEE Transactions on Industrial Electronics*, vol. 64, no. 4, pp. 3369–3379, 2017.

[12] M. Orsag, C. M. Korpela, S. Bogdan, and P. Y. Oh, "Hybrid adaptive control for aerial manipulation," *Journal of Intelligent and Robotic Systems*, vol. 73, no. 1-4, pp. 693–707, 2014.

[13] N. Cao and A. F. Lynch, "Inner–outer loop control for quadrotor uavs with input and state constraints," *IEEE Transactions on Control Systems Technology*, vol. 24, pp. 1797–1804, Sep. 2016.

[14] R. Mahony and T. Hamel, "Robust trajectory tracking for a scale model autonomous helicopter," *International Journal of Robust and Nonlinear Control*, vol. 14, no. 12, pp. 1035–1059, 2004.

[15] M. Fliess, J. Lévine, P. Martin, and P. Rouchon, "Flatness and defect of non-linear systems: introductory theory and examples," *International Journal of Control*, vol. 61, no. 6, pp. 1327–1361, 1995.

[16] R. Spica, A. Franchi, G. Oriolo, H. H. Bülthoff, and P. R. Giordano, "Aerial grasping of a moving target with a quadrotor uav," in *IEEE/RSJ International Conference on Intelligent Robots and Systems*, pp. 4985–4992, 2012.

[17] M. Fumagalli and R. Carloni, "A modified impedance control for physical interaction of uavs," in *IEEE/RSJ International Conference on Intelligent Robots and Systems*, pp. 1979–1984, 2013.

[18] T. Madani and A. Benallegue, "Backstepping control for a quadrotor helicopter," in *IEEE/RSJ International Conference on Intelligent Robots and Systems*, pp. 3255–3260, 2006.

[19] V. Lippiello, G. Loianno, and B. Siciliano, "Mav indoor navigation based on a closed-form solution for absolute scale velocity estimation using optical flow and inertial data," in *50th IEEE Conference on Decision and Control and European Control Conference*, pp. 3566–3571, 2011.

[20] A. Roberts and A. Tayebi, "Adaptive position tracking of vtol uavs," *IEEE Transactions on Robotics*, vol. 27, no. 1, pp. 129–142, 2011.

[21] I. Palunko, P. Cruz, and R. Fierro, "Agile load transportation: Safe and efficient load manipulation with aerial robots," *IEEE Robotics and Automation Magazine*, vol. 19, no. 3, pp. 69–79, 2012.

[22] G. Antonelli, E. Cataldi, P. R. Giordano, S. Chiaverini, and A. Franchi, "Experimental validation of a new adaptive control scheme for quadrotors mavs," in *IEEE/RSJ International Conference on Intelligent Robots and Systems*, pp. 2439–2444, 2013.

[23] G. Antonelli, F. Arrichiello, S. Chiaverini, and P. R. Giordano, "Adaptive trajectory tracking for quadrotor mavs in presence of parameter uncertainties and external disturbances," in *IEEE/ASME International Conference on Advanced Intelligent Mechatronics*, pp. 1337–1342, 2013.

[24] Z. T. Dydek, A. M. Annaswamy, and E. Lavretsky, "Adaptive control of quadrotor uavs: A design trade study with flight evaluations," *IEEE Transactions on Control Systems Technology*, vol. 21, no. 4, pp. 1400–1406, 2013.

[25] D. Cabecinhas, R. Cunha, and C. Silvestre, "A nonlinear quadrotor trajectory tracking controller with disturbance rejection," *Control Engineering Practice*, vol. 26, pp. 1–10, 2014.

[26] L. Lu and J. T. Wen, "Human-robot cooperative control for mobility impaired individuals," in *American Control Conference (ACC)*, pp. 447–452, July 2015.

[27] S. Sivčev, J. Coleman, E. Omerdić, G. Dooly, and D. Toal, "Underwater manipulators: A review," *Ocean Engineering*, vol. 163, pp. 431 – 450, 2018.

[28] A. Flores-Abad, O. Ma, K. Pham, and S. Ulrich, "A review of space robotics technologies for on-orbit servicing," *Progress in Aerospace Sciences*, vol. 68, pp. 1 – 26, 2014.

[29] Z. Song, K. Li, Z. Cai, Y. Wang, and N. Liu, "Modeling and maneuvering control for tricopter based on the back-stepping method," in *Guidance, Navigation and Control Conference (CGNCC), 2016 IEEE Chinese*, pp. 889–894, IEEE, 2016.

[30] B. Yao, C. Hu, L. Lu, and Q. Wang, "Adaptive robust precision motion control of a high-speed industrial gantry with cogging force compensations," *IEEE Transactions on Control Systems Technology*, vol. 19, no. 5, pp. 1149–1159, 2011.

[31] A. Mohanty and B. Yao, "Indirect adaptive robust control of hydraulic manipulators with accurate parameter estimates," *IEEE Transactions on Control Systems Technology*, vol. 19, no. 3, pp. 567–575, 2011.

[32] S. Boyd and L. Vandenberghe, *Convex optimization*. Cambridge university press, 2004.

[33] B. Hu, L. Lu, and S. Mishra, "Fast, safe and precise landing of a quadrotor on an oscillating platform," in *American Control Conference (ACC)*, pp. 3836–3841, IEEE, 2015.

[34] B. Hu, L. Lu, and S. Mishra, "A control architecture for time-optimal landing of a quadrotor onto a moving platform," *Asian Journal of Control*, 2018.

[35] W. Dong, G.-Y. Gu, X. Zhu, and H. Ding, "Development of a quadrotor test bed—modelling, parameter identification, controller design and trajectory generation," *International Journal of Advanced Robotic Systems*, vol. 12, no. 2, p. 7, 2015.

[36] S. Bouabdallah, P. Murrieri, and R. Siegwart, "Design and control of an indoor micro quadrotor," in *IEEE International Conference on Robotics and Automation, 2004. Proceedings. ICRA'04. 2004*, vol. 5, pp. 4393–4398.

[37] Y. Yu and X. Ding, "A quadrotor test bench for six degree of freedom flight," *Journal of Intelligent & Robotic Systems*, vol. 68, no. 3-4, pp. 323–338, 2012.

[38] J. G. B. Farias Filho, C. E. Dórea, W. M. Bessa, and J. L. C. Farias, "Modeling, test benches and identification of a quadcopter," in *Robotics Symposium and IV Brazilian Robotics Symposium (LARS/SBR), 2016 XIII Latin American*, pp. 49–54, IEEE.

[39] J.-T. Zou, K.-L. Su, and H. Tso, "The modeling and implementation of tri-rotor flying robot," *Artificial Life and Robotics*, vol. 17, no. 1, pp. 86–91, 2012.

[40] F. Caccavale, C. Natale, B. Siciliano, and L. Villani, "Six-dof impedance control based on angle/axis representations," *IEEE Transactions on Robotics and Automation*, vol. 15, no. 2, pp. 289–300, 1999.

[41] L. Villani and J. De Schutter, "Force control," in *Springer Handbook of Robotics*, pp. 195–220, Springer, 2016.

[42] L. Lu, Z. Chen, B. Yao, and Q. Wang, "Desired compensation adaptive robust control of a linear-motor-driven precision industrial gantry with improved cogging force compensation," *IEEE/ASME Transactions on Mechatronics*, vol. 13, no. 6, pp. 617–624, 2008.

[43] H. K. Khalil, "Noninear systems (3rd edition)," *Pearson*, 2001.

[44] B. Hu and S. Mishra, "Time-optimal trajectory generation for landing a quadrotor onto a moving platform," *IEEE/ASME Transactions on Mechatronics*, vol. 24, no. 2, pp. 585–596, 2019.

[45] N. Zhao, W. Lu, M. Sheng, Y. Chen, J. Tang, F. R. Yu, and K.-K. Wong, "Uav-assisted emergency networks in disasters," *IEEE Wireless Communications*, vol. 26, no. 1, pp. 45–51, 2019.

[46] K. Ivushkin, H. Bartholomeus, A. K. Bregt, A. Pulatov, M. H. Franceschini, H. Kramer, E. N. van Loo, V. J. Roman, and R. Finkers, "Uav based soil salinity assessment of cropland," *Geoderma*, vol. 338, pp. 502–512, 2019.

[47] B. Zhou, F. Gao, L. Wang, C. Liu, and S. Shen, "Robust and efficient quadrotor trajectory generation for fast autonomous flight," *IEEE Robotics and Automation Letters*, vol. 4, no. 4, pp. 3529–3536, 2019.

[48] J. R. Kutia, K. A. Stol, and W. Xu, "Aerial manipulator interactions with trees for canopy sampling," *IEEE/ASME Transactions on Mechatronics*, vol. 23, no. 4, pp. 1740–1749, 2018.

[49] M. Jafarinasab, S. Sirouspour, and E. Dyer, "Model-based motion control of a robotic manipulator with a flying multirotor base," *IEEE/ASME Transactions on Mechatronics*, vol. 24, no. 5, pp. 2328–2340, 2019.

[50] A. Wojciechowska, J. Frey, S. Sass, R. Shafir, and J. R. Cauchard, "Collocated human-drone interaction: Methodology and approach strategy," in *14th ACM/IEEE International Conference on Human-Robot Interaction (HRI)*, pp. 172–181, 2019.

[51] G. Hoffmann, H. Huang, S. Waslander, and C. Tomlin, "Quadrotor helicopter flight dynamics and control: Theory and experiment," in *AIAA Guidance, Navigation and Control Conference and Exhibit*, p. 6461, 2007.

[52] S. Zairi and D. Hazry, "Adaptive neural controller implementation in autonomous mini aircraft quadrotor (amac-q) for attitude control stabilization," in *IEEE 7th International Colloquium on Signal Processing and its Applications*, pp. 84–89, 2011.

[53] H.-N. Nguyen and D. Lee, "Hybrid force/motion control and internal dynamics of quadrotors for tool operation," in *2013 IEEE/RSJ International Conference on Intelligent Robots and Systems*, pp. 3458–3464, IEEE, 2013.

[54] G. O. Vargas, C. Hintz, L. R. G. Carrillo, F. M. Palacios, and E. S. E. Quesada, "Dynamic modeling of a multi-rotorcraft uas with morphing capabilities," in *2015 International Conference on Unmanned Aircraft Systems (ICUAS)*, pp. 963–971, IEEE, 2015.

[55] R. Anderson, "Robust adaptive control laws for tilt-rotor quadcopters subject to user-defined constraints," 2019.

[56] H.-N. Nguyen, C. Ha, and D. Lee, "Mechanics, control and internal dynamics of quadrotor tool operation," *Automatica*, vol. 61, pp. 289–301, 2015.

[57] I. Palunko and R. Fierro, "Adaptive control of a quadrotor with dynamic changes in the center of gravity," *IFAC Proceedings Volumes*, vol. 44, no. 1, pp. 2626–2631, 2011.

[58] V. Lippiello and F. Ruggiero, "Exploiting redundancy in cartesian impedance control of uavs equipped with a robotic arm," in *2012 IEEE/RSJ International Conference on Intelligent Robots and Systems*, pp. 3768–3773, IEEE, 2012.

[59] H. Lee and H. J. Kim, "Estimation, control, and planning for autonomous aerial transportation," *IEEE Transactions on Industrial Electronics*, vol. 64, no. 4, pp. 3369–3379, 2016.

[60] H. Yang and D. Lee, "Dynamics and control of quadrotor with robotic manipulator," in *2014 IEEE International Conference on Robotics and Automation (ICRA)*, pp. 5544–5549, IEEE, 2014.

[61] L. Lu and B. Yao, "Energy-saving adaptive robust control of a hydraulic manipulator using five cartridge valves with an accumulator," *IEEE Transactions on Industrial Electronics*, vol. 61, no. 12, pp. 7046–7054, 2014.

[62] P. Ouyang, W. Zhang, M. M. Gupta, and W. Zhao, "Overview of the development of a visual based automated bio-micromanipulation system," *Mechatronics*, vol. 17, no. 10, pp. 578–588, 2007.

[63] R. Mahony, V. Kumar, and P. Corke, "Multirotor aerial vehicles: Modeling, estimation, and control of quadrotor," *IEEE Robotics and Automation magazine*, vol. 19, no. 3, pp. 20–32, 2012.

[64] A. F. Abdul Ghaffar and T. S. Richardson, "Position tracking of an underactuated quadrotor using model reference adaptive control," in *AIAA Guidance, Navigation, and Control Conference*, p. 1388, 2016.

[65] R. Pérez-Alcocer and J. Moreno-Valenzuela, "Adaptive control for quadrotor trajectory tracking with accurate parametrization," *IEEE Access*, vol. 7, pp. 53236–53247, 2019.

[66] S. Kim, H. Seo, S. Choi, and H. J. Kim, "Vision-guided aerial manipulation using a multirotor with a robotic arm," *IEEE/ASME Transactions On Mechatronics*, vol. 21, no. 4, pp. 1912–1923, 2016.

[67] J. Thomas, G. Loianno, J. Polin, K. Sreenath, and V. Kumar, "Toward autonomous avian-inspired grasping for micro aerial vehicles," *Bioinspiration and Biomimetics*, vol. 9, no. 2, p. 025010, 2014.

[68] D. Tzoumanikas, F. Graule, Q. Yan, D. Shah, M. Popovic, and S. Leutenegger, "Aerial manipulation using hybrid force and position nmpc applied to aerial writing," *arXiv preprint arXiv:2006.02116*, 2020.

[69] S. Park, J. Lee, J. Ahn, M. Kim, J. Her, G.-H. Yang, and D. Lee, "Odar: Aerial manipulation platform enabling omnidirectional wrench generation," *IEEE/ASME Transactions on Mechatronics*, vol. 23, no. 4, pp. 1907–1918, 2018.

[70] C. A. Ochoa, K. S. Meuche, and E. M. Atkins, "Multicopter operations for autonomous assembly applications in manufacturing environments," in *2018 Modeling and Simulation Technologies Conference*, p. 3888, 2018.

[71] D. Kim and P. Y. Oh, "Human-drone interaction for aerially manipulated drilling using haptic feedback," in *IEEE International Conference on Intelligent Robots and Sytsems (IROS)*, 2020.

[72] D. F. Carlson, J. Pasma, M. E. Jacobsen, M. H. Hansen, S. Thomsen, J. P. Lillethorup, F. S. Tirsgaard, A. Flytkjær, C. Melvad, K. Laufer, *et al.*, "Retrieval of ice samples using the ice drone," *Frontiers in Earth Science*, vol. 7, p. 287, 2019.

[73] Y. Sun, A. Plowcha, M. Nail, S. Elbaum, B. Terry, and C. Detweiler, "Unmanned aerial auger for underground sensor installation," in *2018 IEEE/RSJ International Conference on Intelligent Robots and Systems (IROS)*, pp. 1374–1381, IEEE, 2018.

[74] D. Brescianini and R. D'Andrea, "Computationally efficient trajectory generation for fully actuated multirotor vehicles," *IEEE Transactions on Robotics*, vol. 34, no. 3, pp. 555–571, 2018.

[75] C. Ding, L. Lu, and C. Wang, "Energy-efficient adaptive robust control of vector thrust uavs with unknown inertia parameters," in *Dynamic Systems and Control Conference*, vol. 51913, p. V003T36A005, American Society of Mechanical Engineers, 2018.

[76] M. Zarudzki, H.-S. Shin, and C.-H. Lee, "An image based visual servoing approach for multi-target tracking using an quad-tilt rotor uav," in *2017 International Conference on Unmanned Aircraft Systems (ICUAS)*, pp. 781–790, IEEE, 2017.

[77] C. Ding and L. Lu, "A tilting-rotor unmanned aerial vehicle for enhanced aerial locomotion and manipulation capabilities: Design, control, and applications," *IEEE/ASME Transactions on Mechatronics*, pp. 1–1, 2020. doi: 10.1109/TMECH.2020.3036346.

[78] J. Zhong and B. Yao, "Adaptive robust precision motion control of a piezoelectric positioning stage," *IEEE Transactions on Control Systems Technology*, vol. 16, no. 5, pp. 1039–1046, 2008.

[79] S. Liu and B. Yao, "Coordinate control of energy saving programmable valves," *IEEE Transactions on Control Systems Technology*, vol. 16, no. 1, pp. 34–45, 2007.

[80] J. Redmon, S. Divvala, R. Girshick, and A. Farhadi, "You only look once: Unified, real-time object detection," in *Proceedings of the IEEE Conference on Computer Vision and Pattern Recognition*, pp. 779–788, 2016.

[81] Y. Cai, H. Li, G. Yuan, W. Niu, Y. Li, X. Tang, B. Ren, and Y. Wang, "Yolobile: Real-time object detection on mobile devices via compression-compilation co-design," *arXiv preprint arXiv:2009.05697*, 2020.

[82] R. Szeliski, *Computer vision: algorithms and applications*. Springer Science & Business Media, 2010.

[83] J. Shi *et al.*, "Good features to track," in *1994 Proceedings of IEEE Conference on Computer Vision and Pattern Recognition*, pp. 593–600, IEEE, 1994.

[84] S. Baker and I. Matthews, "Lucas-kanade 20 years on: A unifying framework," *International Journal of Computer Vision*, vol. 56, no. 3, pp. 221–255, 2004.

[85] N. Efford, *Digital image processing: a practical introduction using java (with CD-ROM)*. Addison-Wesley Longman Publishing Co., Inc., 2000.